Direct Numerical Simulations of the Compressible Low Atwood Rayleigh-Taylor Instability

by

Scott A. Wieland

B.S. Physics, Mansfield University of Pennsylvania, 2012

A thesis submitted to the

Faculty of the Graduate School of the

University of Colorado in partial fulfillment

of the requirements for the degree of

Doctor of Philosophy

Department of Mechanical Engineering

2018

This thesis entitled:
Direct Numerical Simulations of the Compressible Low Atwood Rayleigh-Taylor Instability
written by Scott A. Wieland
has been approved for the Department of Mechanical Engineering

Prof. Peter E. Hamlington

Dr. Daniel Livescu

Prof. Scott J. Reckinger

Prof. Daven Henze

Prof. John A. Evans

Date

The final copy of this thesis has been examined by the signatories, and we find that both the content and the form meet acceptable presentation standards of scholarly work in the above mentioned discipline.

Wieland, Scott A. (Ph.D., Mechanical Engineering)

Direct Numerical Simulations of the Compressible Low Atwood Rayleigh-Taylor Instability

Thesis directed by Prof. Peter E. Hamlington

Two fluids are considered Rayleigh-Taylor unstable when the more dense fluid is suspended above the less dense fluid in the presence of a gravitational like accelerative force. When a perturbation is applied to the interface between the two, they begin mixing as the light fluid rises and the heavy fluid drops. The extension of this to the compressible regime leads to the densities of the fluids to not be constant, but instead the molar mass is used to define the weights. At the interface, a density jump still occurs, but away from the interface the densities can vary in a variety of ways. This research investigates the effects of these density changes by imposing an initial background stratification before the initial perturbation is applied. Isothermal, isentropic, and isopycnic initial conditions are imposed for small molar mass differences and the growth of the perturbations are studied through the use of the Parallel Adaptive Wavelet Collocation Method. Strong non-linear interactions lead to the growth and destruction of complex vortical fields resulting in the initial suppression of the instability in all cases. For the isothermal case, this leads to a complete suppression at moderate to high Mach numbers, but for the isentropic and isopycnic case, this initial suppression is overcome and an increased acceleration occurs that grows with the Mach number. To further investigate these interactions, the vorticity transport equation is investigated and modified to give insights into the effects background stratification and fluctuating terms. In addition to this, a comparison is drawn to the simplified case of vortex pairs and rings propagating in the same stratifications. All of these interactions and discoveries have strong implications for understanding the physics governing engineering scenarios such as fuel capsules in inertial confinement fusion, flame front propagation in supernovae, and the mixing of fuels in some specialized burners.

Dedication

To my family for their love,

and to my friends for the laughs,

but really, to all the ones who skirt the line,

'cause they are truly the ones who always have had my back.

Acknowledgements

This entire trip through the realm of graduate school has been nothing but a roller coaster and the only reason why I have been able to make it through is thanks to my friends, family, colleagues, and advisors. Of course, though, there have been some people that have stood out above the rest. First and foremost, I must thank my (current) advisor Dr. Peter Hamlington, for not only taking me under his wing at a moment when I thought my doctorate was ripped out from under me, but for the all hard work he is able to accomplish for not just me, but all of his many students along with the entire scientific community. Dr. Daniel Livescu has been my trusted advisor and has steered this research from the very start. Without him, this definitely would not have been possible, and he has also supplied me with the fantastic opportunity to spend time at Los Alamos National Lab. Dr. Scott Reckinger was the one to truly pioneer this project, and has been around to assist ever since. A special thanks must also be given to Dr. Daven Henze and Dr. John Evans for joining my committee and for offering helpful insights whenever possible.

To my Dad, my Mom, Scott, Ann, Skippy, Jenny, Steph, and Keith, you have helped me recuperate and stay motivated since day one. To my nephews, hopefully someday, someone writes one of these to help you out little Paul, and until then, Logan, make sure to have his back. To Lindz, T-rev, Trey, and Watson, you have kept me sane, in check, and laughing throughout this ride. Finally, to all of my friends that I don't have space to mention, you are all awesome! Remember that.

Contents

Chapter

Tables

Table

Figures

Figure

Chapter 1

Introduction

1.1 Motivation and Objective

In one of his famous dialogues, Plato said, "nothing without understanding would ever be more beauteous than with understanding." To me, this simple line points to the heart of what it means to be a scientist, i.e. to explain the unexplained and to discover the undiscovered. It is our duty and responsibility as scientists to look for unanswered questions and seek for the answers. The field of fluid mechanics is one where there often seems to be more questions than there are answers. It is only the most basic of problems that have analytic solutions and as you chip away each underlying assumption, less and less is known. As the range of scales becomes wider, and velocities begin growing, turbulence and chaos begins to onset, and even more is unknown, but we end up with a more accurate description of real flows. It is only though the constant methodical work done by the fluids community at large that we can hope to understand these mysteries and thusly unlock the secrets of the world around us.

The following project all began in the late 1800's with Lord Rayleigh. The story goes that he was puzzled by the exact way cirrus clouds were able to form and take the shapes that they did, so he set out to develop a theory for an incompressible fluid with a density jump under constant acceleration. Over time, further investigations have lead to the development and better understanding of the instability along with the realization of the plethora of physical scenarios in which similar flows occur. It has come to our understanding that the the Rayleigh-Taylor instability is the occurrence of a mean density gradient in the opposite direction of a gravity-like

body force, accelerating front, or local differential motion. If the interface is perturbed, this force then results in the generation of vorticity and continues growing and mixing in a non-linear fashion. This instability is found in many engineering applications at all scales from astrophysical flows to oceanic to geophysical, and it can even be commonly seen when doing something as simple as pouring cream into coffee.

The bulk of the previous work done, largely revolves around the analysis of immiscible and incompressible RTI's. Both experiments and numerical simulations have been carried out to try to characterize the effects of varying such things as the density difference at the interface and the initial perturbation applied. Approximating the initial growth regimes has been largely successful leading to good approximations of the growth rate for the bubbles and spikes as they move upwards and downwards in the system, respectively. Such phenomenon as the late time asymptotic growth, eventual approach to self similarity, merging of bubbles and spikes with multimodal perturbations, and the achievement of chaotic growth in high Reynolds number flows have all been documented and studied.

Though there have been many discoveries and many advancements over the history of studying RTI, there is still much to be found. In the physical world, RTI occur in very complex scenarios, most of which involve compressible and miscible fluids. Their background states and stratifications can wildly vary and many RTI occur in scenarios with external forcing from sources such as electromagnetism and reactions. Based on this, there is still much to be uncovered and much of the work is just unfeasible to do with experiments. This leaves us with the need to explore these regimes through numerical modeling. This project is designed to work on filling in the gaps in our knowledge base through the use of highly adaptive wavelet based numerical simulations.

In addition to understanding the complete, full system, it is also important to work towards simplified systems and the understanding of these in order to feed our knowledge of the larger system. Like a physicist explaining atoms through the approximation of balls and springs, finding simple analogs to further elucidate complex scenarios is imperative to the development of new models and techniques. It is known that RTI propagates fluid flow through the development and

propagation of vortical fields. Initially, these manifest themselves as either vortex pairs in two dimensions, or vortex rings in three. To help paint the entire picture of RTI development, a study into these reduced analogs of vortex pairs and rings is also presented and investigated through the use of wavelet based simulations.

1.2 Methodology

In order to complete these investigations, simulations must be carried out. Essentially, we have two options, to use modeling such as Large Eddy Simulations (LES), or to use Direct Numerical Simulations (DNS) [16]. The advantage of using modeling is that the simulations are inherently cheaper whereas DNS leads to better capturing of the physics. For RTI driven systems, there is a large range of scales that needs to be resolved and the multi-species nature leads to steep gradients developing causing this problem to be very difficult to model. With modeling, there has been some success, but in general the nature of RTI causes small scales to force large scale growth, which is opposite of what most models are built to do. In addition, previously untouched regimes are to be explored, and the models are not tailored to capture unknown new physics. Because of this, DNS is the only way we can be sure that we are accurately capturing and representing the flow fields.

To help alleviate the negative aspect of the simulations, using modern adaptive techniques to alleviate the costs is necessary [16]. Even though today we have access to cutting edge super computing power, it is still necessary to ensure that these resources are used efficiently so we can explore as many regimes as possible. The Parallel Adaptive Wavelet Collocation Method (PAWCM) lends itself naturally to flow simulations, especially localized flows such as the RTI, because it allows us to take advantage of the inherent aspects of the problem to create highly adaptive and compressed grids. This allows us to simulate these complex flows for significantly cheaper than a non-adaptive simulation. It is truly only through the use of such powerful techniques that we are able to explore new physics such as this.

1.3 Organization

The rest of the this document is ordered as follows. In Chapter 2, there is a thorough discussion on the background and current state of Rayleigh-Taylor instability research. It contains the relevant historical approximations and physical descriptions while also discussing the previous simulations and experiments that have been done. Chapter 3 then goes on to discuss the numerical method used to approach this problem with a brief section on other applications of the Adaptive Wavelet Collocation Method. Chapters 4-6 present the results of this research in the format of the papers that have been written about them, and thusly may contain some redundancy in the information presented because each was also written to stand on its own. Chapter 4 begins as a discussion of the results obtained from the isothermal single-mode simulations. Chapter 5 widens this scope to also investigating the isentropic and isopycnic initial stratifications while also comparing these with the isothermal. Chapter 6 presents results for the multi-mode isothermal stratification. Finally, Chapter 7 includes a discussion about the overall conclusions and the future work that is still to be done.

Chapter 2

Background

Rayleigh-Taylor instability has been a phenomenon experienced throughout all history and time. Any time we overturn a glass of water, pour water into oil, or add creamer to our favorite caffeinated beverage, we experience RTI. It wasn't until Lord Rayleigh became interested in understanding the physics behind the formation of cirrus clouds, though, that a mathematical definition of these motions was generated. Lord Rayleigh's paper in 1880 focused on the description of a heavier fluid on top of a light fluid where both are immiscible and in the presence of Earth's gravity [50]. Later, 1950 to be exact, Sir G.I. Taylor came through and expanded this theory to any general acceleration and not just our gravity [59]. From this, the instability was given its name. You can view an image of the two namesakes for this instability below in Figure 2.1. The rest of this section investigates the work that has already been accomplished since Lord Rayleigh and Sir Taylor began this research.

2.1 Overview of the Rayleigh-Taylor Instability

RTI by definition occurs when a light fluid supports a heavy fluid in the presence of a gravity like accelerative force, or alternatively, you can think about it as a light fluid pushing on a heavy fluid. This results in an acceleration in the opposite direction of a density gradient [10, 50, 59]. When the interface is perturbed, it results in the generation of small scale vorticity, in the form of a counter rotating vortex pair in two dimensions or a vortex ring in three, that continues to grow larger in time. This vorticity results in the propagation of the heavy fluid downwards in a

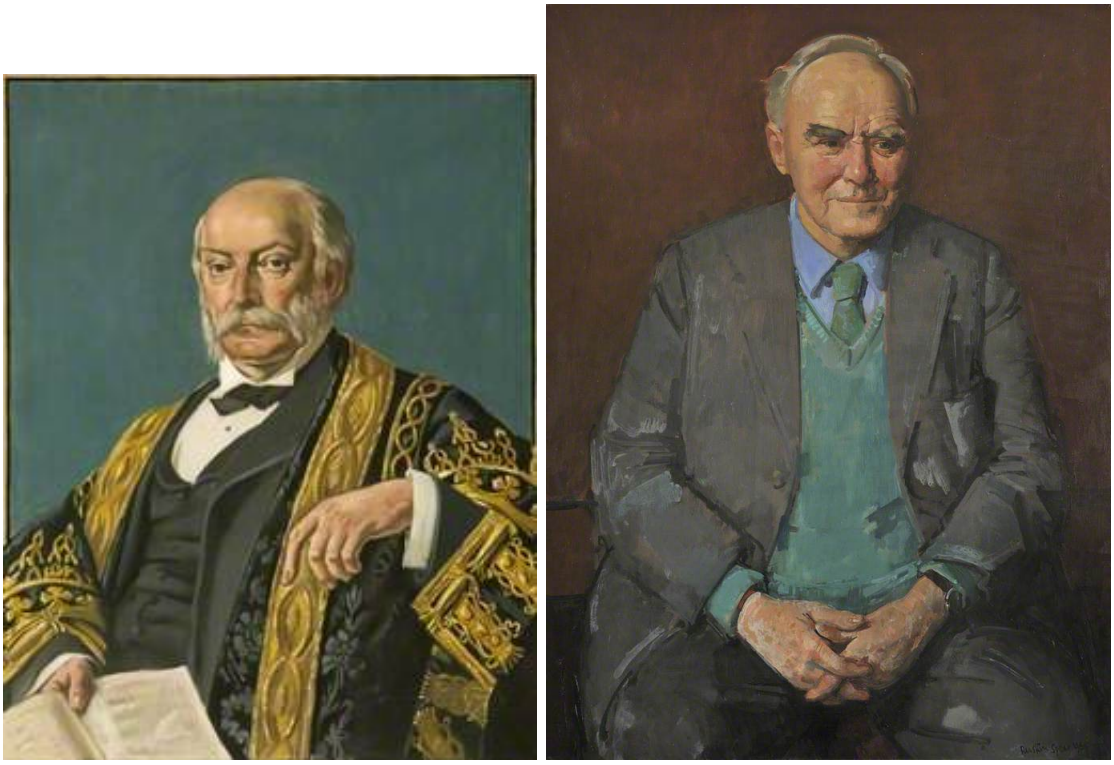

(a) Lord Rayleigh (b) Sir Taylor

Figure 2.1: The namesakes of the Rayleigh-Taylor Instability courtesy of Art UK (artuk.org).

"spike", while the light fluid is propagated upwards as a "bubble". Initially, the two motions are very similar, but as time progresses the bubble begins to widen at its tip while the spike begins to narrow, hence feeding the names given to them. As these motions continue, the shearing on the interfaces results in the generation of a Kelvin-Helmholtz instability and thusly the addition of more induced motion [64].

In large, the main defining characteristic of the instability is the intensity of the density jump at the interface. This is classified in the non-dimensional number known as the Atwood number, defined as the difference of the fluid densities divided by the sum of the fluid densities for the classical incompressible case. In more general terms, and thusly for the compressible case, this is defined synonymously by replacing the density with the molar mass of the fluids. Hence the Atwood number is defined as follows in 6.12.

$$A = \frac{W_2 - W_1}{W_2 + W_1}, \text{which in the incompressible limit becomes } A_{inc} = \frac{\rho_2 - \rho_1}{\rho_2 + \rho_1} \tag{2.1}$$

In this definition, the subscript 2 refers to the upper fluid while 1 refers to the lower fluid. In order to have the system be Rayleigh-Taylor unstable, it is required that $W_2 > W_1$ and equivalently that $\rho_2 > \rho_1$ at the interface. This puts the bounds on the Atwood number between 0 and 1 where close to 0 refers to a small difference in densities and 1 refers to an infinite difference in densities. As the Atwood number approaches 1, we expect to see the differences in the bubble and spike enlarge as we should see very wide and circular bubbles develop while the spikes become an extraordinarily narrow point. This leads to the spike moving further and faster downwards as it creates a jet-like effect in comparison to the bubbles movement. Conversely, as the Atwood number approaches 0, we should see very similar growth between the bubble and spike as both maintain a very similar shape and appearance somewhere in between rounded and pointed, while both maintain very similar growth rate and distance traveled. When thinking about multi-modal perturbations, these bubble and spike formations start off even smaller, but as the instability growth continues, they begin to join into even larger structures [57, 37].

One of the most interesting features of the RTI is that it occurs in a huge range of scales

and physical scenarios. On the largest side, RTI have been shown to affect how galaxies form, the transfer of plasmas in giant magnetospheres such as Jupiter's and Saturn's, and supernova explosions. An example of a nebula exhibiting RTI structures, namely the Crab Nebula, and a simulation from recent research exploring RTI in supernova explosions can be seen in Figure 2.2. Essentially for supernova, the core of a star will explode and send hot reacting gases from its center into a cloud of cooled gas. Because of the temperature difference, this results in the lighter and hotter gas pushing into the heavier and cooler gas creating RTI at the interface of reaction. The RTI is then able to act as a mixing mechanism for the system to allow unburnt reactants into the reaction zone to continue supplying it with fresh fuel. In the other astrophysical scenarios, namely magnetospheres and galaxies, magnetic fields cause the movement of dense plasmas from the interior of the system towards the exterior which has less dense plasmas pushing back [72, 35, 44, 19, 31, 33, 54, 28]. On the vastly opposite end from the astrophysical scale, is the scale of fusion

(a) Crab Nebula (b) Supernova Simulation

Figure 2.2: An example of a nebula exhibiting RTI characteristics and the results from a supernova simulation to study the effects of RTI on the growth of the flame front [33].

reactors. With our technology, it is feasibly impossible to achieve fusion without the introduction of RTI. In space, fusion is achieved because of the massive amount of mass a star has causing intense gravity to force fusion to happen. To try to recreate this in a lab, we cannot nearly achieve the levels of gravity needed, so instead, large amounts of kinetic energy must be applied to some fuel to force the fusion to happen. This is typically done through the use of magnetics or lasers. The magnetic case ends up similar to that of the astrophysical phenomenon already described. The method using

lasers is referred to as inertial confinement fusion and a schematic for how it works is shown in Figure 2.3 In this process, it is practically impossible to input the energy in a completely uniform

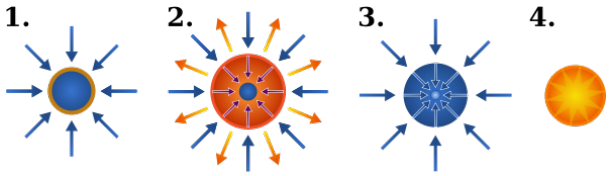

Figure 2.3: A schematic for inertial confinement fusion. (1) First lasers heat the exterior of the fuel pellet leading to (2) blow off and fuel compression. If done properly (3) the core will ignite finally resulting in (4) the thermonuclear burn that should output many times the input energy.

fashion because there will either be stronger inputs towards the center of the beam, imperfections in the fuel capsule, or the power of the individual beams will vary. This essentially then creates a perturbation that results in the generation of a RTI because of the vast differences in the densities between the burnt and unburnt fuels. As soon as the instability occurs, mixing begins to sap away the thermal potential making their performance less than desirable. Through the understanding of RTI in cases like this, the hope is to work towards minimizing this mixing thusly creating better thermonuclear fusion reactors [34, 7, 41].

These two scales present interesting engineering ideas and thoughts, but they occur in very nuanced and specific regimes. The exciting part about RTI is that it also occurs in everyday situations. The origins of this research began with clouds, and there are multiple atmospheric conditions that can lead to the generation of RTI with clouds in the atmosphere [9]. Essentially if a temperature inversion occurs, the atmosphere becomes RT unstable and if the conditions are right, this results in the shaping of clouds accordingly. In Figure 2.4, there are two examples of this, i.e. a mammatus cloud resulting from cool water vapor occurring above warm atmosphere, and also a volcanic ash mushroom cloud resulting from the intense heat from the volcano rising through the cooler air around it [56]. As mentioned previously, RTI can also occur in everyday scenarios like pouring creamer into coffee [54]. Because of its everyday occurrences, in classes such as Dr. Jean Hertzberg's Flow Visualization and for aspiring artists, RTI lends itself for the generation of

beautiful artwork since the experimental setup is quite easily obtainable. An example of this can be seen in Figure 2.5 where one of Dr. Hertzberg's students photographed a RTI created by pouring dyed milk into sugar water.

(a) Mammatus Cloud (b) Volcanic Mushroom Cloud

Figure 2.4: Examples of clouds being shaped by the development of RTI.

Figure 2.5: A RTI created and photographed for Dr. Jean Hertzberg's Flow Visualization class by Kyle Thatcher in 2014.

2.2 RTI Development and Analysis

To achieve RTI, we impose a heavy fluid above a light fluid, and perturb the interface. The perturbation then grows, but how does it grow? In general, the instability growth is described exactly the by compressible continuity, Navier-Stokes, energy, and species mass fraction equation. For the single mode situation, after any diffusion is allowed to take place, we know that initially the interface will grow according to linear stability theory in an exponential fashion. After this stage, the instability continues according to potential flow theory as the small scale vorticity begins to be generated. From there, the instability was originally believed to reach a terminal velocity [57, 38]. Recently, though, it has been shown that if the viscous effects are small enough, and the generation of vorticity is strong enough, then the instability will actually grow to reaccelerate [64]. From there, the continuous generation of additional vorticity from the Kelvin-Helmholtz instability causes the instability to proceed into a chaotic and turbulent like regime. A diagram of these regimes can be seen in Figure 2.6. The specific growth in any one of these regimes is characterized by many different parameters, such as compressibility, diffusivity, finite density gradients, surface tensions, and viscous effects to name a few [17, 36, 42, 23]. With the extension of the linear stability theory to the compressible regime, it has been shown that there is no single parameter to quantify the effects of such complex interactions on even the earliest growth regimes, let alone the even more complex late time growth [42].

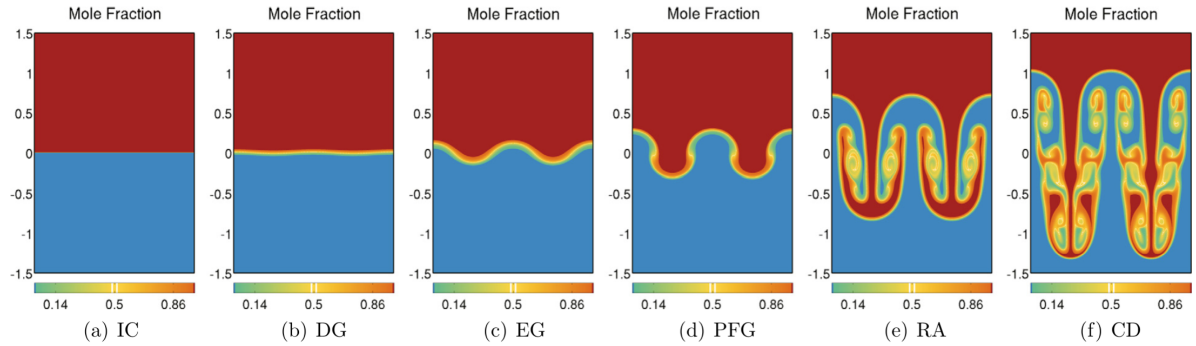

(a) IC (b) DG (c) EG (d) PFG (e) RA (f) CD

Figure 2.6: The stages of RTI growth. IC stands for initial conditions, DG diffusive growth, EG exponential growth, PFG potential flow growth, RA reacceleration, and CD chaotic development.

To further investigate these effects, I will give a short description on the derivation of the linear stability analysis and then the potential flow theory. To perform the linear stability analysis, the first step it so define all flow fields as a background state plus a perturbation. Essentially, this equates to defining any variable, u, as $u = u^0 + u'$ where u^0 is the base state and u' is the applied perturbation to this state. To arrive at an analytical solution, we can begin by looking at the incompressible result. For any given perturbation with wavenumber k, we know the interface location will follow the relationship

$$\eta_I(x_2, x_3, t) = \eta_A \exp\left(i(k_2 x_2 + k_3 x_3) + nt\right), \tag{2.2}$$

where the perturbation is only applied in the x_2 and x_3 direction, n is the growth rate, and η_A is the amplitude of the initial perturbation.This then results in the solution for the incompressible growth rate as

$$n_{inc} = \sqrt{Agk} \text{ where } k^2 = k_2^2 + k_3^2. \tag{2.3}$$

This solution then can be expanded on to include the effects of diffusivity and viscosity. This results in the determination that the upper limit for the growth rate is

$$n_{visc,diff} = \left(\frac{Agk}{\psi} + \nu^2 k^4\right)^{1/2} - (\nu + D)k^2, \tag{2.4}$$

where D is the mass diffusion coefficient, ν is the kinematic viscosity, and ψ is a function of A, k, and the initial diffusion thickness δ that is a purely empirical relation [17]. This equation succinctly shows that both viscosity and diffusion work to suppress the instability, especially at higher wavenumbers. While these relationships might be great at predicting the initial growth for incompressible cases in both simulations and experiments, we are in need of the inclusion of compressible effects.

Unfortunately, the inclusion of compressibility results in great difficulty in deriving analytic relations. In order to uncover an analytical solution, we must make the assumptions that the fluids are inviscid, immiscible, and lack both heat diffusion and surface tension effects [42]. This

essentially leaves us with a simplified set of governing equations that is as follows.

$$\frac{\partial \rho}{\partial t} + \frac{\partial \rho u_j}{\partial x_j} = 0, \tag{2.5}$$

$$\frac{\partial \rho u_i}{\partial t} + \frac{\partial \rho u_i u_j}{\partial x_j} = -\frac{\partial p}{\partial x_i} - \rho g_i, \tag{2.6}$$

$$\frac{\partial p}{\partial t} + \frac{\partial p u_j}{\partial x_j} = (1-\gamma) p \frac{\partial u_j}{\partial x_j} \tag{2.7}$$

where $g_i = g_1 = g$ is gravity, p is pressure, u_i is velocity, and ρ is density. From here, we want to seek solutions in the form of that for the position of the incompressible interface η_I, namely, the form $\exp(i(k_2 x_2 + k_3 + x_3) + nt)$. Assuming this relationship, we end up with the solutions

$$n\rho = -\rho_0 \left(\frac{\partial u_1}{\partial x_1} + i(k_2 u_2 + k_3 u_3) \right) - u_1 \frac{\partial \rho_0}{\partial x_1}, \tag{2.8}$$

$$\rho_0 n u_1 = -\frac{\partial p}{\partial x_1} - g\rho, \tag{2.9}$$

$$\rho_0 n u_2 = -i k_2 p, \tag{2.10}$$

$$\rho_0 n u_3 = -i k_3 p, \tag{2.11}$$

$$np = -\gamma p_0 \left(\frac{\partial u_1}{\partial x_1} + i(k_2 u_2 + k_3 u_3) \right) + u_1 \rho_0 g, \tag{2.12}$$

where the subscript 0 implies the unperturbed state. From this, we can rearrange and work on eliminating variables so that we end with an equation for u_1. Keeping in mind that on either side of the interface, our local speed of sound, $c = \sqrt{\gamma \frac{p_0}{\rho_0}}$, is constant and we have a jump condition at the interface, we end up with the relationship of

$$\frac{\partial^2 u_{1_m}}{\partial^2 x_1} - \frac{\gamma_m g}{c_m^2} \frac{\partial u_{1_m}}{\partial x_1} - \left(k^2 + \frac{n^2}{c_m^2} + \frac{(\gamma_m - 1) g^2 k^2}{n^2 c_m^2} \right) u_{1_m} = 0, \tag{2.13}$$

where the subscript m refers to the fluid species. The solution must take the form of $u_{1_m} = A_m \exp(\lambda_{1_m} x_1) + B_m \exp(\lambda_{2_m} x_1)$ where

$$\lambda_{1,2_m} = \frac{\gamma_m g}{2c_m^2} \pm k\sqrt{1 + \frac{n^2}{k^2 c_m^2} + \frac{(\gamma_m - 1)g^2}{n^2 c_m^2} + \frac{\gamma_m^2 g^2}{.} 4k^2 c_m^4} \tag{2.14}$$

Finally, from this we can use our definition of u_1, the boundary conditions that $u_1 = 0$ at $\pm\infty$, the fact that u_1 must be continuous, and its jump condition to solve for the growth rate n. With this we arrive at

$$n_{comp,inv}^2 = k^2 g \left(\frac{\gamma_2(k^2 c_1^2 + n_{comp,inv}^2) - \gamma_1(k^2 c_2^2 + n_{comp,inv}^2)}{\gamma_1(k^2 c_2^2 + n_{comp,inv}^2)\lambda_{1_1} - \gamma_2(k^2 c_1^2 + n_{comp,inv}^2)\lambda_{2_2}} \right) \tag{2.15}$$

From this, we can then go back and obtain the perturbation fields from earlier [42]. There has also been work done to extend these results to the case where the thermodynamics are not in equilibrium. These results end with a similar expression except it does not provide an explicit analytical solution except for in two limiting cases. These cases are when the thermodynamics are in near equilibrium, where it reduces to the same expression as above, or when the thermodynamics are so out of equilibrium that the resulting equations are dominated by the temperature gradient effects. This solution though, is cumbersome and does not add any real importance to this report, so it is omitted [23].

To further our investigation into the growth of the RTI, we must progress into the non-linear regime where the early stages can be predicted using potential flow theory. The previous results show the growth rate for any arbitrary perturbation wavenumber, k, but to continue on, it is imperative to make the assumption that the instability only has a single mode. Though this is inconsistent with any real system found in nature, it is the only true way to proceed with the analysis and is still useful for obtaining an upper bound for the predicted terminal velocities from this method. To continue with the examination of the growth, we must first define a velocity potential, $u_i = \nabla\phi$, and assume we are near the $A = 1$ limit [37]. This analysis can proceed in either two dimension or three, but will be presented in two and the extension to three dimensions will be discussed. Assuming gravity in the x direction, the velocity potential is defined as

$$\phi(x, y, t) = a(t)\cos(k(y - y_0))\exp(-k(x - \eta_0)) \tag{2.16}$$

where the tip of the bubble is defined to be at (y_0, η_0) at a given time, and k is the wavenumber of the applied perturbation. This potential must satisfy the Bernoulli equation, i.e.

$$\frac{\partial \phi}{\partial t} + \frac{1}{2}(u^2 + v^2) + gx = C \tag{2.17}$$

where C is a constant on the interface, and u and v are the velocities in the x and y direction, respectively. The interface location is defined by

$$x = \eta_I(y,t) = \eta_0 + \eta_2(t)(y - y_0)^2 \tag{2.18}$$

where the subscript I refers to at the interface, y_0 and η_0 are still the location of the tip, and η_2 is defined by the radius of curvature R such that $\eta_2 = -1/2R$. To solve this system, we need one more equation, and the comes in the for of the kinematic equation to describe how the interface moves with the fluids. This equation is

$$u_I - \frac{\partial \eta_0}{\partial t} - \frac{\partial \eta_2}{\partial t}(y - y_0)^2 - 2\eta_2(y - y_0)(v_I - \frac{\partial y_0}{\partial t}) = 0, \tag{2.19}$$

and the same definitions are used as above. When we combine all of these equations together, we get the system

$$ak + \frac{\partial \eta_0}{\partial t} = 0, \tag{2.20}$$

$$ak^2\left(\eta_2 + \frac{k}{2}\right) - \frac{\partial \eta_2}{\partial t} + 2ak^2\eta_2 = 0, \tag{2.21}$$

$$\frac{\partial a}{\partial t}k\left(\eta_2 + \frac{k}{2}\right) - \frac{a^2k^4}{2} - g\eta_2 = 0. \tag{2.22}$$

From here, we can use standard techniques for solving a system of ordinary differential equations. By combining 2.20 and 2.21 we can arrive at a relationship between the bubble height and curvature of the system. This results in the relationship

$$\frac{\partial \eta_0}{\partial t} = -\left(\frac{2}{k(k + 6\eta_2)}\right)\frac{\partial \eta_2}{\partial t} \tag{2.23}$$

which gives way to the solution

$$\eta_0(t) = -\frac{1}{3k}\ln(k + \eta_2(t)) + C. \tag{2.24}$$

If we consider η_0 to be initially small such that $\eta_0(t = 0) << 1$, then we can solve for the constant and arrive at the actual solution. This comes out to be

$$\eta_2(t) = -\frac{k}{6} + \left(\frac{k}{6} - \frac{k}{2}\eta_0(0)\right)\exp(-3k(\eta_0(t) - \eta_0(0))) \tag{2.25}$$

From this relation, we can predict the asymptotic behavior of the curvature of the bubble. By letting η_0 go to ∞, it is clear that η_2 goes to $-k/6$, and form there the radius of curvature, R, can be obtained. This same process can be repeated but by combining 2.22 with 2.20. With the addition that the terminal velocity of the bubble is defined as

$$V_b = \frac{\partial\phi}{\partial x} = -ak \text{ at the bubble tip.} \tag{2.26}$$

We can then arrive at the result that for two dimensional flow, the terminal bubble velocity, $V_b = \sqrt{\frac{g}{3k}}$. We can then repeat this process but expand everything into three dimensions with axial symmetry and cylindrical coordinates. Overall, the process remains largely the same and we arrive at a similar results, i.e. $V_b = \sqrt{\frac{g}{k}}$. This immediately shows the result that by switching from two to three dimensions, we should expect the velocity to increase. This is attributed to the fact that in three dimensions, there is a reduced amount of drag per unit volume on the growth of the bubble [37].

The next step is to try to extend these findings to any generic Atwood number instead of assuming $A = 1$. To do this, the simplest way is to consider a buoyancy-drag model [48]. These models relate the velocity of the bubble or spike to a force balance equation that includes buoyancy and drag with the inclusion of the inertia of the system. This balance becomes the equation

$$\left((\rho_{in} + C_a\rho_{out})\frac{dV}{dt} - \beta(\rho_{out} - \rho_{in})g\right)[\text{Volume}] = -C_d\rho_{out}V|V|[\text{Area}] \tag{2.27}$$

where V represents the velocity of either the spike or the bubble, ρ_{in} is the velocity of the feature of interest, i.e. $\rho_{in} = \rho_2$ for the spike and ρ_1 for the bubble whereas ρ_{out} becomes the density of

the other, C_a is a mass effect caused by the displacement of fluid, and C_d is the coefficient of drag. Both C_a and C_d are dependent on the shape and thusly volume of the moving fluid, and β is a parameter allowing us to account for the mixing of the two fluids at the interface . Essentially, $\beta = 1$ represents the immiscible case and $\beta < 1$ allows us to investigate effects of diffusion [15]. To determine the terminal velocities, all we must do is take the limit as t goes to ∞. When this limit is achieved, and we assume immiscible fluids, the time derivative naturally goes to zero and we are left with the equation

$$(\rho_{out} - \rho_{in})g[\text{Volume}] = -C_d \rho_{out} V_m^2 [\text{Area}]. \tag{2.28}$$

This limit occurs when the height of the instability reaches about one wavelength, λ, so we can take the ratio of the area and volume to be $1/\lambda$ leaving us with the equation $(\rho_{out} - \rho_{in})g = -\frac{C_d}{\lambda}\rho_{out} V_m^2$. From this we can rearrange the equation and invoke the definition of the Atwood number to arrive at an equation for the terminal velocity of either the bubble or spike. This equation is

$$V_{b,s} = \left(\frac{2Ag\lambda}{(1 \pm A)C_d} \right)^{1/2} \tag{2.29}$$

This result has also been expanded on to account for more general conditions such as in [25].

The final stage of the instability that has been explored analytically is the onset of self-similarity. Essentially, the idea is that in the perfect case of pure RTI, as the flow progresses the initial conditions are forgotten. As a random perturbation proceeds to grow, the various modes begin coalescing to form larger modes. The high wavenumber modes start coupling and forming into low wavenumber modes and these low wavenumbers begin to dictate the growth of the instability, pushing it towards a single mode growth. This self similar regime is only supposed to happen when the dominant wavelength is significantly greater than the largest wavelength from the initial perturbation, but once this is achieved all memory of the initial state is said to be lost [12].

If the memory is truly lost, then it stands to reason that the growth rate must only depend on the the density difference between the fluids, i.e. the Atwood number, the strength of the acceleration being applied, and time. Using this dimensional reasoning it should stand true that the growth height a bubble, h_b, becomes a function of only those parameters, i.e. $h_b = h_b(A, g, t)$.

From this we can surmise that the length scale to relate the height to will be gt^2 thusly leaving us with the equation for the dominant bubble height as $h_b = f(A)gt^2$. To solve for this equation, we must first note that it requires that the bubble height, h_b, the bubble diameter, D_b, and the dominant wavelength, λ_b, all be proportional to each other. From here we note that the time for a wavelength to become dominant, t_b must be equal to a number of linear growth periods N_b, where $N_b = n_b t_b$. The linear growth rate, n_b is thusly derived from linear stability theory to $n_b = \sqrt{2\pi Ag/\lambda_b}$. When we combine all of this information together and solve for the dominant wavelength, we are left with

$$\lambda_b = \frac{2\pi}{N} Agt^2. \tag{2.30}$$

We know that the height of the growth must be proportional to the dominant wavelength giving the expression for the bubble height, h_b, as

$$h_b = \alpha Agt^2 \tag{2.31}$$

where α is some non-dimensional growth parameter [5]. If we were to do this same analysis for a spike, we would find that for low Atwood numbers, where the spike and bubble are nearly identical, the spike growth rate h_s equals the bubble growth rate h_b. As we increase A, though, this approximation becomes poor. The drag on the spike becomes significantly reduced leaving it to achieve near free fall velocities. In the end, though, finding the growth parameter, α has been the goal of many research efforts [6, 4, 16, 48, 70]. To this day, there still remains discrepancy over what α should be, and it is nearly impossible to tell if a simulation or experiment has truly "lost all memory of its initial conditions," to determine if the analysis is fitting.

2.3 Modern Experiments and Simulations of the Rayleigh-Taylor Instability

There is constantly more research going on in the world of RTI, and my goal here is to highlight just a few of the things that are currently being worked on or have recently been published both computationally and experimentally. The goal is that the research directly related to this project investigating late time effects of compressibility on low Atwood RTI will be presented. The

first important work was done to classify the growth stages of incompressible, miscible, low Atwood number RTI flows. Essentially, these were the incompressible simulations that the simulations presented later were based off of. It involved simulating $A = 0.04$ RTI until extremely late times at Reynolds numbers that had not been touched before. This was the research that discovered the existence of the reacceleration and chaotic growth regime. Essentially, it was found that during the early stages of growth, i.e. diffusive, exponential, and potential flow, the vorticity dynamics are small, but as the late time is entered the vorticity dynamics grow. A new definition for the Reynolds number,i.e. the perturbation Reynolds number: Re_p, was defined and found that at values of $\mathcal{O}(10^4)$ or greater the viscous effects are low enough to allow the late time generation of vorticity to cause the reacceleration and chaotic development of the instability [64].

One of the current gold-standards for computational simulations of RTI arises from the Alpha-group collaboration which consisted of a large group effort to try to better characterize α. The team used seven different numerical frameworks, TURMOIL3D, FLASH, WP/PPM, NAV/STK, RTI-3D, HYDRA, and ALEGRA, to run high Reynolds number simulations until late times to perform this study. All but one of these codes works by using a compressible solver and working in the near incompressible limit, so small compressibility effects may be present. Also, all of the codes use a version of LES that is total variation diminishing, namely MILES or monotone integrated LES. In addition to this, they all worked with the Euler equations, allowing only the numerical diffusion to dissipate the energy from the small scales. Though they completed some of the most advanced simulations to date, they still obtained a value for α roughly 40% less than what is found in experiments. Because of the schemes used, it is unknown whether these results are perfectly reproducible via DNS, but DNS would be the way to improve on them [16].

Lafay, et al. have been a group that has also been working on the numerical and theoretical side of compressible, miscible RTI growth. For their main study, they have two approaches, first to vary a stratification parameter related to the gradient of density, and secondly, to explore the effects of changing the ratio of specific heats, γ, between the two fluids. Their work stayed in the low Reynolds number region, keeping it at 1000, while they studied these effects on RTI with

Atwood number of 0.25. In this situation, the simulations were only carried out in two dimensions and were incapable of making it into the reacceleration regime with their high viscous dissipation. In general they found that compressibility tended to lower the growth rates of the instability. The only exception was when allowing the heavy fluid to become very incompressible, i.e. large γ, while allowing the light fluid to become largely compressible, i.e. small γ, the most unstable state was achieved in which the highest growth rate was seen. In general, though, they found that increasing compressibility led to a decrease in mean vorticity. They then went on to explore the multi-modal regime, where it was found that even at very high Reynolds numbers, the background stratification is able to suppress the instability eventually causing it to form a decaying mixing layer which slowly dissipates the kinetic energy [36, 20, 21].

Wykes, et al. at Cambridge have recently done exciting experimental work in the realm of miscible and stratified RTI growth. Though they use incompressible fluids and induced stratification through salinity, the background stratification is remarkably similar to that of which we see in our compressible isothermal states. For their studies, Atwood number varied from trial to trial, but it remained very small around 0.005 to 0.01. The main purpose of their investigation was to determine the mixing efficiency, and they found that in general, RTI would cause a very high mixing efficiency, i.e. 95%, in the central region of the stratified fluid. The end result is that the instability grows to some height inside of which the fluid is mixed well. This then results in the development of a stable stratification and the instability is suppressed [13].

There are numerous other areas of active research going on right now in the RTI community that simply do not hold much relevance to this project, or I do not have time to get into great detail on. Some of these are presented here with a very short synopsis. There is a group looking into the effect of electric fields on dielectric fluids exhibiting RTI[69]. There is effort to characterize the coupled Kelvin-Helmholtz and RT instabilities and quantify the transition between the two through experiments[2]. A combination effort to use experiments and numerical models to characterize the convective and diffusion terms exists to show that the lateral movement of bubbles and spikes is potentially due to diffusion [26]. The effects of miscibility and forced or natural perturbation

application is being looked into [53]. A group is seeing how the instability changes when the density difference is caused by the heavy fluid containing suspended particles [11]. All of these things lead to very different results and are helping to push the field forward while uncovering new interactions.

Chapter 3

Simulation Setup and Numerical Method

The Rayleigh-Taylor instability presents many challenges that lend itself to be difficult to characterize. In the compressible regime, there are many parameters and intertwined effects that are not well understood [43, 42]. Because of this it is important to isolate any individual parameters possible to try to understand the effect of each. Doing this and maintaining known perturbations is a huge challenge for experimentalists, whereas getting the exact initial conditions wanted is easier to do in a computational world. In order to effectively explore the parameter space we have provided, it is necessary to try to run these simulations as efficiently as possible and thusly advanced adaptive numerical techniques should be employed. This chapter explains the numerical method chosen to run these simulations and details the setup of the simulations themselves.

3.1 Governing Equations, Initial Conditions, and Non-dimensional Parameters

The simulations have been performed using the standard multi-species compressible fluid dynamics equations. The full system of equations is[43, 68]:

$$\frac{\partial \rho}{\partial t} + \frac{\partial \rho u_j}{\partial x_j} = 0, \tag{3.1}$$

$$\frac{\partial \rho u_i}{\partial t} + \frac{\partial \rho u_i u_j}{\partial x_j} = -\frac{\partial p}{\partial x_i} - \rho g_i + \frac{\partial \tau_{ij}}{\partial x_j}, \tag{3.2}$$

$$\frac{\partial \rho e}{\partial t} + \frac{\partial \rho e u_j}{\partial x_j} = -\frac{\partial p u_i}{\partial x_i} - \rho u_i g_i + \frac{\partial \tau_{ij} u_i}{\partial x_j} - \frac{\partial q_j}{\partial x_j} + \frac{\partial c_{pl} T s_{jl}}{\partial x_j}, \tag{3.3}$$

$$\frac{\partial \rho Y_l}{\partial t} + \frac{\partial \rho Y_l u_j}{\partial x_j} = \frac{\partial s_{jl}}{\partial x_j}, \tag{3.4}$$

where ρ is density, p is pressure, T is temperature, u_i is the velocity in the x_i direction, Y_1 is the mass fraction for the bottom fluid, Y_2 is the mass fraction for the top fluid, R is the gas constant, and the ideal gas law $p = \rho RT$ is enforced. Repeated indices imply summation. The specific total energy is

$$e = \frac{1}{2} u_i u_i + c_p T - \frac{p}{\rho}, \tag{3.5}$$

the viscous stress is assumed to be Newtonian and is

$$\tau_{ij} = \mu \left(\frac{\partial u_i}{\partial x_j} + \frac{\partial u_j}{\partial x_i} - \frac{2}{3} \frac{\partial u_k}{\partial x_k} \delta_{ij} \right), \tag{3.6}$$

the heat flux is written as

$$q_j = -k \frac{\partial T}{\partial x_j}, \tag{3.7}$$

and the species mass flux is defined as

$$s_{jl} = \rho D \frac{\partial Y_l}{\partial x_j}. \tag{3.8}$$

From here, we can initialize the simulation. The upper fluid occupies the space where x_1 is greater than 0, and the lower fluid occupies where it is less than zero. This puts the interface right at $x_1 = 0$ where the species mass fraction is smoothed using the error function since it is the exact solution to the diffusion equation between the species. For the RTI to be present, it is required that the density (for the incompressible case) or the molar mass (compressible case) be greater in the upper fluid than the lower fluid, i.e. $W_1 < W_2$. The difference between these two is typically measured by a non-dimensional parameter called the Atwood number,

$$A = \frac{W_2 - W_1}{W_2 + W_1}. \tag{3.9}$$

For this study, the majority of the fluid properties were taken to be the same between the two species for simplicity. This includes the dynamic viscosity, μ, the heat conduction coefficient, k, the mass diffusion coefficient, D, and the gravitational acceleration, g_i, which is taken to only act in the vertical, x_1, direction. Finally, the gas constants are found based on the molecular weight as

$$R = \mathcal{R}\frac{Y_l}{W_l}, \tag{3.10}$$

where $\mathcal{R}$ is the universal gas constant. Following from this, c_p is calculated as an average as well, i.e. $c_p = c_{pl}\, Y_l$,.

Compressibility can be characterized by several parameters [42, 43]. Here, we are mainly concerned with flow compressibility. In this case, the corresponding incompressible limit can be obtained by increasing the speed of sound through increasing the background pressure (or temperature), such that the densities are not affected. The Mach number associated with this compressibility aspect is defined as the ratio of the gravity wave speed, $\sqrt{g\lambda}$, and the isothermal speed of sound, $a_0 = \sqrt{\frac{p_I}{\rho_I}}$, at the interface. This gives the definition of M as:

$$M = \sqrt{\frac{\rho_I g\lambda}{P_I}}, \tag{3.11}$$

where the subscript I implies interfacial. The interface density, ρ_I, is found with

$$\rho_I = \frac{\mathcal{R}T_I}{p_I}\left(\frac{W_1 + W_2}{2}\right). \tag{3.12}$$

Since the background state needs to be in hydrostatic equilibrium away from the interface, the Mach number defined above also characterizes the background stratification. The simulations presented have the same ρ_I (which fixes the Atwood number), perturbation wavelength λ, and g, so that varying M results in a change of p_I and subsequently T_I. To further elaborate on the available parameters, Table 3.1 has a collection of all the non-dimensional parameters that are used to characterize these simulations. Also included is the range of values used for the simulations presented later.

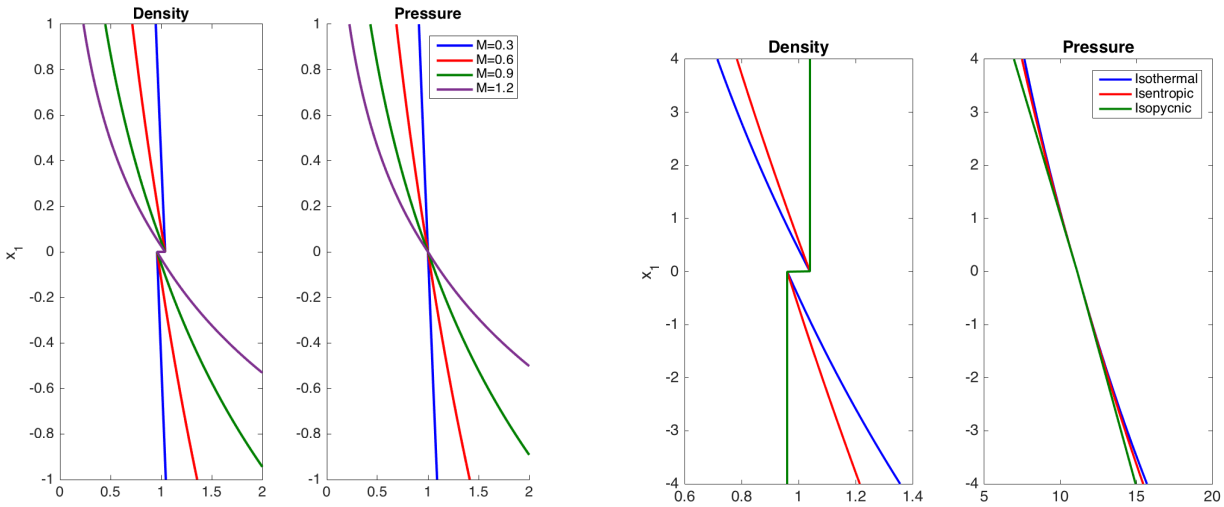

(a) Isothermal Stratifications by Mach number

(b) Stratifications by state for $M = 0.3$

Figure 3.1: Density and pressure stratifications for $A = 0.04$ as both a function of Mach number and stratification type.

Parameter	Definition	Description	Range
Atwood	$A = \frac{W_2 - W_1}{W_2 + W_1}$	Density jump	0.04
Mach	$M = \sqrt{\frac{\rho_I g \lambda}{p_I}}$	Compressibility + stratification	0.3-1.2
Perturbation Reynolds	$Re_p = \sqrt{\frac{Ag\lambda^3}{(1+A)\nu^2}}$	Viscosity	5,000-20,000
Schmidt	$Sc = \frac{\rho_I \mu_I}{D_I}$	Mass diffusivity	1.0
Prandtl	$Pr = \frac{c_{p_I} \mu_I}{k_I}$	Thermal diffusivity	1.0
Froude	$Fr = \frac{U_0}{(gL)^1/2)}$	Gravitational effects	1.0
Specific Heat Ratio	$\gamma = \frac{c_{p_I}}{c_{v_I}}$	Compressibility	1.4

Table 3.1: A synopsis of the relevant non-dimensional parameters and their respective meanings and values.

In order to remain consistent with the governing equations, the initialization of the background state must satisfy the hydrostatic equation, namely,

$$\frac{\partial p}{\partial x} = -\rho g. \tag{3.13}$$

This leads to the possibility of many different initial states. For this study, three different sets of stratifications were used to initialize the simulations, namely isothermal, isentropic, and isopycnic. Each one of these conditions isolates a field of interest, and minimizes its effects by leaving it constant while allowing the other states to vary. It it important to note that isobaric initial conditions are impossible to generate in a fashion consistent with the governing equations. For the isothermal stratification, the density and pressure fields are

$$p(x_1) = p_I \exp\left(-\frac{g x_1}{R_l T_I}\right), \tag{3.14}$$

$$\rho(x_1) = \frac{p_I}{R_l T_I} \exp\left(-\frac{g x_1}{R_l T_I}\right), \tag{3.15}$$

where in this case T_I is not only the temperature for the interface, but is constant in the whole domain. For the isentropic case the stratification is defined as

$$p(x_1) = p_I \left(1 - \frac{\gamma}{\gamma - 1} \frac{g x_1}{R_l T_I}\right)^{\left(\frac{\gamma}{\gamma - 1}\right)}, \tag{3.16}$$

$$\rho(x_1) = \rho_l \left(1 - \frac{\gamma}{\gamma - 1} \frac{\rho_l g x_1}{p_I}\right)^{\left(\frac{1}{\gamma - 1}\right)}, \tag{3.17}$$

and the temperature field is set to satisfy the equation of state. Finally, for the isopycnic case, ρ is set to be constant above and below the interface and the pressure field is set as

$$p(x_1) = -\rho_l g x_1 + p_i, \tag{3.18}$$

where p_i is added to ensure that it maintains the right interface pressure and T is again set to satisfy the equation of state. An example of the different stratifications can be seen in Figure 6.1.

Finally, to begin the RTI simulations, either a single-mode small amplitude velocity perturbation or a linear combination of randomized perturbations with random amplitudes and random phase shifts for the multi-mode perturbation is applied directly at the interface. The simulation is then carried out from that state [52].

3.1.1 Vortex Analogs

As RTI develop, one of the key features in their growth is the development of vortical structures[43, 64]. In two dimensions this first manifests itself as the formation of a pair of counter rotating vortices while in three dimensions, it manifests as a vortex ring. This transformation from the initial perturbation to these vortical structures is what ends up driving the instability. As it continues to grow, this first vortical structure remains intact, and sheds additional vorticity along the sides of the bubble and spike to form the Kelvin-Helmholtz instability. For this reason, these initial vortical structures are imperative to the growth of the RTI.

To further understand the effects of compressibility and background stratifications on the growth of RTI, an investigation into the effects onto these vortical structures by themselves can be carried out. To perform these simulations, a similar methodology is carried out to initialize them as the RTI. The same background state is used as the RTI case but with $A = 0$ so that there is no density discontinuity in the domain. The same non-dimensional parameters are all used to describe the vortex analog case so that the comparison can be one to one.

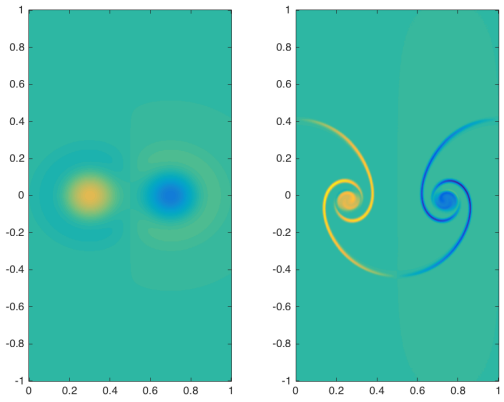

Figure 3.2: A comparison of the initial velocity field for the vortex pair simulations and the resulting velocity field from the development of the vortex pairs through RTI.

To complete the initialization, an imposed velocity field must be applied. For the vortex pair the initialization is

$$u_1 = -\sum_{i=1}^{2} \frac{\Lambda}{\sigma^2}(x_2 - x_{2,i})\exp\left(-\frac{(x_1 - x_{1,i})^2 + (x_2 - x_{2,i})^2)}{\sigma^2}\right) \tag{3.19}$$

$$u_2 = \sum_{i=1}^{2} \frac{\Lambda}{\sigma^2}(x_1 - x_{1,i})\exp\left(-\frac{(x_1 - x_{1,i})^2 + (x_2 - x_{2,i})^2)}{\sigma^2}\right) \tag{3.20}$$

so that the velocities are described by a Gaussian distribution with the summation being for the two different vortices [62]. The center of each vortex is located at $(x_{1,i}, x_{2,1})$, and the width is described by σ. The strength of the vortex pair, Λ, is set so that the circulation over each vortex matches that of the vortices generated by the RTI. A comparison of the velocity fields for the vortex pair case and two dimensional RTI case can be found in Figure 4.2. For the vortex ring case, the velocities are set similarly, i.e. they are also defined by a Gaussian distribution, but instead, it is based on the radius away from the center as if in cylindrical coordinates.

3.2 Parallel Adaptive Wavelet Collocation Method

The RTI problem lends itself naturally to state-of-the-art adaptive numerical methods. To effectively capture the instability growth, very long domains are needed to ensure late-time growth

is captured, but very small grid spacing is needed to fully resolve the high gradients at the interface of the instability. This would equate to having a very dense grid and incredibly high computational costs with traditional methods. During the majority of the simulation, however, the grid far away from the interface is unnecessary, and thusly, through the use of adaptive methods, high grid compression rates can be achieved. A method that has proven effective at doing this, is the Parallel Adaptive Wavelet Collocation Method (PAWCM), and it is what has been applied here[51, 52].

PAWCM uses the natural properties of the wavelet transformation to locate areas of steep gradients and gives direct control over the amount of resolution applied based on how steep these gradients are. Essentially, through PAWCM a flow field variable is transformed into wavelet space resulting in wavelet basis functions and coefficients that are localized in both wavelet and physical space. From there, the coefficients are passed through a thresholding filter where all the coefficients above the parameter ϵ are kept, and any of those below are set to zero. The resulting thresholded decomposition appears as follows

$$u_{\geq}(x) = \sum_{k} c_k^0 \phi_k^0(x) + \sum_{j=0}^{\infty} \sum_{\mu=1}^{2^n-1} \sum_{\substack{l \\ |d_l^{\mu,j}| \geq \epsilon ||u||}} d_l^{\mu,j} \psi_l^{\mu,j}(x), \tag{3.21}$$

where u is any variable, ϕ_k are the scaling functions on the coarsest level, c_k are the corresponding coarse level wavelet coefficients, ψ_l are the scaling interpolating functions on any arbitrary level, d_l are the coefficients that the thresholding is applied to, l and k represent physical grid points, and μ and j represent the wavelet family and level of resolution, respectively [61, 47]. The equivalence of setting one of these coefficients, d_l, to zero is the removal of a grid point at that level of resolution. d_l itself is a large value when in the presence of a large gradient at the given level, j or j-level, of resolution, and is small when it is in a relatively constant region. In addition to these points, when dealing with a field that changes in time, a buffer zone of the points on the same j-level around the significant point are kept as well. This method results in the error being of the order of which we set ϵ. An example of applying this method to a test function can be seen in Figure 3.3. In this image, PAWCM is applied to a hyperbolic tangent function. The entire grid for the given j-levels is shown, and then the same grid is shown with the points that have significant coefficients at their

respective j-levels highlighted in red. As expected, more points at higher j-levels are used as we approach the region of high variability, and then less are used as we move passed it [61, 55, 47].

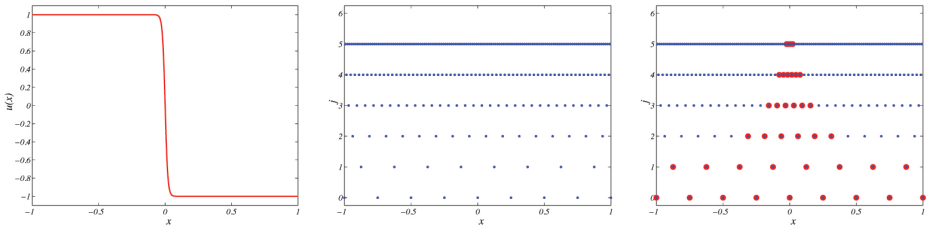

(a) A hyperbolic tangent function (b) Wavelet coefficient locations (c) Wavelet-threshold filter locations

Figure 3.3: An example of the application of the Adaptive Wavelet Collocation Method to a test function. On the left is the test function, the middle shows all of the grid points for j-levels up to 6, and the right highlights which points would have a coefficient above ϵ in red.

PAWCM has been implemented in a way that enables it to work with finite difference methods. For this method, fourth order central differences have been applied spatially, and a third order total variation diminishing explicit Runge-Kutta method scheme has been applied in time. PAWCM also boasts many modern features besides its adaptivity to enable fast and efficient processing. It is highly parallelized, having successfully run on up to 5000 cores with decent scaling, and it is able to do arbitrary domain decompositions using the Zoltan library. It has a tree-like data structure for easy MPI communications, and direct error control. All of this results in the fact that any additional overhead that arises from the wavelet methodology, is made up for by using many processors and a maintaining 90%+ grid compression[61, 55, 47].

To effectively capture these simulations, proper boundary conditions must be used. On the boundaries all sides that can be taken as periodic are, i.e. the boundaries in the x_2 and x_3 directions. In the x_1 direction, at the top and bottom of the domain, careful thought must be given to the boundary conditions implemented. The goal is to essentially mimic an infinite domain, but to ensure both the background stratification is preserved and that none of the shocks are reflected back into the domain. To do this, shear free slip boundary conditions were put in place with the addition of numerical diffusion buffer zones before them. These buffer zones ensure that any

shockwaves sent to the boundaries are dissipated before reaching the end which guarantees that issues won't arise as the waves try to leave the domain. Also, the waves are fully dampened so no reflections can take place[52].

3.3 Resolution Requirements

To ensure the simulations are fully resolved, a resolution convergence study was completed for both the maximum j-level and for the thresholding parameter, ϵ. The results for the ϵ study can be seen in Figure 3.4 and for the j-level in Figure 3.5. To accomplish this, first the grid resolution is held constant and ϵ is varied to arrive at a converged value of 10^{-3}. Next, the ϵ value is held constant at this converged quantity, but the resolution is varied by changing the maximum allowed j-level. Effectively, increased or decreasing the j-level by one either increases or decreases the maximum resolution by a factor of 2 in each direction, respectively. Through this it becomes clear that convergence is reached when $j_{max} = 6$ [52]. The puzzling part, is that even when these criteria are met it is still possible to introduce extremely small scale error that propagates through time and causes the introduction of secondary modes. The result of this can be seen in 4.5 in which the instability displays proper growth rates by looking at the maximum bubble and spike tips, but secondary modes cause the point at which the tip should be to invert. [htp] [htp] As mentioned

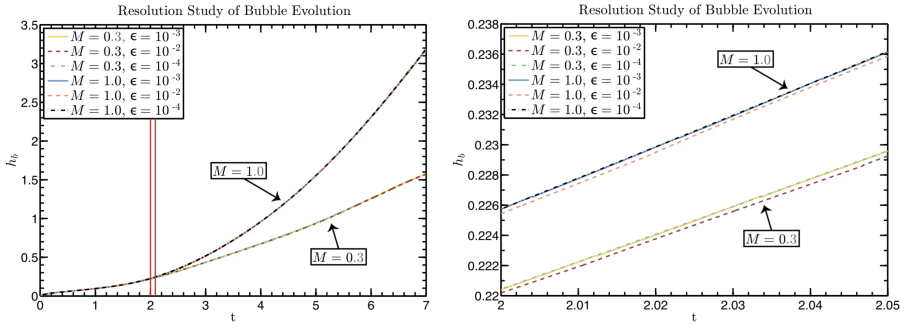

(a) Full Evolution (b) Zoomed-In View

Figure 3.4: The convergence of RTI growth with respect to the grid determined by ϵ. The Atwood number is 0.7 for all cases, and the zoomed in view focuses on the area between the two red lines. It becomes clear that convergence is reach when $\epsilon = 10^{-3}$ [52].

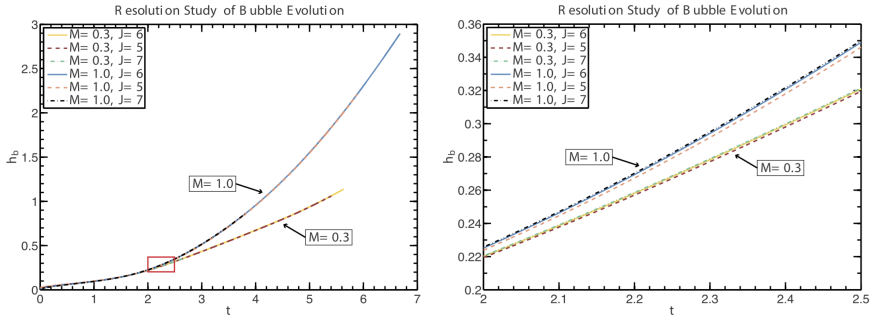

(a) Full evolution (b) Zoomed-In View

Figure 3.5: The convergence of RTI growth with respect to the grid determined by maximum j-level. The Atwood number is 0.7 and $\epsilon = 10^{-3}$ for all cases. The zoomed in portion focuses on the area highlighted by the red box. It is clear that convergence is reach when the maximum j-level allowed is 6 [52].

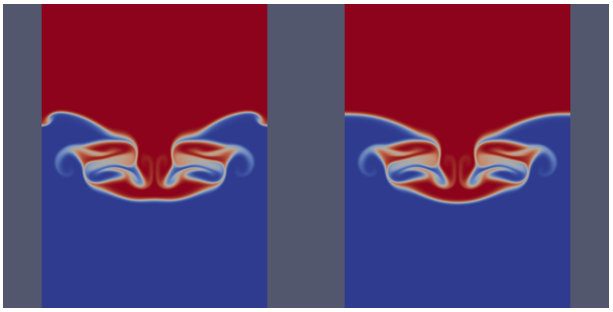

Figure 3.6: Any introduction of error in the initial conditions leads to the generation of secondary modes in the late time growth.

previously, pure single mode perturbations do not occur in actual RTI driven systems. By nature, all of these systems are inherently multi-mode. The power in simulating the single mode instability is that we can use it to determine the requirements of our code base. In the single mode system, we should remain symmetric for the entire growth regime, whereas in the multi-mode scenario, we are not guaranteed symmetry. For cheaper simulations, we do have the option of simulating only half of the single mode perturbation with mirrored boundary conditions instead of periodic, but the power in simulating the entire wavelength is that it allows us to check if any additional modes, directional biasing, or asymmetrical growth happens. This allows us to be able to determine a set of requirements so that when investigating the multi-mode regime, we can be sure that we are purely seeing the growth of the applied perturbations. As shown in 4.5, the standard convergence studies are not a rigorous enough check to ensure that secondary modes are not applied. To determine these requirements, a secondary study must be carried out.

To complete this study, all that is required is the analysis of the symmetry of the problem in the initial conditions. Essentially, if there is any asymmetry in the initial conditions, we know that this will nonlinearly propagate through time and cause issues later. The nature of RTI is that the initial conditions are on a very small scale, so anything else on that scale will also grow. We seek to minimize the difference across the line of symmetry in the initial fields of the simulations. Though all the fields are important, the most significant fields defined at the initial conditions to determine this symmetry are the species mass fraction, as it is the scalar to be advected to determine the position of the bubble and spike, and the initial velocity. This first step to doing this is to study the effect that the resolution has on the symmetry of the initial conditions. In Figure 3.7, the results are shown for calculating both the l^∞ and l^2 norms of the symmetry error. The l^2 norm is normalized by the number of points in the domain, and the points that are omitted, i.e. velocities at $j_{max} = 8$ and mass fraction at $j_{max} = 4$, are effectively zero. Essentially, we can see that the maximum error in the velocity field is at the level of machine precision, and thusly not much can be done. The error in Y, though, is significantly higher, but we can see a clear decreasing trend with the l^2 error as the resolution is increased. For this reason, and also because there is a minimum in the l^∞ error

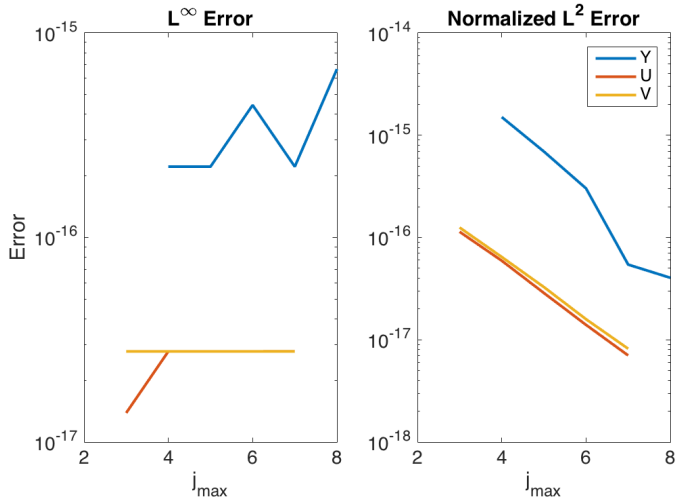

Figure 3.7: A plot of the symmetry error of Y, u and v as a function of resolution.

for $j_{max} = 7$, as well as $j_{max} = 7$ being cheaper to run than $j_{max} = 8$, we can choose this resolution as our new requirement. Continuing in this study, we must also approach the problem of whether ϵ has an effect on the initial symmetry. To do this, we run a similar study on the initial conditions, subtracting the two sides from each other to get the symmetry error while varying the value of ϵ while keeping $j_{max} = 7$. The l^∞ and l^2 error (which no longer needs to be normalized for the number of points) from this can be seen in Figure 3.8. This shows a clear trend that for u and v, there is no significant change in the symmetry as a function of ϵ, but Y becomes more symmetrical with lower ϵ. This decrease in error asymptotes in the l^2 sense near $\epsilon = 10^{-5}$. This tells us that at least for the initial conditions, the smaller the thresholding in the initial conditions, the more symmetrical our initial conditions will be. To remedy this problem, we can set our initial ϵ to be very small, i.e. 10^{-8}, and let it slowly rise to our standard running epsilon, 10^{-3}, over the first few hundred iterations. This process adds minimal cost to the simulation as a whole, and helps ensure that we maintain initial symmetry.

The final parameter we can play with in regards to maintaining symmetry in the initial conditions, is the initial interface thickness. When the initial conditions are set, the interface is set as a diffusion zone between the two species. This is done using the exact solution for the mass

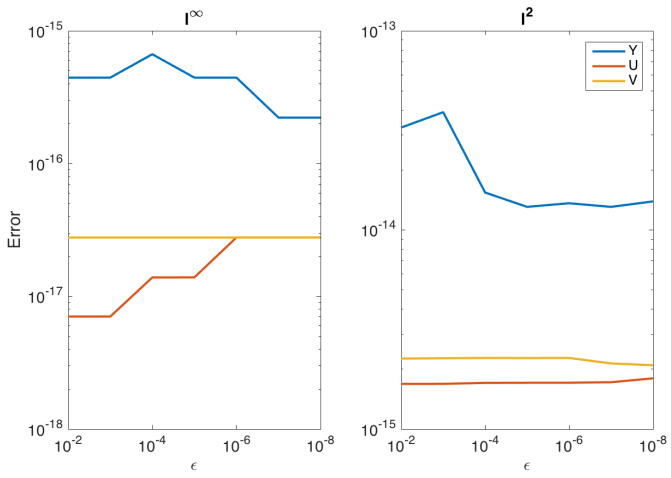

Figure 3.8: A plot of the symmetry error of Y, u and v as a function of ϵ.

diffusion equation, i.e. the error function. When setting this, though, we can choose how thick we want the initial diffusion zone to be, and by changing this we only impact the growth through a slight shifting of the initial diffusive growth phase, i.e. it has minimal impact on late time behavior. Essentially, by increasing our diffusion region at the interface, we should be able to both better represent the error function by having more points to describe it, and it should also act as an initial smoothing buffer region. In short, the thicker the initial interface, the better chance we should have at gaining smoothness. The thickness of this interface is characterized by how many points on the finest resolution we use to transition from 1% of the top fluid to 99% of the top fluid. The results for the effect on the symmetry of this parameter is shown in 3.9. Similarly to the last parameter, changing this one does not cause an increase or decrease in the number of points in the total domain, so there is no need to normalize the error. It is interesting to note that increasing the number of points across the interface actually causes an increase in the symmetry error. The goal is to maximize the number of points across the interface to act as a buffer in the initial time steps, while still maintaining the best symmetry possible. For these reasons, the two choices are either for 8 points across the interface or 16. In practicality, the difference between the two images in 4.5 is that the one without the secondary modes was initialized with 16 points across the interface while the one with the secondary modes only had 8. Based on this heuristic, the choice becomes to use 16 points across the interface.

In summary, in order to accurately capture the physics of these RTI driven flows, we will use a maximum j level of 7, an initial ϵ of 10^{-8} that is then allowed to slowly shift to our running epsilon of 10^{-3}, and we will initialize the diffusion zone using 16 points across the interface.

3.4 Adaptation Parameters

One of the benefits to using PAWCM is that it allows us to adapt on any flow field variable that we can calculate. Given this choice, though, how do know which fields are the ones that require adaptation? There are two separate approaches to this problem, and conveniently, one can feed off of the other. Firstly, we can choose which parameters we want to adapt on based on our

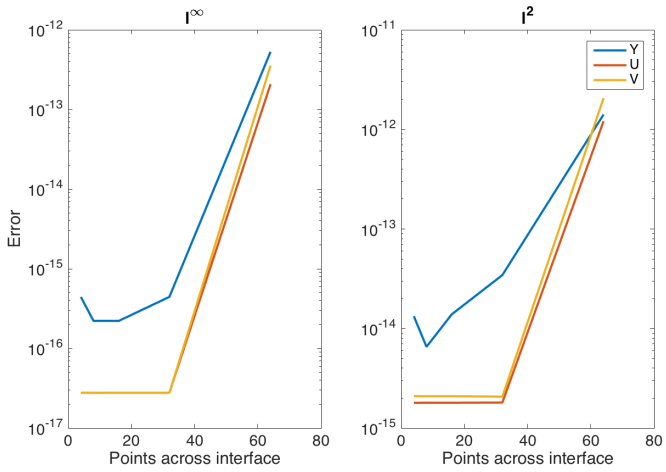

Figure 3.9: A plot of the symmetry error of Y, u and v as a function of the points across the interface. .

a priori knowledge. For example, we know that we are interested in resolving the mass fraction, there could potentially be an acoustic wave in the domain, and also that the driving force behind the development of the instability is vorticity, so our initial guess would be to adapt on the set of parameters that should best capture these features, namely $Y, ||S_{ij}||,$ and ω, respectively. We can apply this to a test simulation and see what sort of grid each variable will give us. These grid solutions can be seen in Figure 3.10 along with the mass fraction and vorticity fields for a reference. By looking at the grids, it becomes quite apparent that each parameter adapts on vastly different features of the flow. For instance, the acoustic wave towards the top of the domain would not be captured by either the adaptation from Y or ω. In all actuality to get the best grid, adaptation on all three parameters is required to ensure that the unique physics that each one exhibits is accurately captured. Alternatively, lets say that we chose that we wanted to adapt on velocity and density because our intuition tells us that the flow is driven by a density jump and by velocity fields. The resulting adapted grids and reference fields are shown below in Figure 3.11. At just a glance it becomes immediately apparent that the grids supplied by the analysis of these fields are much more sparse than what we were able to generate before, especially the grid generated by adapting on the density field. Looking back to how the adaptation works, we know that the methodology looks for steep gradients and high variability, so this means that the density field must be relatively smooth. What this posits is that there are much more complex interactions going on that are driving the instability. This breaches the realm into the second method for choosing our grid adaptation parameters. By performing an analysis on a single time step and adapting on a variety of different variables, we can determine the variables that are contributing the most to the growth and development of the instability. As long as we are resolving our fields to ensure that we aren't causing numerical oscillations, we know that the dynamics caused by a variable will cause more significant points as it affects a greater region of the flow. This means by analyzing variables, we can essentially determine the most important variables by just seeing how many grid points the adaptation generates. Now, this does not mean that low significant point generation means a flow variable is unimportant, but it does imply that the more points generated, the more important

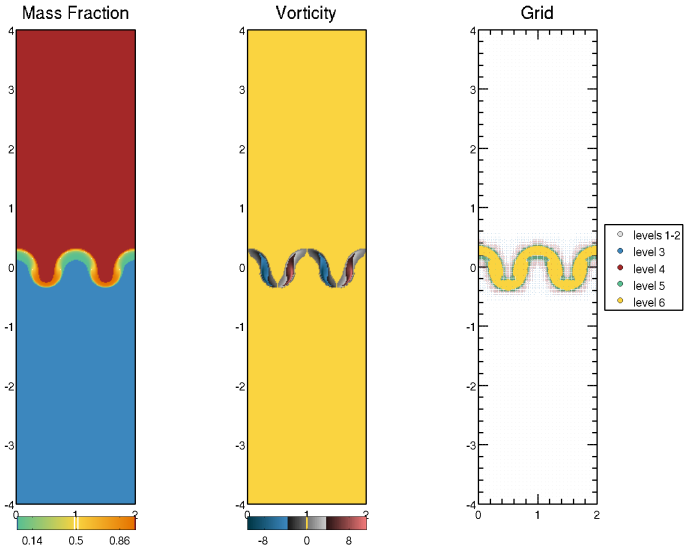

(a) Adapted by Y

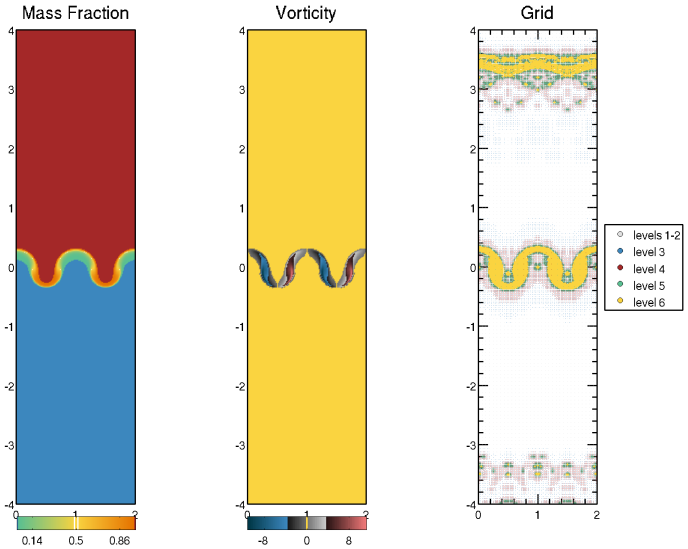

(b) Adapted by $||S_{ij}||$

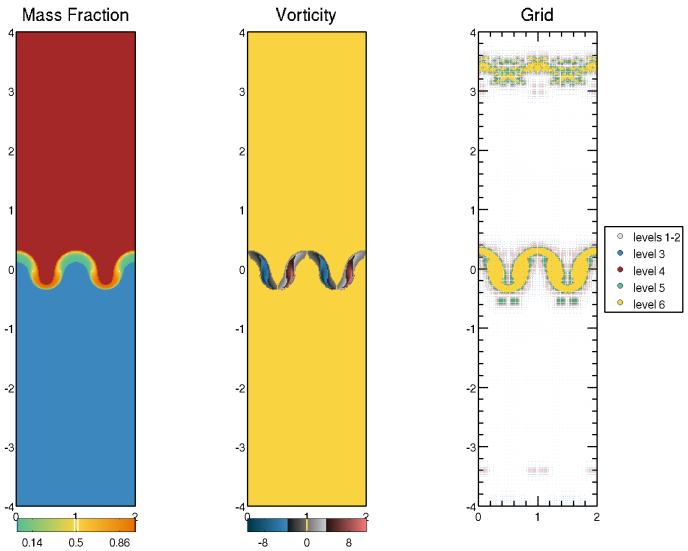

(c) Adapted by ω

Figure 3.10: Example grids based on the adaptation of a single flow field parameter.

that variable is in determining the evolution of the flow. If we look back to the five grids generated

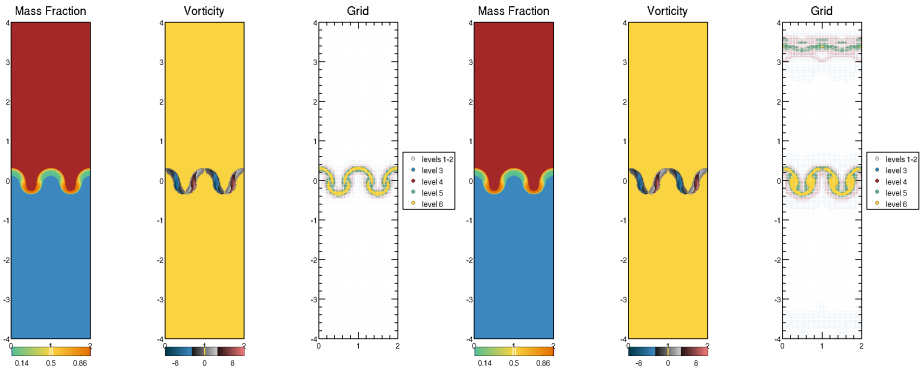

(a) Adapted by ρ (b) Adapted by u_i

Figure 3.11: Alternative grids based on different adaptation parameters.

for the test case, it becomes evident that the 2 most important variables out of the selected ones are the vorticity and norm of the strain rate tensor, $||S_{ij}||$, simply because they generate the most complex grid with the most significant points. This in itself is not an interesting discovery. We already know that strain rates are high around acoustic waves and that vorticity generation and development causes the growth of the instability. What is the interesting find is the idea that we can now analyze more complex flow fields to determine what variables are dominating the flow. In Figure 3.12, you can see a late time flow field of a RTI simulation with the mass fraction, vorticity, and corresponding grid shown. To arrive at this grid, the adaptation was done on multiple variables, namely the velocity, species, gradient of the species, the magnitude of vorticity, and the norm of the strain rate tensor. Note the complexity in the formations of both the grid and the mass fraction. It is important to notice that at this stage some asymmetry has developed, but this simulation was chosen to show that these asymmetries can be captured through the right adaptation. In Figure 3.13, you can see a comparison of the contribution that each one of these variables has on the grid.

Looking at these individual grids, it is clear that vorticity and the gradient of the species mass fraction seem to be contributing the most points at the highest resolution levels with the norm of

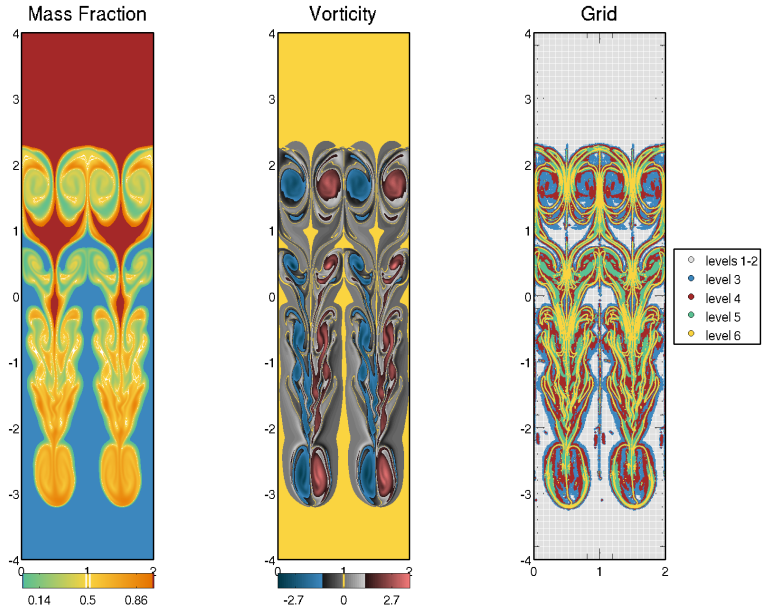

Figure 3.12: A late time RTI driven flow with its corresponding grid.

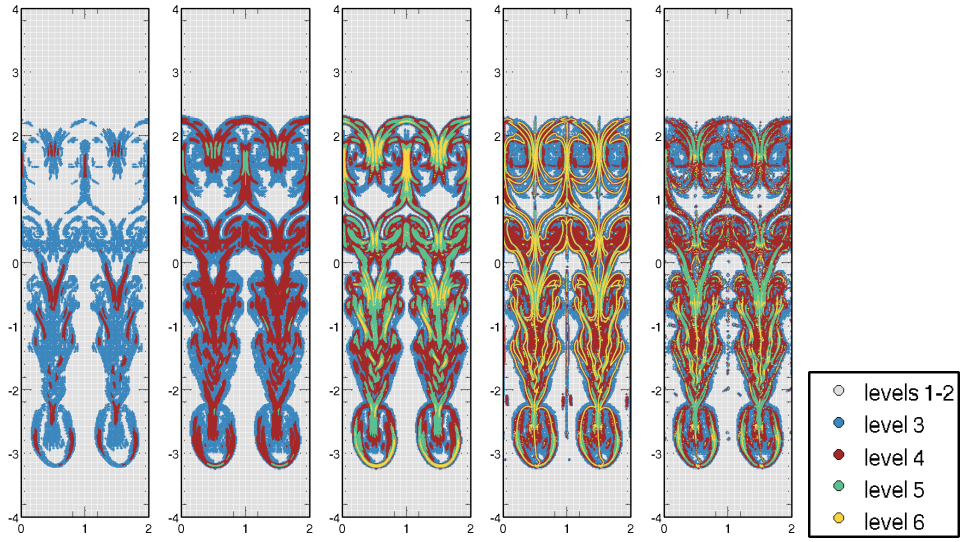

(a) u_i (b) Y (c) $\frac{\partial Y}{\partial x_1}$ (d) $|\omega|$ (e) $||S_{ij}||$ (f) Legend

Figure 3.13: The individual contribution of the adaptation of each variable.

the stress tensor not being far behind. The adaptation that is accomplished from the velocity and mass fraction fields is negligible in comparison. From here, though, we can begin exploring even more derived variables, below in Figure 3.14, you will find what happens if the grid is allowed to adapt on the baroclinic term from the vorticity equation or the divergence of the velocity field. The end results are quite clear, namely that the baroclinic term causes a large amount more adaptation on the finest grid resolution than any of the other flow variables. The divergence of velocity also has a large number of points, larger than the velocity or species fields, but not nearly as many as the baroclinic term. In Table 3.2, you can find a summary of the number of points that are active after the adaptation on that variable takes place. Looking at these counts, it becomes readily apparent that the baroclinic term causes more adaptation than any other term. This result tells us that the baroclinic term in the vorticity equation must be a dominant feature in the flow.

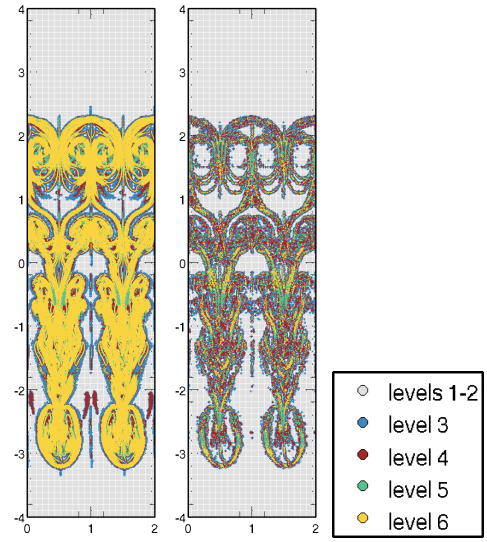

(a) $\frac{1}{\rho^2}\nabla\rho \times \nabla p$ (b) $\nabla \cdot u_i$ (c) Legend

Figure 3.14: The individual contribution of the adaptation of each variable.

Variable	Active Points
u_i	401349
Y	785760
$\frac{\partial Y}{\partial x_1}$	2373332
$\|\omega\|$	2754066
$\|\|S_{ij}\|\|$	1700967
All variables above	3933336
$\frac{1}{\rho^2}\nabla\rho \times \nabla p$	8225174
$\nabla \cdot u_i$	1219567
P	262272
ρu_i	400592
e	262272
ρ	262598
ω	1148117
ρY	426794
All variables presented	9344958

Table 3.2: A summary of the number of active grid points when adapting on various variables.

3.5 Other Applications of PAWCM: Data Assimilation

This wavelet method has been shown to be useful in many other scenarios. In addition to the RTI problem, it has been applied to many other case including shock particle interactions,

channel flow, and flow around cylinders just to name a few. In addition to performing effectively at DNS simulations, it has been shown to be a useful tool for running Large Eddy Simulations and other models. It can capture reactions, work on ocean flows, and capture shocks, all while being efficient and effective at maintaining its grid adaptation [60, 18, 14, 32, 55]. In addition to these problems, the Adaptive Wavelet Collocation Method has been adapted to work on space and time simultaneously in a data assimilation problem. Using this method, we are able to adapt on a grid as we did before, but by treating time as another dimension, we are able to adapt our time step by the intermittency of the problem [58].

The idea behind the Space Time Adaptive Wavelet Collocation method for the 4D-Var problem is as follows.The 4D-Var problem consists of a system described by some model with a set of unknown inputs such as physical parameters, boundary conditions, or initial conditions. In addition to this model, there is a collection of observations of the system state, and the goal is to estimate what the unknown inputs are. To determine the unknowns, the problem is approached as a least squares problem and solved using any number of non-linear optimization problems. To do this, a cost function is defined based on the weighted norm of the difference between the solution from the direct problem and the known observations along with a term to measure the change of the initial state from the previous estimate. The difficulty in this arises when the optimization algorithms require the gradient of this cost function. To do this, an approximation can be found using the adjoint problem and essentially solving the system using backwards time stepping. Finding the solution to the adjoint problem, though, requires access to the entirety of the solution form the forward problem. This is problematic because either large amounts of extra data must be stored, or a large amount of extraneous computations must be completed. Using the Space Time Adaptive Wavelet Collocation Method (STAWCM) allows for the solution to be well approximated using a compressed mesh that adapts on the intermittent structures of the problem [45, 29, 1, 49, 27, 40, 3].

In general the space-time formulation of the 4D-Var problem takes the form

$$\begin{cases} \bar{\mathbf{F}}\left(\mathbf{u}(\mathbf{x})\right) = 0 \quad \mathbf{x} \in \Omega, \\ \mathbf{u}(\mathbf{x}|x_{d+1} = 0) = \mathbf{c}, \end{cases} \tag{3.22}$$

where $\bar{\mathbf{F}}\left(\mathbf{u}(\mathbf{x})\right) = \dfrac{\partial \mathbf{u}}{\partial t}(\mathbf{x}, t) - \mathbf{F}\left(\mathbf{u}(\mathbf{x}, t)\right)$, where $\mathbf{F} : \mathbb{R}^n \to \mathbb{R}^n$ is a vector valued function such that $\mathbf{F} = (F_1, F_2, \ldots, F_n)^{\mathrm{T}}$ with $F_i = F_i(\mathbf{u})$ for $1 \leq i \leq n$, and $\{\mathbf{x} \in \Omega | x_{d+1} = 0\}$ is the boundary of the space-time domain with $x_{d+1} = 0$. Also, the space time variable is defined as $\mathbf{x} = (x_1, x_2, \ldots, x_{d+1})^{\mathrm{T}}$ where d is the dimensionality of the physical space domain. Essentially this means that we have d spacial directions and an extra dimension due to space.Thusly the second equation of Eq. (3.22) is the equivalent to the initial condition in the conventional formulation of the problem.

From this, we write out our cost function where we use the norms that are based on the appropriate inner products and then derive the adjoint model of the equation. First we write out the observations $\mathbf{y}^{\mathrm{o}}$ in terms of the space-time variable

$$\begin{aligned} \mathbf{y}^{\mathrm{o}} : \Omega &\to \mathbb{R}^m \\ \mathbf{x} &\mapsto \mathbf{y}^{\mathrm{o}}(\mathbf{x}) = \mathbf{h}\left(\mathbf{u}(\mathbf{x})\right) + \boldsymbol{\varepsilon}^{\mathrm{o}}(\mathbf{x}). \end{aligned} \tag{3.23}$$

Then, we can write the cost function as:

$$J(\mathbf{c}) = \frac{1}{2}\|\mathbf{h}\left(\mathbf{u}\right) - \mathbf{y}^{\mathrm{o}}\|^2_{\mathcal{O}} + \frac{1}{2}\|\mathbf{c} - \mathbf{c}^{\mathrm{b}}\|^2_{\mathcal{B}} \tag{3.24}$$

where

$$\|\mathbf{h}\left(\mathbf{u}\right) - \mathbf{y}^{\mathrm{o}}\|_{\mathcal{O}} = \int_0^T \|\mathbf{h}\left(\mathbf{u}(\mathbf{x})\right) - \mathbf{y}^{\mathrm{o}}(\mathbf{x})\|^2_{\mathcal{O}} dx_{d+1} \tag{3.25}$$

Which allows us to write out the adjoint model as:

$$\begin{cases} \bar{\mathbf{F}}^*\left(\mathbf{p}(\mathbf{x})\right) = \left[\dfrac{\partial \mathbf{h}}{\partial \mathbf{u}}\right]^* \cdot \left[\mathbf{h}(\mathbf{u}(\mathbf{x})) - \mathbf{y}^{\mathrm{o}}(\mathbf{x})\right], \quad \mathbf{x} \in \Omega, \\ \mathbf{p}(\mathbf{x}|_{x_{d+1}=T}) = 0, \end{cases} \tag{3.26}$$

where

$$\bar{\mathbf{F}}^*\left(\mathbf{p}(\mathbf{x})\right) = \frac{\partial \mathbf{p}}{\partial x_{d+1}}(\mathbf{x}) + \left[\frac{\partial \mathbf{F}}{\partial \mathbf{u}}\left(\mathbf{u}(\mathbf{x})\right)\right]^* \cdot \mathbf{p}(\mathbf{x}) \tag{3.27}$$

Finally, we are able to discretize these equations for use with our numerical techniques. This is done in a way that makes its convenient to apply STAWCM. As the solutions are obtained, STAWCM

works by going through the same grid refinement techniques as described previously, except that now, an additional dimension is added to adapt on. So, if we are solving a two dimensional problem, STAWCM will treat it as a three dimensional problem but with time added. It then uses the adaptive techniques as it would with any other dimension.

To test out this method, two test problems were used. First a linear problem was studied, and then a non-linear problem, both of which tested as one dimensional in space and one dimensional in time. The linear problem is described with the space-time domain Ω being $\Omega = \Omega_s \times [0, T]$, where $\Omega_{\mathrm{s}} = [-1, 1]$ and $[0, T]$ are the physical space and the time domains, respectively. A linear advection-diffusion problem is considered:

$$\begin{cases} \dfrac{\partial u}{\partial x_{d+1}} + v_d \dfrac{\partial u}{\partial x_d} - \nu \dfrac{\partial^2 u}{\partial x_d^2} &= 0, \\ u|_{x_{d+1}=0} &= c(x_d), \\ u|_{x_d=-1} = u|_{x_d=+1} &= 0, \end{cases} \tag{3.28}$$

where u is the scalar system state, $c(x_d)$ is a function that defines the initial condition, and $v_d(\mathbf{x})$ is the advection velocity. The subscripts d and $d+1$ are used to denote spatial and time coordinates, respectively. The associated adjoint model is given by:

$$\begin{cases} \dfrac{\partial p}{\partial x_{d+1}} + \dfrac{\partial (v_d p)}{\partial x_d} + \nu \dfrac{\partial^2 p}{\partial x_d^2} &= \left[\dfrac{\partial \mathbf{h}}{\partial \mathbf{u}}\right]^* \left(h(u) - y^{\mathrm{o}}\right), \quad \mathbf{x} \in \Omega, \\ p|_{x_{d+1}=T} &= 0, \\ p|_{x_d=-1} = p|_{x_d=+1} &= 0, \end{cases} \tag{3.29}$$

where p is the adjoint variable. To achieve the observations, a base mesh at j-level j_{obs} is forced to always be present and the observations are taken from a known control variable c^t which in this case is defined as

$$c^t(x_d) = \exp\left(-\frac{x_d^2}{2\sigma^2}\right) \text{ with } \sigma = 0.1. \tag{3.30}$$

Lastly, the time domain is taken such that $T = 2$ ad the advection velocity is described by

$$v(x_d, x_{d+1}) = 0.5 \sin(2\pi x_{d+1}). \tag{3.31}$$

From here we are able to solve the problem using STAWCM and the MODULOPT library's M1QN3 algorithm [24]. An example result for the solution obtained from the analysis of the data assimilation

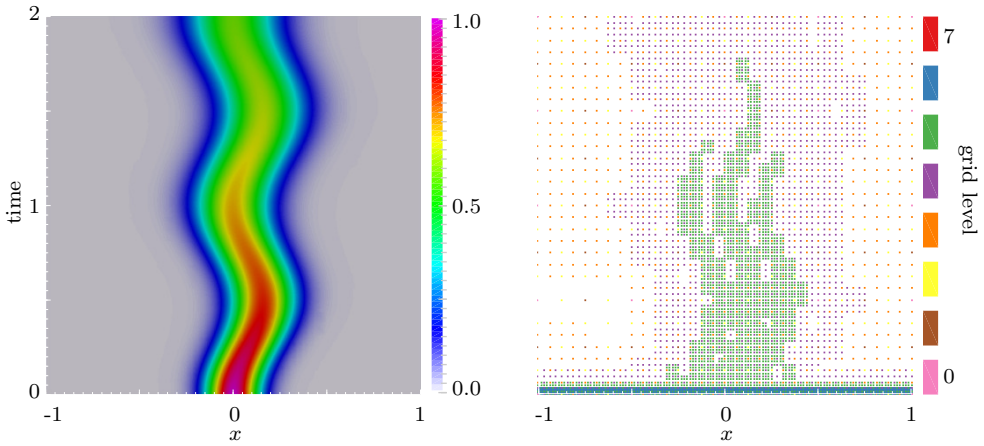

Figure 3.15: Analysis: the solution(left) and the corresponding grid (right) with the **analyzed** control variable, $j_{\max} = 6$, and $\epsilon = 10^{-3}$.

problem is shown in 3.15. The evolution of the cost function and its gradient during the optimization of this process are shown in 3.16. For this particular run, $j_max = 6$ and $\epsilon = 10^{-3}$, and we can see from the evolution of the cost function and its gradient that the solution is converged. It was found by varying the order of ϵ, that the data assimilation results remained congruent with that of what we expected, i.e. ϵ determined the level of error present in the solution. This analysis was also carried out for a nonlinear test problem where the advection velocity was changed from ν_d to be $\nu_d + u$ and the adjoint model changed accordingly. The results from this can be seen in 3.17. This paints a clear picture that even for non-linear problems, the data assimilation can reach a reasonable approximation of the true solution and it converge as ϵ gets smaller.

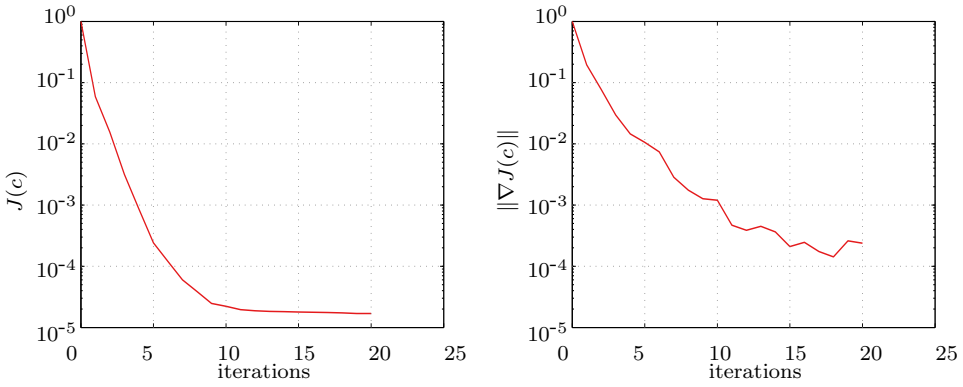

Figure 3.16: Evolution of the cost function and its gradient during optimization.

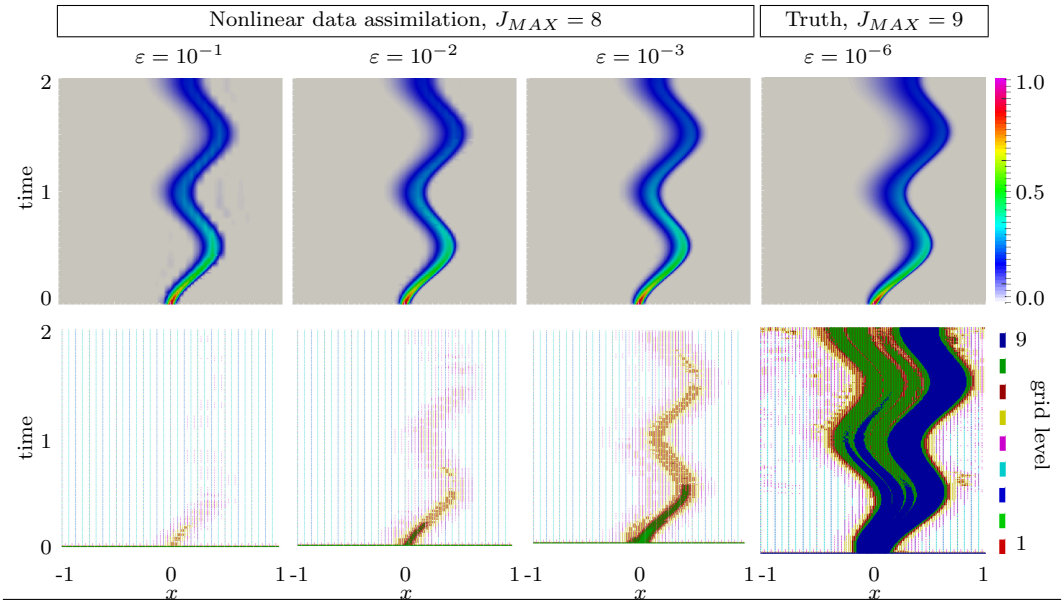

Figure 3.17: The analyzed solution of nonlinear 4D-Var (top row) and the corresponding computational grid (bottom) for different values of the threshold parameter. The column 4 is the true solution with $\epsilon = 10^{-6}$.

Chapter 4

Effects of Isothermal Stratification Strength on the Single Mode Compressible Rayleigh-Taylor Instability

4.1 Abstract

The effects of isothermal stratification on the single mode compressible two-dimensional (2D) Rayleigh-Taylor instability (RTI) is examined using fully compressible wavelet-based direct numerical simulations (DNS). The simulations model low Atwood number (At = 0.04) RTI development for four different strengths of initial stratification, corresponding to isothermal Mach numbers from 0.3 (weakly stratified) to 1.2 (strongly stratified). Simulations are also performed for three different Reynolds numbers, spanning 5,000 to 20,000, for the two cases with weakest and strongest stratification. All simulations use adaptive wavelet-based mesh refinement to achieve very fine spatial resolution at relatively low computational cost. The simulations show that weak initial stratification in the nearly incompressible regime leads to pronounced bubble and spike asymmetries, while bubble and spike growth rates become increasingly similar as the stratification strength increases. For small initial stratifications, the bubble and spike growth rates undergo oscillatory behavior whereby slow-downs and re-accelerations are alternately observed until the growth halts even for the weakest stratification. Above an isothermal Mach number of roughly 0.6, this behavior is less pronounced and nearly uniform suppression is observed. Reynolds number is found to have little effect on bubble and spike growth, although the formation of secondary vortices becomes substantially more pronounced as Reynolds number increases. A simultaneous study of vortex pair evolution shows that, at low Atwood numbers, bubble and spike growth rates for the strongly

stratified cases are nearly identical to vortex propagation rates, but there is a substantial mismatch in vortex pair and RTI growth rates for weak stratification when the RTI is able to continue growing and re-acceleration occurs. Finally, a three-dimensional (3D) simulation of compressible RTI in the strongly stratified case (corresponding to a Mach number of 1.2) is performed in order to demonstrate that the present 2D results for single mode RTI are qualitatively consistent with 3D results.

4.2 Introduction

The Rayleigh-Taylor instability (RTI) is formed when a mean density gradient is oriented in a direction opposite to that of an accelerative force [50, 59]. Such a scenario arises in a number of engineering and physics problems, including Inertial Confinement Fusion (ICF) [7], supernovae ignition fronts [31, 28, 8], and x-ray bursts [39], to name just a few examples. Understanding RTI growth and behavior in these systems is made challenging, however, by the low Atwood and high Reynolds numbers present in many real-world problems, resulting in dynamics driven by relatively small density differences over a wide range of length and time scales. The present study is focused on understanding the long-time evolution of RTI as a function of stratification strength (i.e., Mach number) and Reynolds number at low Atwood number for isothermal stratifications using fully compressible wavelet-based direct numerical simulations (DNS).

The use of DNS for the study of RTI is motivated by the difficulty in controlling, with high precision, initial and boundary conditions in experiments. This difficulty has resulted in ambiguity surrounding many experimental observations, for example the unexpectedly high RTI growth rates measured in prior experiments, which are now understood to be the result of low wavenumber perturbations. By contrast, all initial and boundary conditions are known and carefully controlled in DNS, and DNS has become an increasingly common tool for the study of RTI over the past five years [64].

Despite its promise, DNS is not without its challenges. In particular, the computational cost required to resolve all length and time scales at high Reynolds and low Mach numbers using three-

dimensional (3D) fully compressible simulations is enormous. Ultimately, resolution requirements are determined by the sharpness of the interface between the two fluid species, and the generation of shockwaves from both acoustics and the RTI itself. The nature of RTI growth also requires domains that are much longer than the initial perturbation in order to capture the entirety of the growth, prevent unphysical boundary interactions, and to give enough space to dissipate any shockwaves generated. As a result of these resolution and domain size requirements, most RTI simulations have been performed in only 2D, at low Reynolds numbers, and from an incompressible standpoint [43, 42] by assuming that the velocity flow-field remains divergence free (i.e., by solving the Boussinesq or anelastic equations).

In the present paper, these simplifying assumptions are relaxed through the use of a new fully compressible DNS capability [51, 52] that employs adaptive mesh refinement based on the Parallel Adaptive Wavelet Collocation Method (PAWCM). This method allows high spatial resolution to be used where it is needed (e.g., where density and velocity gradients are large), while reducing the total number of collocation points used in the simulation. The development of the adaptive wavelet DNS capability was described by Reckinger *et al.* [52], where a preliminary study was performed of 2D RTI growth as a function of stratification strength at moderately high Atwood and low Reynolds numbers.

Using this adaptive capability, DNS are performed here at low Atwood number for different Reynolds numbers and different strengths of isothermal initial stratification, corresponding to Mach numbers between 0.3 (weak stratification) and 1.2 (strong stratification) [43, 42, 23]. The focus on low Atwood number, in particular, is motivated by the observations of RTI growth and regimes in Wei and Livescu [64], where an asymptotic variable-density form of the Navier-Stokes equations were solved in 2D to show that RTI is suppressed at high Mach numbers. The goals of the present study are to reproduce these features by solving the fully compressible Navier-Stokes equations in both 2D and 3D, and to determine the dependence of these features on Reynolds number and stratification strength. Here single-mode initial perturbations are studied in order intended to simplify the problem by eliminating complex interactions of multiple wavelengths, thereby allowing the un-

derlying fundamental physics to be more easily understood. Although the isothermal stratification creates variations in density and pressure, the thermodynamics are assumed to be in equilibrium.

The overall simplicity of this physical configuration is intended to reveal compressibility effects as clearly as possible, without additional confounding effects due to other factors. Even in the incompressible case, RTI have been examined over an enormously wide parameter space; just a few examples include studies of incompressible RTI for different density variations [**?**], temperature fields [**?**], electromagnetic fields [**?**], viscosities [**?**], surface tensions [**?**], miscibilities [**?**], thermal transfers [**?**], and boundary effects [**?**]. Compressibility adds yet another set of parameters to consider, including temperature-dependent transport (e.g., viscosity, diffusivity) and thermodynamic (e.g., specific heat ratio) coefficients [20, 36]. Although each of these parameters must be varied in succession in order to fully understand the complex nature of compressible RTI in problems such as ICF, we specifically focus here on the effects of isothermal stratifications of various strengths, an obvious starting point for the study of compressible RTI.

In order to explain the observed results, RTI growth at low Atwood and high Reynolds numbers is compared with vortex dynamics for different stratification strengths. This additional analysis and comparison is motivated by the observation that RTI growth is heavily dominated by the vorticity transport that is generated[64]. Most of the various parameters that effect the instability growth truly manifest themselves by affecting the vortical fields. RTI will begin by first generating a vortex pair in the two dimensional case or a vortex ring in the three dimensional. These vortical formations will then lead to induced velocities and the generation of additional vorticity by the creation of shear layer instabilities such as the Kelvin-Helmholtz instability. For these reasons, insight into the physics of the RTI scenario can be garnered by studying the effects of various parameters on the induced velocities of vortex pairs and rings which can be done for significantly cheaper than full RTI simulations. These pairs and rings match the initial vortical fields generated by the RTI and give an interesting insight into the effects of the background on the initial growth.

The rest of this paper is organized as follows. The second Section discusses the problem setup

including the governing equations and initialization for both the RTI and vortex cases. Section 3 provides a brief discussion of the numerical method applied to complete these simulations. In Section 4, the paper goes in depth into the results of this study, first looking at the effects of Reynolds number and background stratification strength on RTI growth, and then repeating this for the vortex simulations. This is then all confirmed in three dimensions. Finally, the resulting conclusions are presented in Section 5.

4.3 Problem Description

4.3.1 Governing Equations

The numerical simulations solve the fully compressible, two-fluid Navier-Stokes equations given by [43, 68]

$$\frac{\partial \rho}{\partial t} + \frac{\partial (\rho u_j)}{\partial x_j} = 0\,, \tag{4.1}$$

$$\frac{\partial (\rho u_i)}{\partial t} + \frac{\partial (\rho u_i u_j)}{\partial x_j} = -\frac{\partial p}{\partial x_i} + \rho g_i + \frac{\partial \tau_{ij}}{\partial x_j}\,, \tag{4.2}$$

$$\frac{\partial (\rho e)}{\partial t} + \frac{\partial (\rho e u_j)}{\partial x_j} = -\frac{\partial (p u_i)}{\partial x_i} + \rho u_i g_i + \frac{\partial (\tau_{ij} u_i)}{\partial x_j} - \frac{\partial q_j}{\partial x_j} + \frac{\partial [T (c_\mathrm{p})_l s_{jl}]}{\partial x_j}\,, \tag{4.3}$$

$$\frac{\partial (\rho Y_i)}{\partial t} + \frac{\partial (\rho Y_i u_j)}{\partial x_j} = \frac{\partial s_{ji}}{\partial x_j}\,, \tag{4.4}$$

where ρ is the density, u_i is the velocity in the x_i direction, p is the pressure, g_i is the gravitational acceleration, τ_{ij} is the viscous stress tensor, e is the specific total energy, q_i is the heat flux, T is the temperature, $(c_\mathrm{p})_i$ is the specific heat capacity for fluid i, s_{ij} is the mas flux for fluid j, and Y_i is the mass fraction for the i^{th} fluid. Note that, for a two-fluid system, $Y_2 = 1 - Y_1$, and so Eq. (6.4) need only be solved for $i = 1$. The ideal gas law $p = \rho R T$ is enforced by expressing the specific total energy as

$$e = \frac{1}{2} u_i u_i + c_\mathrm{p} T - \frac{p}{\rho}\,, \tag{4.5}$$

where R is the combined gas constant defined in terms of the universal gas constant $\mathcal{R}$ and the molar mass of each fluid, W_i, as

$$R = Y_i R_i = \mathcal{R} \frac{Y_i}{W_i}\,, \tag{4.6}$$

where we define the species gas constant as $R_i \equiv \mathcal{R}/W_i$. The combined specific heat capacity c_p appearing in Eq. (6.5) is similarly defined as

$$c_\mathrm{p} = (c_\mathrm{p})_i Y_i \,. \tag{4.7}$$

The viscous stress τ_{ij} in Eqs. (6.2) and (6.3) is assumed to be Newtonian and is given by

$$\tau_{ij} = \mu \left(\frac{\partial u_i}{\partial x_j} + \frac{\partial u_j}{\partial x_i} - \frac{2}{3} \frac{\partial u_k}{\partial x_k} \delta_{ij} \right) , \tag{4.8}$$

where the dynamic viscosity is given by $\mu = \rho\nu$, with the kinematic viscosity ν assumed to be constant (i.e., temperature independent). The heat flux in Eq. (6.3) is written as

$$q_j = -k \frac{\partial T}{\partial x_j} \,, \tag{4.9}$$

where k is the thermal conductivity, and the species mass flux in Eqs. (6.3) and (6.4) is defined as

$$s_{jl} = \rho D \frac{\partial Y_l}{\partial x_j} \,, \tag{4.10}$$

where D is the mass diffusivity. Both k and D, like the kinematic viscosity ν are assumed to be constant and temperature independent, and both Prandtl and Schmidt numbers are unity.

In the present study, the system of equations given by Eqs. (6.1)-(6.8) is solved using the PAWCM numerical approach, which is described in Section 4.4, for an RTI with a physical setup as described in the following section. For this study, the majority of fluid properties are taken to be the same between the two fluids for simplicity. This includes the dynamic viscosity, μ, the heat conduction coefficient, and k, and the mass diffusion coefficient, D.

4.3.2 Initialization of Rayleigh Taylor Instability

Rayleigh Taylor instability occurs when a heavier fluid, denoted by index '2' with molar mass W_2, is suspended above a lighter fluid, denoted by index '1' with molar mass W_1, in the presence of an accelerative force such as gravity. The addition of a perturbation causes the pseudo-stable condition to be lost, and the heavier fluid begins to fall into the lighter fluid in a spike-like formation, while the lighter fluid rises into the heavier fluid in a bubble-like formation. Assuming that it is small

enough, the initial perturbation grows in accordance with linear perturbation theory, but quickly becomes more complex as Kelvin-Helmholtz instabilities cause continuous production of vorticity along the sides of the bubbles and spikes [50, 59] via the baroclinic torque (vorticity dynamics is discussed in more detail in the next section). This production of vorticity creates a nonlinear system that cannot be described by simplified models [43]. In the classical incompressible case, where the density of both fluids is constant, this growth eventually leads to a re-acceleration of the bubble and spike tips, finally resulting in chaotic dynamics and development. In the compressible case, however, it is impossible to have constant densities without changing the pressure and temperature fields. The effects of changing any of these fields is largely unknown, and here we choose to impose an isothermal background state in order to eliminate thermal effects since the background state is already in thermal equilibrium. Future work will examine the effects of isopycnic and isentropic background states.

The present RTI problem is initialized by imposing a perturbation in the presence of a gravitational acceleration on a background state that is in hydrostatic equilibrium. The resulting pressure, $p(x_1, x_2, t)$, and density, $\rho(x_1, x_2, t)$, fields at $t = 0$ can be expressed for 2D RTI (i.e., as functions of x_1 and x_2) as

$$p(x_1, x_2, 0) = p_0(x_1) + p'(x_1, x_2, 0)\,, \tag{4.11}$$

$$\rho(x_1, x_2, 0) = \rho_0(x_1) + \rho'(x_1, x_2, 0)\,, \tag{4.12}$$

where p_0 and ρ_0 are hydrostatic background states assuming that the gravitational acceleration is only in the negative x_1 direction (i.e., $g_i = -g\delta_{i1}$), and p' and ρ' represent fluctuations on the background state; the initial perturbations to the background state are denoted $p'(x_1, x_2, 0)$ and $\rho'(x_1, x_2, 0)$.

Assuming an isothermal background state at temperature T_0, the background pressure and density fields for fluid α (where $\alpha = [1, 2]$ and summation over Greek indices is not implied) are

given by

$$p_{0\alpha}(x_1) = p_I \exp\left(-\frac{g x_1}{R_\alpha T_0}\right), \tag{4.13}$$

$$\rho_{0\alpha}(x_1) = \frac{p_I}{R_\alpha T_0} \exp\left(-\frac{g x_1}{R_\alpha T_0}\right), \tag{4.14}$$

where the initial interface between the two fluids lies at $x_1 = 0$, with the $\alpha = 2$ fluid for $x_1 > 0$ and the $\alpha = 1$ fluid for $x_1 < 0$, p_I is the interfacial pressure, g is the magnitude of the gravitational acceleration, and $R_\alpha = \mathcal{R}/W_\alpha$ is the gas constant based on the molar mass of fluid α. A corresponding interfacial density is given using the ideal gas law as $\rho_I = p_I/(R_I T_0)$ where $R_I = \mathcal{R}[(W_1+W_2)/2]^{-1}$.

In each of the cases examined here, the kinematic viscosity ν, which is constant and the same in both fluids, is set using the perturbation Reynolds number, Re_p, as

$$Re_p \equiv \sqrt{\frac{Ag\lambda^3}{(1+A)\nu^2}} \quad \Rightarrow \quad \nu = \sqrt{\frac{Ag\lambda^3}{(1+A)Re_p^2}}, \tag{4.15}$$

where λ is the wavelength of the applied perturbation and A is the non-dimensional Atwood number defined as

$$A \equiv \frac{W_2 - W_1}{W_2 + W_1}. \tag{4.16}$$

Note that in the present study, $W_2 > W_1$ in order to generate RTI, with the heavier fluid ($\alpha = 2$) initially completely above the interface (i.e., $x_1 > 0$) and the lighter fluid ($\alpha = 1$) initially completely below the interface (i.e., $x_1 < 0$).

The degree of compressibility enters the RTI problem by re-expressing $g x_1/(R_\alpha T_0)$ in Eqs. (6.9) and (6.10) in terms of the Mach number M. There are multiple parameters that can be used to specify the degree of compressibility [42, 43], but, due to the isothermal initial state, the relevant incompressible limit is found by increasing the background pressure to cause an increase in the speed of sound such as to leave the density unaffected. This results in the definition of an isothermal Mach number based on the ratio of the gravity wave speed, $\sqrt{g\lambda}$, and the isothermal speed of sound, $a_0 = \sqrt{P_I/\rho_I}$. The resulting Mach number, M, is then given by

$$M = \sqrt{\frac{\rho_I g\lambda}{p_I}} \quad \Rightarrow \quad M^2 = \frac{g\lambda}{R_I T_0}. \tag{4.17}$$

Normalizing $P_{0\alpha}$ in Eq. (6.9) and $\rho_{0\alpha}$ in Eq. (6.10) by p_I and ρ_I, respectively, we obtain

$$p^*_{0\alpha}(x^*_1) = \exp\left(-M^2 \frac{R_I}{R_\alpha} x^*_1\right) , \tag{4.18}$$

$$\rho^*_{0\alpha}(x^*_1) = \frac{R_I}{R_\alpha} \exp\left(-M^2 \frac{R_I}{R_\alpha} x^*_1\right) , \tag{4.19}$$

where $x^*_1 \equiv x_1/\lambda$ is a normalized distance variable. It can be shown that the ratio R_I/R_α can be written in terms of the Atwood number A as

$$\frac{R_I}{R_\alpha} = \frac{2W_\alpha}{W_1 + W_2} = 1 + (-1)^\alpha A \text{ for } \alpha = 1, 2\,. \tag{4.20}$$

Since $\alpha = 1$ corresponds to the lighter fluid for which $x^*_1 < 0$ initially and $\alpha = 2$ corresponds to the heavier fluid for which $x^*_1 > 0$, the non-dimensional background states P^*_0 and ρ^*_0 can be written in final form as

$$p^*_0(x^*_1) = \exp\left[-M^2(1 \mp A)x^*_1\right] , \tag{4.21}$$

$$\rho^*_0(x^*_1) = (1 \mp A) \exp\left[-M^2(1 \mp A)x^*_1\right] , \tag{4.22}$$

The resulting initial background stratifications are shown for a variety of Mach numbers in Figure 6.1, where the size of the density difference at $x^*_1 = 0$ is determined by the value of A.

For this study, we have constrained ourselves to single mode perturbations. Though, they are not a perfect representation of the multi-mode nature of the engineering problems found in ICF and such, the effects that are being studied must be understood in the simplest cases, before they can be expanded to the complex. Through the single mode studies, we are able to determine our resolution requirements and guide our path to study the more complex multi-mode scenario while still garnering useful insights into the physics arising from compressibility. To simulate the single mode case, at this point we apply a single mode velocity perturbation to the interface in a way that is consistent with linear stability theory[52].

Even in multi-modal simulations, the most unstable mode will grow the fastest, so single mode perturbations serve as a limiting case in which the most unstable mode is the only mode applied. In addition, single-mode simulations allow the opportunity to ensure that the simulations

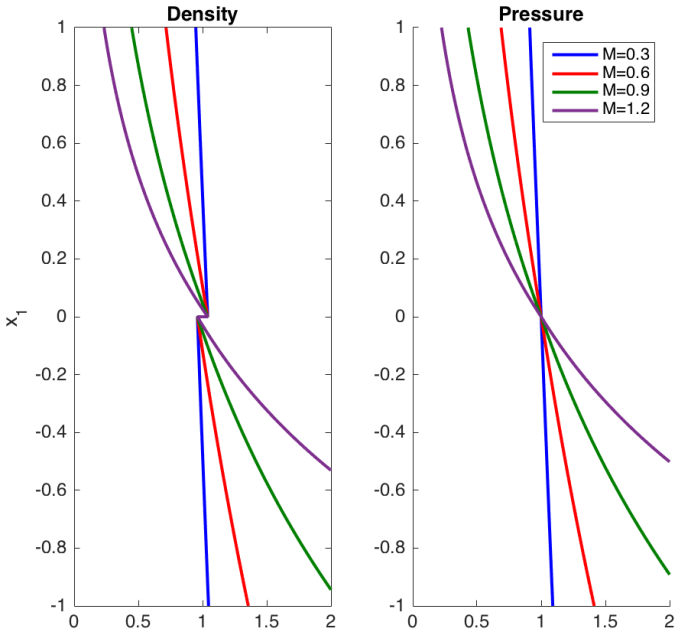

Figure 4.1: Density and pressure stratifications for $M = 0.3to1.2$ and $A = 0.04$.

are completely resolved from the initial conditions through the late times while also giving the ability to check the simulations for the addition of extra perturbation modes and the maintaining of symmetry throughout the simulation. Only through the complete investigation of single mode studies, can a simulation platform be said to accurately, reliably, and certainly capture the exact initial conditions that were input since it is the most sensitive case to errors in the late time growth and will manifest any additional modes or asymmetries introduced through the platform itself.

4.3.3 Vorticity Dynamics

By taking the curl of the momentum equation, we obtain the transport equation for the vorticity, $\omega_i = \epsilon_{ijk}\partial u_k/\partial x_j$ in a general compressible flow as

$$\frac{\partial \omega_i}{\partial t} + u_j \frac{\partial \omega_i}{\partial x_j} = \omega_j S_{ij} - \omega_i S_{kk} + \frac{\epsilon_{ijk}}{\rho^2}\frac{\partial \rho}{\partial x_j}\frac{\partial p}{\partial x_k} + D_i \,, \tag{4.23}$$

where ϵ_{ijk} is the Levi-Civita, or alternating, tensor. The first term on the right-hand side of Eq. (4.23) represents vortex stretching, the second term represents dilatation, the third term is the

baroclinic torque, and the last term is diffusion. Using the characteristic time scale $\sqrt{\lambda/g}$, the transport equation for ω can be written in non-dimensional form as

$$\frac{D\omega_i^*}{Dt^*} = \omega_j^* S_{ij}^* - \omega_i^* S_{kk}^* + \frac{1}{M^2}\frac{\epsilon_{ijk}}{\rho^{*2}}\frac{\partial \rho^*}{\partial x_j^*}\frac{\partial p^*}{\partial x_k^*} + \sqrt{\frac{A}{1+A}}\frac{1}{Re_p}D_j^*\,, \tag{4.24}$$

where $D/Dt^* \equiv \partial/\partial t^* + u_j^*\partial/\partial x_j^*$. In the above non-dimensional equation, baroclinic torque dominates dilatation when $M \ll 1$, for example in the weakly stratified case where $M = 0.3$. When $M \gtrsim 1$, by contrast, dilatation becomes increasingly strong compared to baroclinic torque.

The baroclinic torque itself has a Mach number dependence that is revealed by first writing this in terms of the specific volume $v^* \equiv 1/\rho^*$ as

$$\frac{1}{M^2}\frac{\epsilon_{ijk}}{\rho^{*2}}\frac{\partial \rho^*}{\partial x_j^*}\frac{\partial p^*}{\partial x_k^*} = -\frac{1}{M^2}\epsilon_{ijk}\frac{\partial v^*}{\partial x_j^*}\frac{\partial p^*}{\partial x_k^*}\,. \tag{4.25}$$

We can then split v^* and p^* into hydrostatic and fluctuating parts as

$$v^*(x_1, x_2, t) = v_0^*(x_1^*) + v'^*(x_1, x_2, t)\,, \quad p^*(x_1, x_2, t) = p_0^*(x_1^*) + p'^*(x_1, x_2, t)\,, \tag{4.26}$$

where $v_0^* = 1/\rho_0^*$, and ρ_0^* and p_0^* are given by Eqs. (6.15) and (6.14), respectively. Using this decomposition, it can be shown that Eq. (4.25) can be written as

$$\frac{1}{M^2}\frac{\epsilon_{ijk}}{\rho^{*2}}\frac{\partial \rho^*}{\partial x_j^*}\frac{\partial p^*}{\partial x_k^*} = -\left[\frac{1}{M^2}\epsilon_{ijk}\frac{\partial v'^*}{\partial x_j^*}\frac{\partial p'^*}{\partial x_k^*} + M^2(1 \mp A)\left(v_0^*\frac{\partial p'^*}{\partial x_2^*} + p_0^*\frac{\partial v'^*}{\partial x_2^*}\right)\right]\,. \tag{4.27}$$

Substituting this into Eq. (5.23) then gives

$$\frac{D\omega_3^*}{Dt^*} = \left[\omega_j^* S_{ij}^* - \omega_i^* S_{kk}^* - (1 \mp A)\left(v_0^*\frac{\partial p'^*}{\partial x_2^*} + p_0^*\frac{\partial v'^*}{\partial x_2^*}\right)\delta_{i3} + (1 \mp A)\left(v_0^*\frac{\partial p'^*}{\partial x_3^*} + p_0^*\frac{\partial v'^*}{\partial x_3^*}\right)\delta_{i2}\right] - \frac{1}{M^2}\left[\epsilon_{ijk}\frac{\partial v'^*}{\partial x_j^*}\frac{\partial p'^*}{\partial x_k^*}\right] + \sqrt{\frac{A}{1+A}}\frac{1}{Re_p}D_3^*\,.$$

When operating in 2D (i.e., x1 and x2 coordinates) this reduces to

$$\frac{D\omega_3^*}{Dt^*} = \left[-\omega_3^* S_{kk}^* - (1 \mp A)\left(v_0^*\frac{\partial p'^*}{\partial x_2^*} + p_0^*\frac{\partial v'^*}{\partial x_2^*}\right)\right] - \frac{1}{M^2}\left[\epsilon_{3jk}\frac{\partial v'^*}{\partial x_j^*}\frac{\partial p'^*}{\partial x_k^*}\right] + \sqrt{\frac{A}{1+A}}\frac{1}{Re_p}D_3^*\,. \tag{4.28}$$

Note that in this expression, the fluctuating baroclinic torque term is large in comparison to the leading dilatation and baroclinic torque terms when M is small, but is comparatively smaller when $M \gtrsim 1$. Effectively this means that the dynamics are dominated by fluctuating baroclinic torque when M is small, and by dilatation and the background baroclinic torque when M is large.

4.3.4 Vortex Analogs

As RTI develop, one of the key features in their growth is the development of vortical structures[43, 64]. In two dimensions this first manifests itself as the formation of a pair of counter rotating vortices while in three dimensions, it manifests as a vortex ring. This transformation from the initial perturbation to these vortical structures is what ends up driving the instability. As it continues to grow, this first vortical structure remains intact, and eventually begins shedding additional vorticity along the sides of the bubble and spike to form the Kelvin-Helmholtz instability. For this reason, these initial vortical structures are imperative to the growth of the RTI as they lead to growth of the entire instability.

To further understand the effects of compressibility and background stratifications on the growth of RTI, an investigation into the effects onto these vortical structures by themselves can be carried out. To perform these simulations, a similar methodology is carried out to initialize them as the RTI. The same background state is used as the RTI case but with $A = 0$ so that there is no density discontinuity in the domain. The same non-dimensional parameters are all used to describe the vortex analog case so that the comparison can be one to one.

To complete the initialization, an imposed velocity field must be applied. For the vortex pair the initialization is

$$u_1 = -\sum_{i=1}^{2} \frac{\Lambda}{\sigma^2}(x_2 - x_{2,i})\exp\left(-\frac{(x_1 - x_{1,i})^2 + (x_2 - x_{2,i})^2)}{\sigma^2}\right) \tag{4.29}$$

$$u_2 = \sum_{i=1}^{2} \frac{\Lambda}{\sigma^2}(x_1 - x_{1,i})\exp\left(-\frac{(x_1 - x_{1,i})^2 + (x_2 - x_{2,i})^2)}{\sigma^2}\right) \tag{4.30}$$

so that the velocities are described by a Gaussian distribution with the summation being for the two different vortices. The center of each vortex is located at $(x_{1,i}, x_{2,i})$, and the width is describe by σ. The strength of the vortex pair, Λ, is set so that the circulation over each vortex matches that of the vortices generated by the RTI. A comparison of the velocity fields for the vortex pair case and two dimensional RTI case can be found in Figure 4.2.

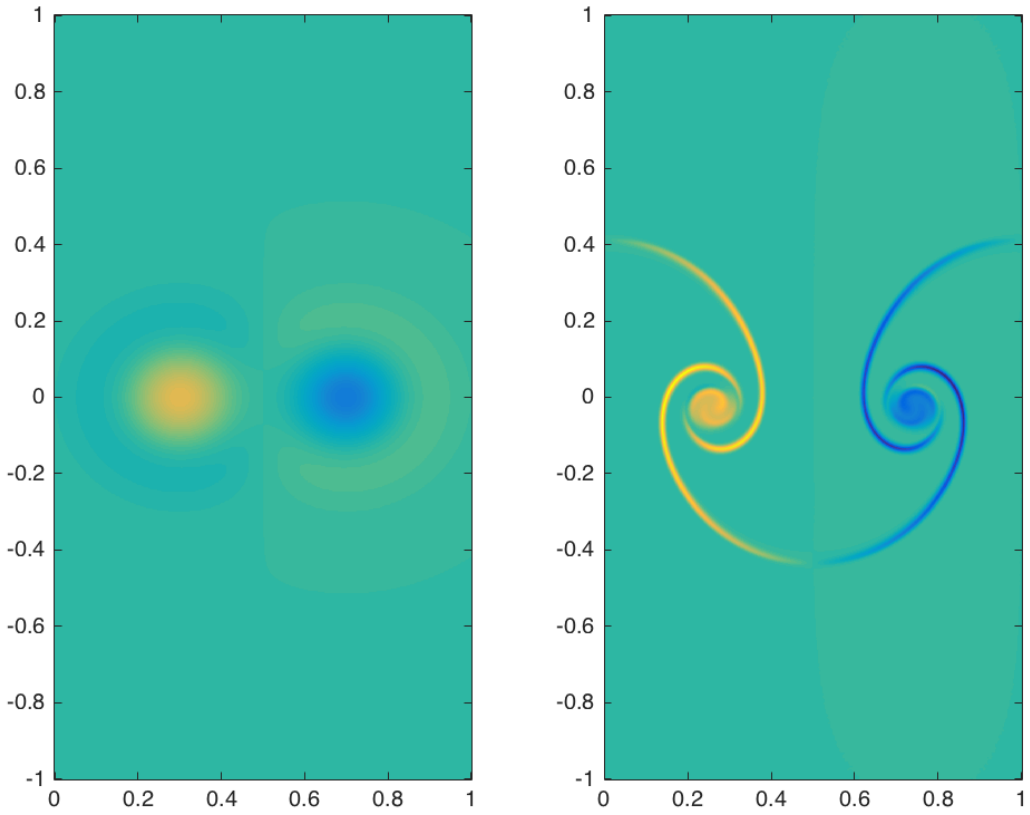

Figure 4.2: A comparison of the initial velocity field for the vortex pair simulations and the resulting velocity field from the development of the vortex pairs through RTI.

4.4 Numerical Method

The RTI problem lends itself naturally to state-of-the-art adaptive numerical methods. To effectively capture the instability growth, very long domains are needed to ensure late-time growth is captured, but very small grid spacing is needed to fully resolve the high gradients at the interface of the instability. This would equate to having a very dense grid and incredibly high computational costs. During the majority of the simulation, however, the grid far away from the interface is unnecessary due to the flow being quiescent, and thusly, through the use of adaptive methods, high grid compression rates can be achieved. A method that has proven effective at doing this, is the Parallel Adaptive Wavelet Collocation Method (PAWCM), and it is what has been applied here[51, 52].

PAWCM uses the natural properties of the wavelet transformation to locate areas of steep gradients and gives direct control over the amount of resolution applied based on how steep these gradients are. Essentially, through PAWCM a flow field variable is transformed into wavelet space resulting in wavelet basis functions and coefficients that are localized in both wave space and physical space. From there, the coefficients are passed through a thresholding filter where all the coefficients above the parameter ϵ are kept, and any of those below are set to zero. The resulting thresholded decomposition appears as follows

$$u_{\geq}(x) = \sum_{k} c_k^0 \phi_k^0(x) + \sum_{j=0}^{\infty} \sum_{\mu=1}^{2^n-1} \sum_{\substack{l \\ |d_l^{\mu,j}| \geq \epsilon ||u||}} d_l^{\mu,j} \psi_l^{\mu,j}(x), \tag{4.31}$$

where u is any variable, ϕ_k are the scaling functions on the coarsest level, c_k are the corresponding coarse level wavelet coefficients, ψ_l are the scaling interpolating functions on any arbitrary level, d_l are the coefficients that the thresholding is applied to, l and k represent physical grid points, and μ and j represent the wavelet family and level of resolution, respectively [61, 47]. The equivalence of setting one of these coefficients, d_l, to zero is the removal of a grid point at that level of resolution. d_l itself is a large value when in the presence of a large gradient, and is small when it is in a relatively constant region. This method results in the error being of the order of which we set ϵ

and the effective resolution being set by a base grid size and the limit put on j (referred to as j_max from here on). This results in the error being $\mathcal{O}(\epsilon)$ and the resolution in a single direction being $2^{(j_{max}-1)} * p$ where p is the base resolution[61, 55, 47].

PAWCM has been implemented in a way that enables it to work with finite difference methods. For this method, fourth order central differences have been applied spatially, and a third order total variation diminishing explicit Runge-Kutta method scheme has been applied in time. PAWCM also boasts many modern features besides its adaptivity to enable fast and efficient processing. It is highly parallelized, having successfully run on up to 5000 cores, and it is able to do arbitrary domain decompositions using the Zoltan library. It has a tree-like data structure for easy MPI communications, and direct error control. All of this results in the fact that any additional overhead from the wavelet methodology is made up for by using many processors and a 90%+ grid compression[61, 55, 47].

Given this methodology, it is necessary to determine the parameters on which to adapt the grid for the numerical simulation. Since the wavelet method is so flexible, it is possible to generate the grid on any flow field variable that is calculable. It was determined for the initial time steps that the important parameters to adapt on are the vorticity, the norm of the strain rate tensor, and the gradient of the species in addition to the normal parameters of the velocity and species fields. An example of the resulting grid from this this adaptation can be seen in 4.3. As the simulation progresses, though, it is possible that the later time flow field would become more complex and require further adaptation. An example of two of these grids based on more complex flow field variables, namely the baroclinic torque term from the vorticity equation and the divergence of velocity, can be seen in Figure 4.4. Through many attempts, it was found that by including adaptation on the baroclinic torque, a more complete grid could be maintained and generated throughout the simulation. This information not only allows proper grid generation, but also informs that this term must be an important flow field quantity.

To effectively capture these simulations, proper boundary conditions must be used. On the boundaries all sides that can be taken as periodic are, i.e. the boundaries in the x_2 and x_3 directions.

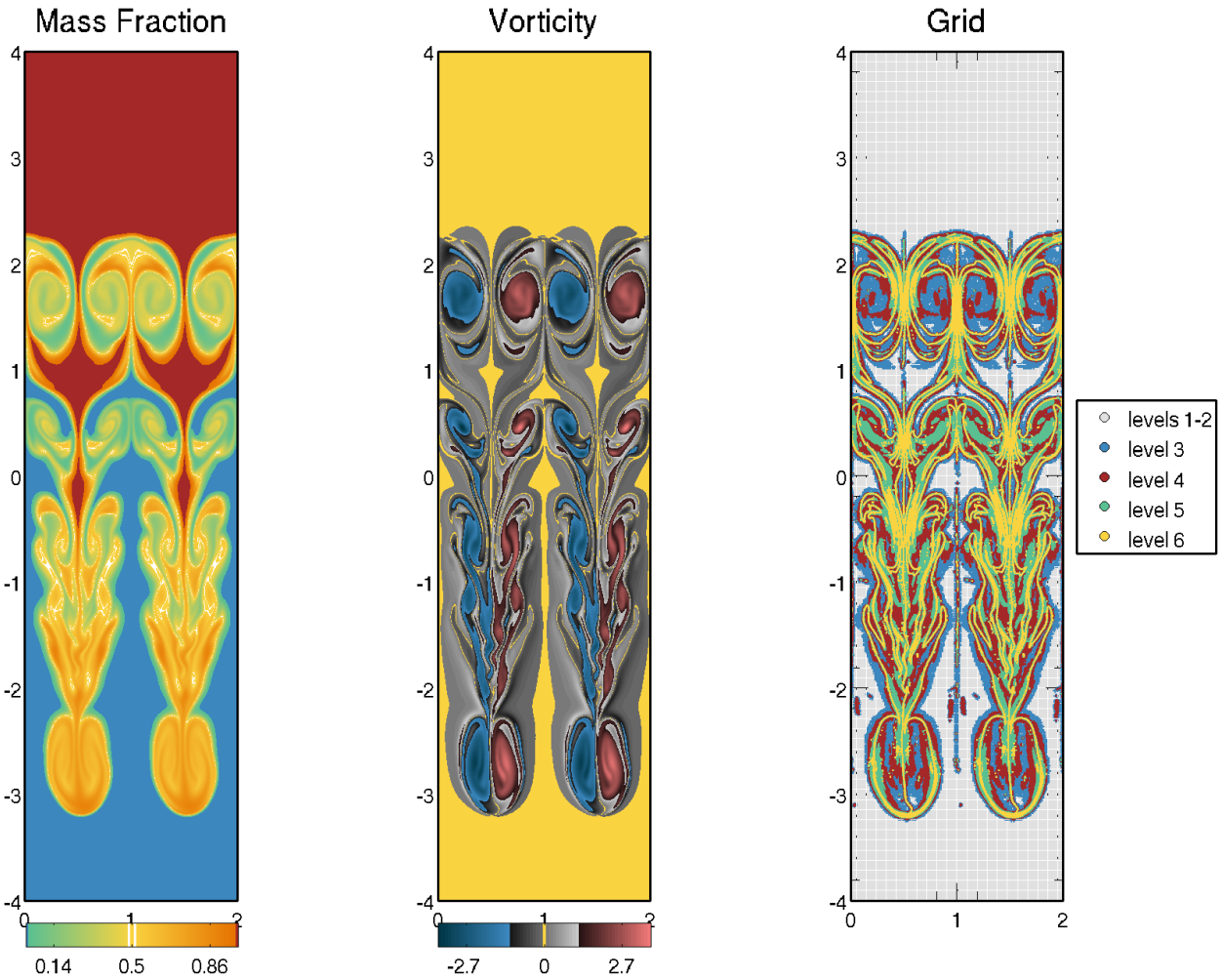

Figure 4.3: An example of a simulation done at Mach number 0.3 and Reynolds number 5,000 with adaptation on the species, gradient of the species, velocity, vorticity, and the norm of the strain rate tensor. The leftmost image shows the mass fraction, the center shows the vorticity field, and the right shows the resulting grid from adaptation.

In the x_1 direction, at the top and bottom of the domain, careful thought must be given to the boundary conditions implemented. The goal is to essentially mimic an infinite domain, but to ensure both the background stratification is preserved and that none of the shocks are reflected back into the domain. To do this, shear free slip boundary conditions were put in place with the addition of numerical diffusion buffer zones before them. These buffer zones ensure that any shockwaves sent to the boundaries are dissipated before reaching the end to ensure that issues don't arise as the waves try to leave the domain and the waves are fully dampened so no reflections can

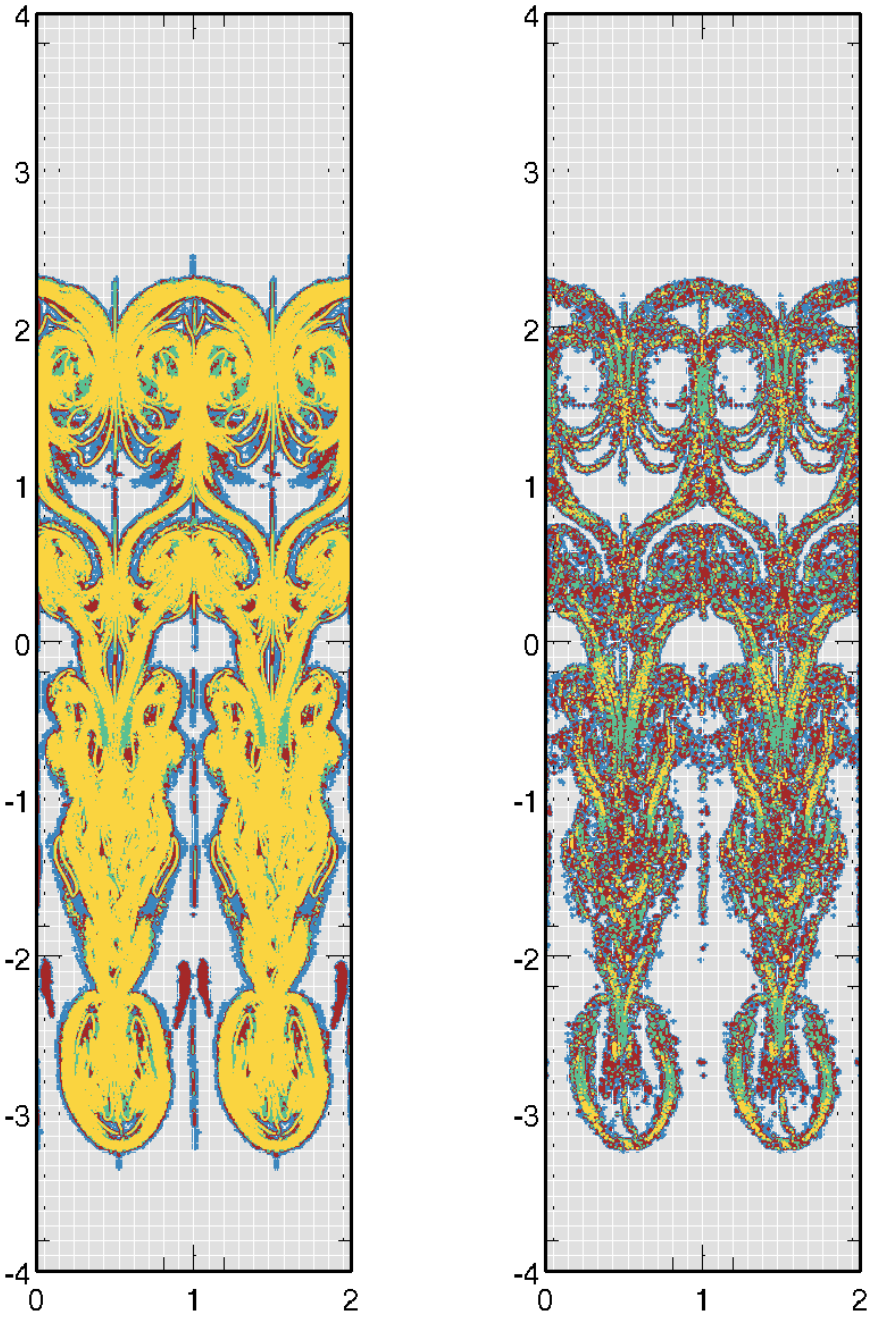

(a) Baroclinic Torque

(b) Divergence of Velocity

Figure 4.4: Example grids generated by calculating derived flow field quantities. The grid on the left is made by adapting on the baroclinic torque term from the vorticity equation, and the grid on the right is generated by adapting on the divergence of the velocity field. The scales are the same as from 4.3.

take place[52].

To ensure the simulations are fully resolved, multiple checks were put into place. Normal convergence studies for this investigation can be found in [52]. It has been found, though, that there are even more constraints to ensure the accuracy of the simulation. Due to the extreme sensitivity to initial conditions, it was found that even when the simulation appeared to be completely resolved, that error in the initial conditions would add additional modes to the late time perturbation growth. An example of this can be seen in Figure 4.5. Essentially, this shows that great care must be taken to fully resolve the initial conditions. The various factors into the minimization in the initial conditions were studied and it was discovered that the root cause was determined by asymmetrical initialization of the species mass fraction. The asymmetrical aspects of all other fields were determined to be on the level of machine precision.

The three parameters of interest in determining the asymmetry of the initial species field were the thresholding parameter, determined by ϵ, the thickness of the initial diffusion layer, determined by the number of points across the interface of the two fluids at the finest resolution p_I and thusly the thickness used in the solution of the diffusion equation, and the resolution, determined by the wavelet parameter j_{max}. Figure 4.6 shows a summary of the results for this asymmetry study. As ϵ is decreased towards 10^{-8}, it is clear that the error is minimized, and for the initial time steps, the cost of having an extremely low ϵ around 10^{-8} is negligible, and thusly the following results were obtained with that as the initial parameter. For the thickness of the interface, two competing effects were found. In general, it was discovered that the thicker the interface was made, the larger the asymmetry of the initial conditions. At the same time, though, it was found through many simulations that a thicker interface acts as a buffer layer to absorb other numerical errors. Based on these two competing effects, the number of points across the interface was chosen to be 16, to both minimize the asymmetry and to gain some of these buffering effects. Finally, it was found that higher resolutions lead to better initial conditions. At a level of $j_{max} = 7$ it was found that the asymmetry drops below machine precisions, and thusly this level of resolution was deemed sufficient for the simulations.

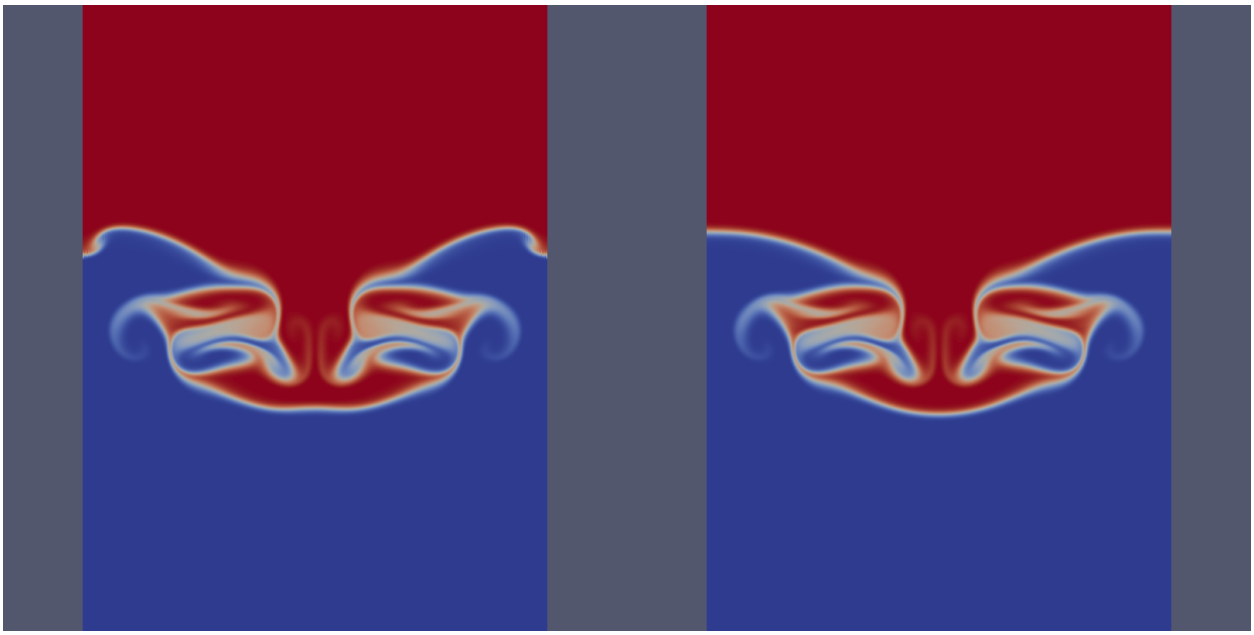

Figure 4.5: Asymmetry in the initial conditions leads to secondary modes developing in late time growth. In this example, a Mach number of 1.2 was used. The image on the left was initialized with a smaller value of ϵ leading to the development of additional modes that appear as concavities on the tips of the bubble and spike formations.

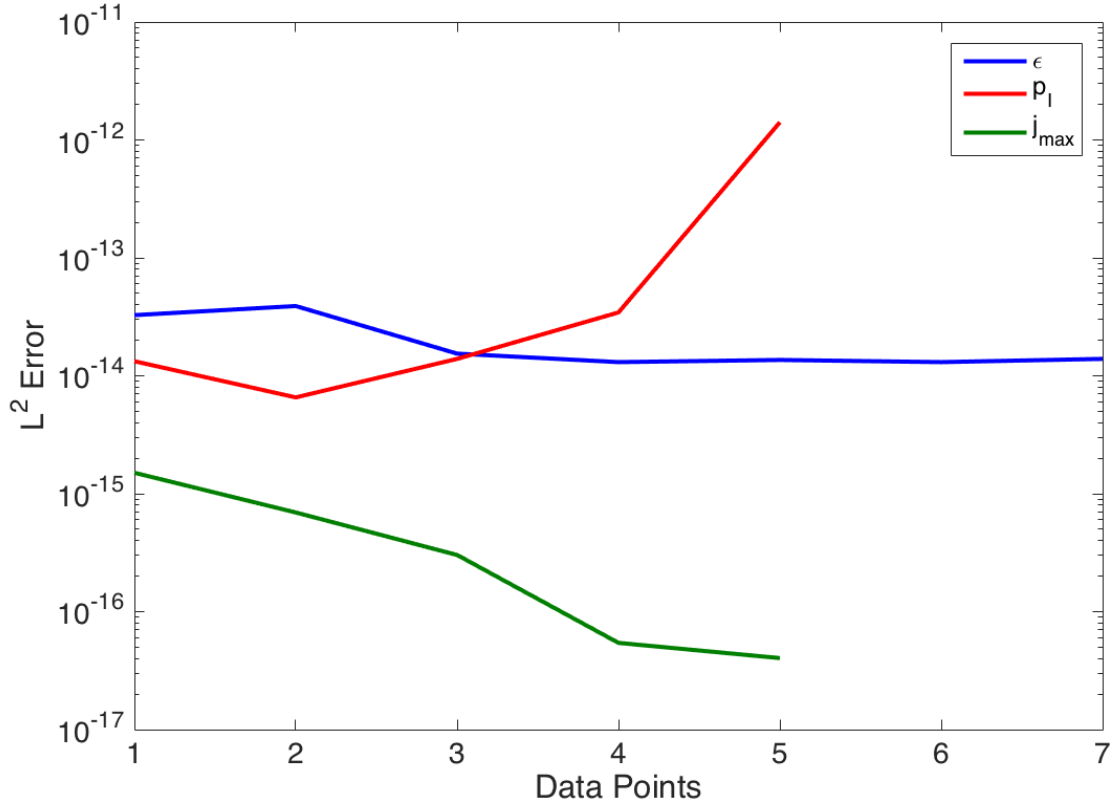

Figure 4.6: An investigation of the effects of various simulation parameters on the asymmetry of the initial species field. Blue shows the effects of the thresholding parameter, ϵ, with values from 10^{-2} to 10^{-8} in increments of 10^{-1}. Red shows the effects of the interface thickness ranging from 4 to 64 by powers of 2, and green shows the effects of resolution through the j_max parameter of the wavelet decomposition ranging from 4 to 8 by increments of 1 with the same base resolution.

4.5 Results

4.5.1 Rayleigh Taylor Instability

The RTI simulations have been carried out in a domain of size $[-8\lambda, +8\lambda]$ X $[0, \lambda]$ in two dimensions and $[-4\lambda, +4\lambda]$ X $[0, \lambda]$ X $[0, \lambda]$ in three dimensions, where λ corresponds to the wavelength of the applied perturbation. The maximum resolution in the x_1 direction was 65,536 for the two dimensional case, and 32,768 for the three dimensional case. In the x_2 and x_3 directions, the maximum resolution was kept at 4,096 grid points. The Atwood number studied for these cases was kept constant at 0.04, and the Mach numbers used were 0.3 (nearly incompressible), 0.6, 0.9, and 1.2. The perturbation Reynolds numbers investigated were 5,000, 10,000, and 20,000. The highest was of particular interest because it has shown to be the minimum perturbation Reynolds number necessary to reach the chaotic growth regime for the incompressible limit of this particular case [64].

The first investigation was to simultaneously look at the effects of stratification strength and the perturbation Reynolds number on the growth of RTI. Figure 4.7 shows the growth of RTI as a function of both time and Mach number. It becomes quite clear that increasing isothermal stratification strength has vast impacts on RTI growth. As stratification strength increases, the instability growth is greatly suppressed.

This complete suppression occurs at every stratification besides the weakest. This is further elaborated in the plot of bubble and spike height as a function of time in Figure 4.8. It is clear that for all of the moderate to higher stratifications, they approach a growth limit asymptotically. It is also interesting to note that in comparison to the incompressible case, from Tei and Livescu's work, not even the lowest stratification is able to approach its growth rate. In addition, Tei, et al. found that for the low Atwood number case of 0.04, the bubble and spike growth was very symmetric until late times, while the weak stratification in the nearly incompressible limit experiences a much larger asymmetry that grows in time.

We can further investigate these effects by viewing the velocities of the bubble and spike

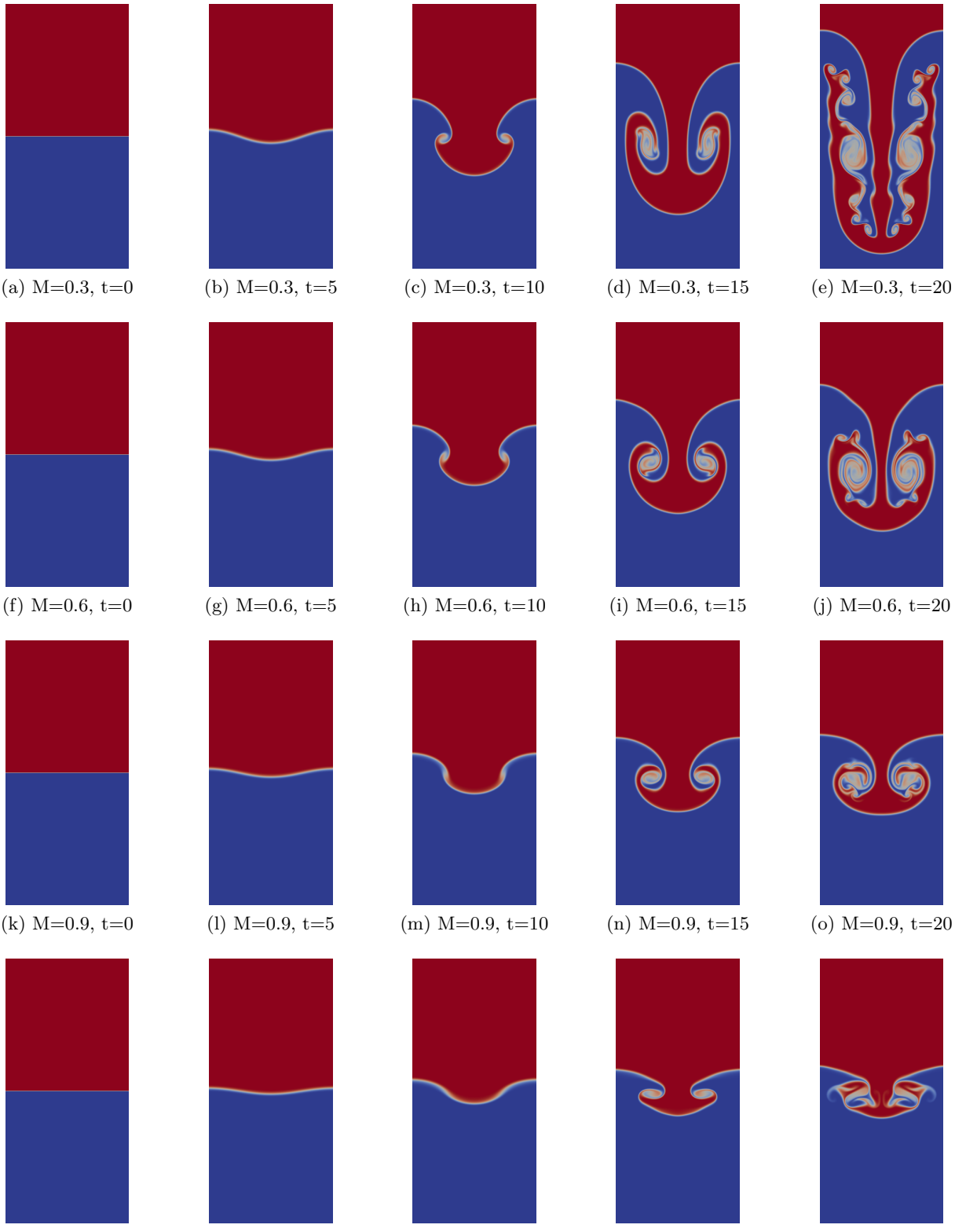

(a) M=0.3, t=0 (b) M=0.3, t=5 (c) M=0.3, t=10 (d) M=0.3, t=15 (e) M=0.3, t=20

(f) M=0.6, t=0 (g) M=0.6, t=5 (h) M=0.6, t=10 (i) M=0.6, t=15 (j) M=0.6, t=20

(k) M=0.9, t=0 (l) M=0.9, t=5 (m) M=0.9, t=10 (n) M=0.9, t=15 (o) M=0.9, t=20

(p) M=1.2, t=0 (q) M=1.2, t=5 (r) M=1.2, t=10 (s) M=1.2, t=15 (t) M=1.2, t=20

Figure 4.7: RTI growth as a function of time (left to right) and Mach number (top to bottom).

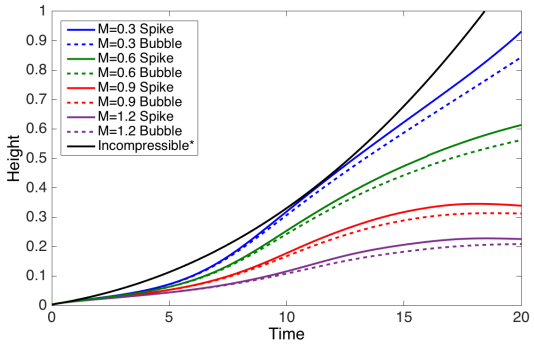

Figure 4.8: A plot of the growth of RTI height for both the bubble and spike tip as a function of time.

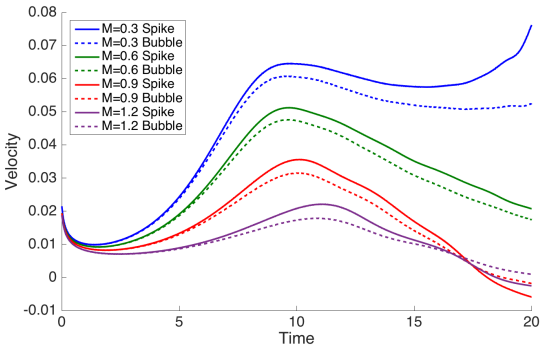

Figure 4.9: A plot of the velocity of the bubble and spike tips for RTI for the range of Mach numbers explored.

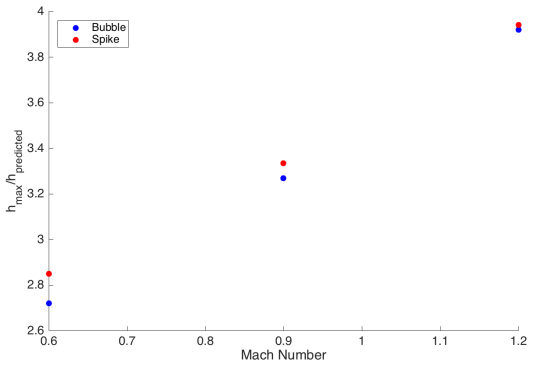

Figure 4.10: The ratio of the actual height achieved to the height predicted by the potential energy analysis as a function of Mach number. Blue dots represent the bubble, where red represents the spike. The lowest Mach number is omitted since full suppression has not been achieved.

tip over time. These velocities are plotted in Figure 4.9. It becomes immediately clear that the velocity of the larger Mach numbers all trend towards zero, confirming the complete suppression of the instability. For Mach number of 0.3 case, though, we can see the beginning of the reacceleration regime as the spike tip begins to rapidly accelerate towards the end. The exaggerated asymmetry can be seen by comparing the velocities of the bubble and spike for this case as well. It becomes apparent that even though the spike reaccelerates, the bubble remains at a nearly constant velocity in the late time, resulting in the spike's height increasing at a much faster rate than the bubble.

In an attempt to try to predict this point of full suppression, an analysis was performed based on the initial potential energy of the system. Essentially, the potential energy was calculated based on the initial density jump and relative to the point at which the density of the light fluid should be equal to that of the heavy fluid. The results are presented in 4.10 where it is presented as the ratio of the distance actually traveled to the distance predicted by the potential energy analysis. It becomes readily apparent that the distance predicted by the potential energy underestimates the actual distance traveled. It is also important to note that this trend is not perfectly matched with a linear fit, but rather needs higher order terms to capture the behavior.

The second part of this investigation was to study the effects of Reynolds number on the growth of these RTI scenarios. In Figure 4.11, it is evident that Reynolds number has minimal

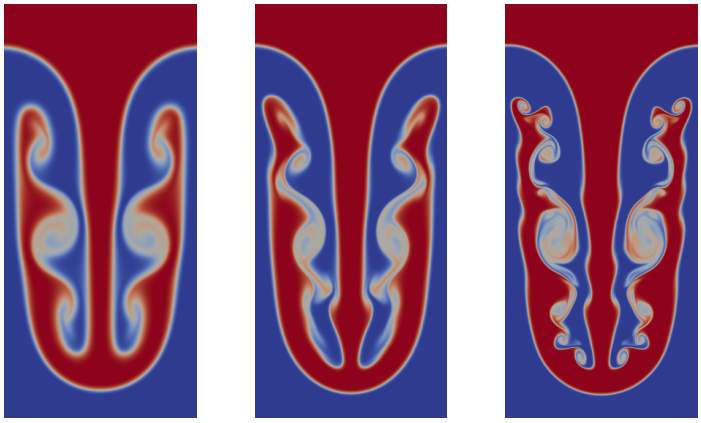

(a) M=0.3, $Re_p = 5,000$ (b) M=0.3, $Re_p = 10,000$ (c) M=0.3, $Re_p = 20,000$

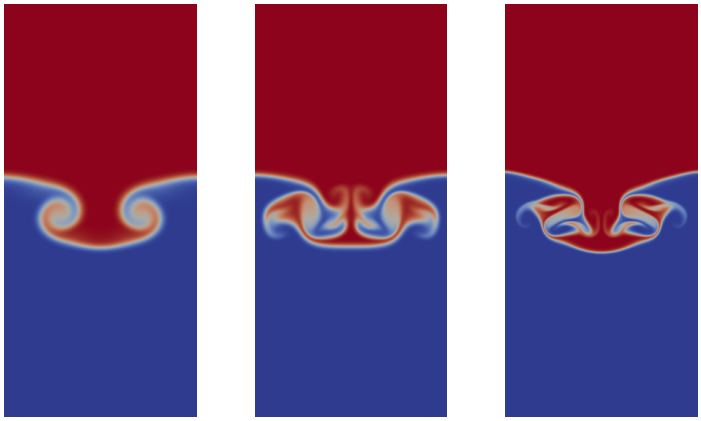

(d) M=1.2, $Re_p = 5,000$ (e) M=1.2, $Re_p = 10,000$ (f) M=1.2, $Re_p = 20,000$

Figure 4.11: Reynolds number effects on RTI growth. The top figures show the results for various Reynolds number for the low stratification while the bottom shows it for high. All images are at t=20.

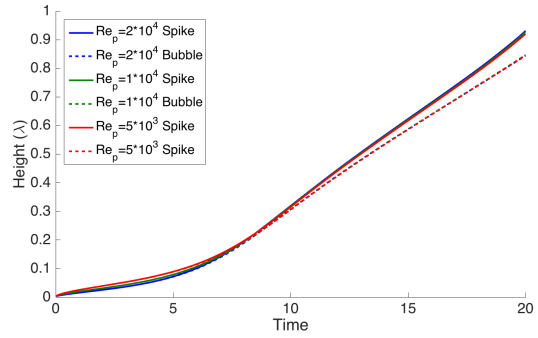

(a) Height

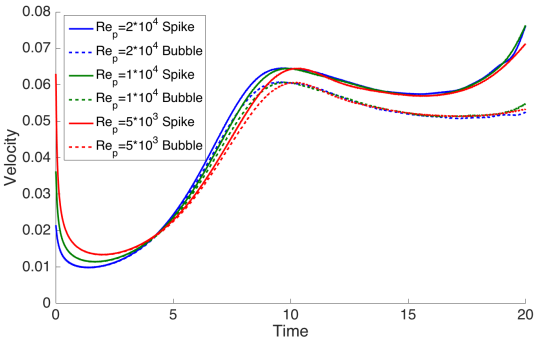

(b) Velocity

Figure 4.12: The growth of the height and corresponding velocities for both the bubble and spike for various Reynolds numbers at M=0.3. It is clear that the Reynolds number has minimal effect.

effect on the development of the bubble and spike heights of RTI. Looking closer, as is expected, with lower Reynolds numbers, the higher viscosity smears the smallest scales. This leads to significantly less small scale development. To further investigate these phenomenon, we can again look at the plot of the bubble and spike heights over time, as well as the corresponding velocities. This is plotted in Figure 4.12. In this plot, we explore specifically the growth of the low Mach number case as a function of Reynolds number. It becomes immediately clear that even for the low Mach number case, Reynold's number plays an insignificant role, as the growth and velocities remain largely the same regardless of the viscous effects. Based off of this it is easy to conclude that Mach number has a much greater effect on the growth rate than the perturbation Reynold's number.

From these conclusions, though, a further investigation into the effects of Mach number was performed at a Reynolds number of 5000. From the high Reynolds number results, it is already known that the suppression occurs somewhere between a Mach number of 0.3 and 0.6. Based on this, simulations were performed at the intermediate Mach numbers in which it was discovered that the most significant changes occur M=0.5 and M=0.6. In Figure 4.13, the growth of the height and velocities of the instability are plotted as a function of time. At the Mach number of 0.3, complete suppression is still not achieved, but even at a Mach number of 0.5, the velocity of the bubble and spike still tends towards zero. It is also clear that the suppression happens on a spectrum from these figures. Namely, in many of these cases such as the Mach number of 0.5, 0.525, and 0.55, the instability is even able to begin reaccelerating only for the suppression to over power and halt the growth. In the following sections, the goal is to further understand how the stratification is able top enact these effects.

4.5.2 Vortex Pairs

To help further our understanding of these suppressive effects of the background stratification, we also simulated vortex pairs traversing through the same stratified media. As mentioned before, the strength of these vortex pairs was set based upon the strength of vortices generated by the RTI. The end results for one of these initializations can be found in Figure 4.2. Essentially, for every

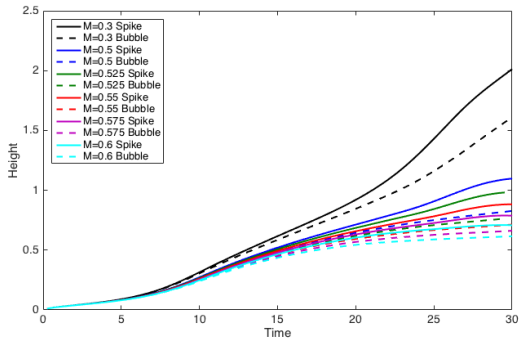

(a) Height

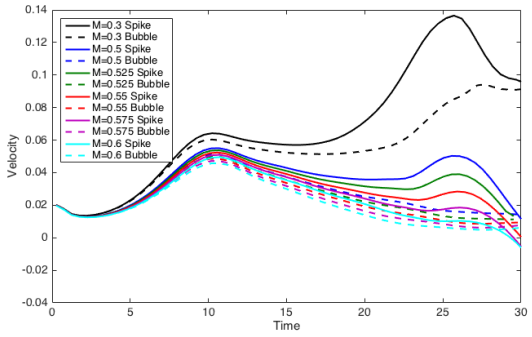

(b) Velocity

Figure 4.13: The growth for the height and velocity of the bubble and spike formations at a variety of Mach numbers from 0.3 to 0.6 at a Reynolds number of 5000. This shows that spectrum on which the suppression occurs.

RTI case carried out, we are able to simulate two analog versions due to the periodic nature of the simulations. To fully capture the effects, we need to simulate both the vortex pair propagating upwards through the fluid, i.e. mimicking the bubble, and also the pair propagating downwards through the fluid to capture the interactions of the spike. So essentially, each of the RTI cases has two corresponding vortex pair cases to help further elaborate the physics. For these cases, the domains were chosen to be [-4λ, +4λ] x [$-\lambda$,+λ], and the maximum resolution was set to be 8,192 points by 2,048 points, making them significantly cheaper simulations to carry out.

Similarly, it was found for this stratification that Reynolds number played a minimal role in the development of the flow, so the rest of these results will focus on the outcome of the Mach number investigation. Essentially, through these studies, it was found that even the weakest stratification resulted in the destruction of the vortex pair given enough time. Through the simulations we would see the initial intertwining of the pair that would lead to the propagation of some amount of vorticity in the direction of the induced velocity, but then the background stratification would cause a reversal of this transversal through the baroclinic torque term in the vorticity equation. In the highest stratification, though, not even a small amount of transversing can be see, instead the vortical structures are completely destroyed from the beginning. An example of the late time vortical structures can be found in Figure 4.14. It can be seen that the destruction caused by the strong stratification essentially leads to just random vortical noise being created, where the weak stratification is able to maintain its structure, although the distance the vortices move is greatly suppressed by the generation of vorticity in the opposite directions in the surrounding area

To further investigate the simulations, and to better compare the results of the vortex pair simulations to the RTI simulations, the respective velocity fields can be decomposed into the components of the vorticity equation. A comparison of the vorticity fields for the RTI and vortex pair simulations at the highest and lowest Mach numbers can be found in Figure 4.15. Investigating the terms of the vorticity equation, there are multiple terms that we can ignore in this analysis. Because the simulations are two dimensional, vortex stretching will not play a role, and because the gravitational body force is constant, the body force can be ignored. Finally, the dissipation

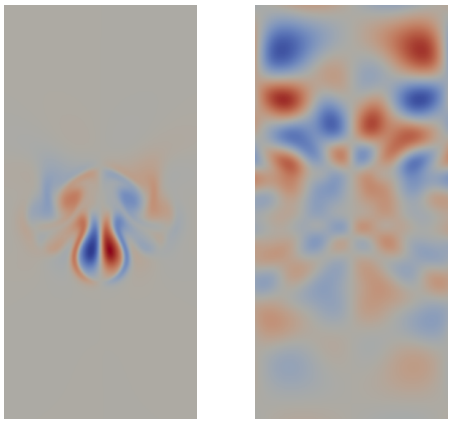

(a) M=0.3 (b) M=1.2

Figure 4.14: A plot of the vorticity fields to show the background stratification effects on the transversing of counter rotating vortex pairs. It can be seen that the high stratification (right) essentially breaks the structures down and generates noise, while the low stratification (left) is able to travel through the domain.

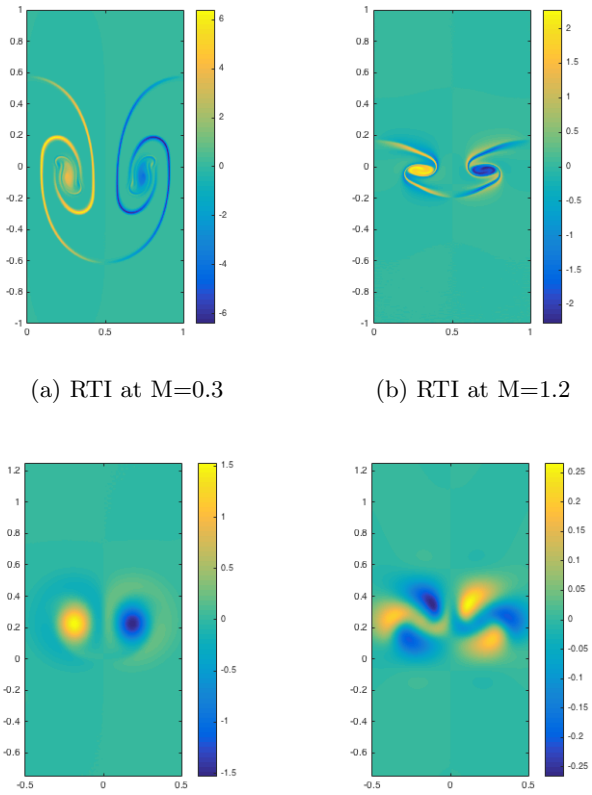

(a) RTI at M=0.3

(b) RTI at M=1.2

(c) Vortex Pair at M=0.3

(d) Vortex Pair at M=1.2

Figure 4.15: The vortical structures resulting form the RTI simulations (top) and vortex pair simulations (bottom) at both M=0.3 (left) and M=1.2 (right). They exhibit very clear similarities in structure at the same Mach number, and clear differences when comparing between the two stratifications

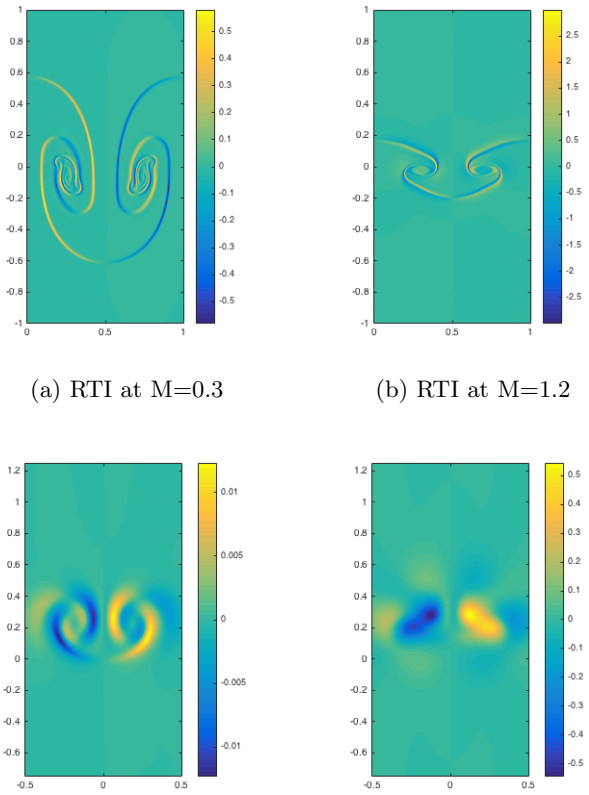

(a) RTI at M=0.3

(b) RTI at M=1.2

(c) Vortex Pair at M=0.3

(d) Vortex Pair at M=1.2

Figure 4.16: The resulting baroclinic production fields for RTI (top) and vortex pair (bottom) at low, M=0.3 (left), and high, M=1.2 (right), background stratifications. The baroclinic production term is responsible for the destruction of the vortical structures by the stratification as can be seen in all cases.

term will just remove vorticity through viscous effects, so it will not greatly influence the growth patterns. Between the final two terms, namely the baroclinic production and dilatation terms, it was found that the baroclinic effects were consistently two orders of magnitude greater than the dilatational effects. Based on this, the most important effects can be understood through the baroclinic production term. The resulting fields can be found in Figure 4.16. From this it becomes apparent that the destruction of vortical structures arises from the baroclinic production term, and this destruction results in the suppression of growth. It is also important to note the similarities of the structures that develop at the same stratification between the RTI and vortex pair cases.

Based off of these findings, we are able to track the core of the vortices by locating the position of the maximum of the vorticity. This measure allows us to know essentially how far a pair of vortices can travel through various stratified media. If we take these values and plot them against the maximum distance that RTI are able to travel through the same stratified media, an interesting relationship can be found. The resulting plot for the spike analysis can be seen in Figure 4.17. The trend that this plot shows in undeniable, and does better at capturing the behavior than the previous potential energy analysis. Using this method of simulating vortex pairs, we should be able to predict the stopping point of any RTI in the same isothermal stratification. Essentially what this means is that, though there is initially enough potential energy to generate the first vortex pair, isothermal background stratifications are strong enough that they result in the destruction of these pairs before enough momentum can be generated to further propagate the RTI system.

To test whether or not this is applicable to the entire regime explored in this paper, an investigation can be done to discover whether or not the low Mach number case of 0.3 will stop at the predicted point. Though simulating the fully resolved perturbation Reynolds number of 20,000 to this point would be prohibitively expensive, it has already been shown above that Reynolds number has minimal effect on the growth exhibited. For this reason, the $Re_p = 5,000$ case was allowed to continue evolving to either confirm or deny these effects. The results can be seen in Figure 4.18. Unfortunately, this proves that the predictive power has some limitations. In the case of the lowest Mach number, the instability is able to generate enough momentum so that

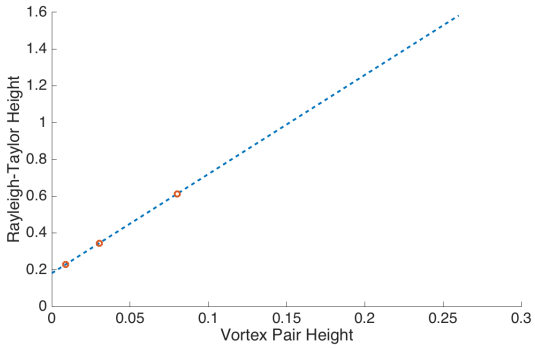

Figure 4.17: A plot of the growth of RTI spike height compared to the distance traveled through the same stratified media by a pair of vortices.

the background stratification is overcome, and the RTI growth can continue past the point that the vortex pair analysis predicts it to stop. This means that somewhere in between $M = 0.3$ and $M = 0.6$ there is a regime change where the isothermal background stratification will not fully suppress the growth of RTI, and thusly cannot be predicted by the vortex pair interactions.

4.5.3 Expanded Vorticity Results

Even through the comparison of the RTI with the vortex pairs, a full understanding of the mechanism responsible for the suppression of the instability is still lacking. Through understanding the evolution of the vorticity, we can also hope to garner a full understanding of this suppression mechanism. To better this understanding, a time series of the vorticity for the highest and lowest Mach numbers is shown in Figure 4.19. To get an even clearer picture, we can average the vorticity in half the domain, i.e. in the region where $0 \leq x_2 \leq 0.5\dot{}$The result essentially allows us to view the total effective vorticity in the system and this can be viewed in Figure 4.20. To understand the loss of vorticity in higher strength stratifications, the standard vorticity equation lends some insight, but it is only through the modified vorticity equation presented in Equation 6.18 that the full picture can be seen. Referring back to the equation, there are 4 terms of interest, excluding the viscous dissipation term. The first term is the standard dilatation term, the second term captures the effects of the perturbation pressure, the third term encompasses the perturbation specific volume

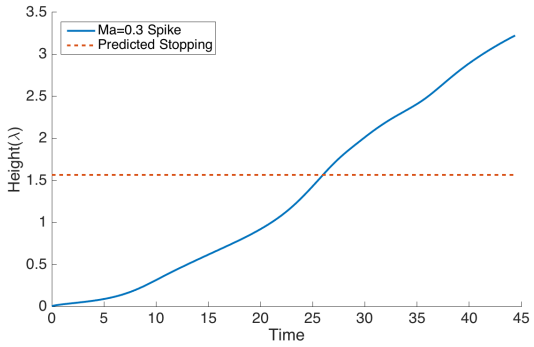

Figure 4.18: The growth of the $Re_p = 5,000$ and M=0.3 case over time (blue line) in comparison to the predicted stopping point based on the vortex pair analysis (the orange dotted line).

or density effects, and the fourth and final term shows the effects of the perturbation baroclinicity.

The first two terms, namely the dilatation and perturbation pressure terms, work on a smaller order of magnitude than the second two. In Figure 4.21, examples of these fields can be seen for the highest and lowest stratification strengths. It becomes quite evident that in addition to being orders of magnitude less than some of the other terms, they actually even oppose each other in their growth. The dilatation term acts by enhancing the vorticity responsible for driving the spike downwards and removes the vorticity driving the bubble. On the other hand, the pressure perturbation term does the exact opposite, i.e. it works to enhance the bubble growth but diminish the spike growth. In the high Mach number regime, these terms roughly cancel each other out, but in the lower Mach number regime, the dilatation strength is significantly higher and could contribute to the asymmetry of the late time growth.

The third and fourth terms are largely responsible for the overall growth of the instability. In particular, the third term, i.e. the perturbation specific volume, acts as the main mechanism for the growth of the instability as a whole. In Figure 4.22, the progression of the perturbation specific volume term can be seen for both the high and low stratification strength case. Immediately, a few things become apparent. Firstly, the low stratification strength case, i.e. M=0.3, has a significantly increased magnitude throughout time which results in the generation of more vorticity as a whole. Secondly, in the low strength scenario, this term mainly acts as source of additional vorticity, except

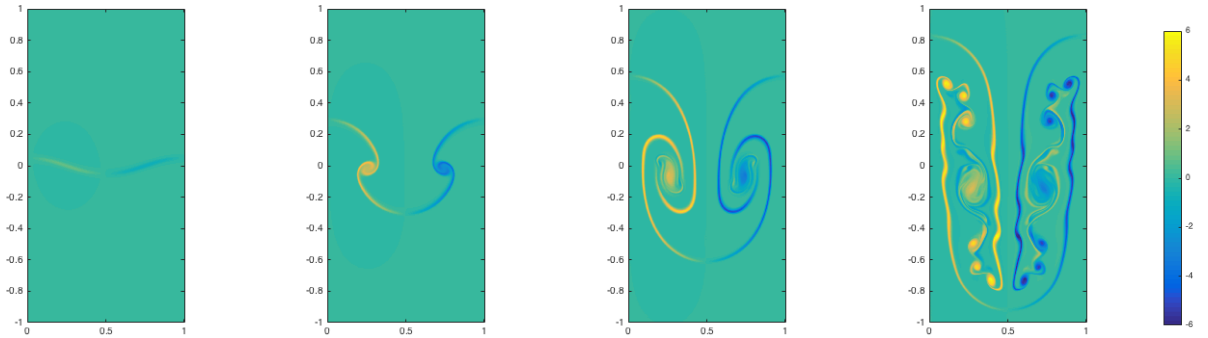

(a) M=0.3, t=5 (b) M=0.3, t=10 (c) M=0.3, t=15 (d) M=0.3, t=20

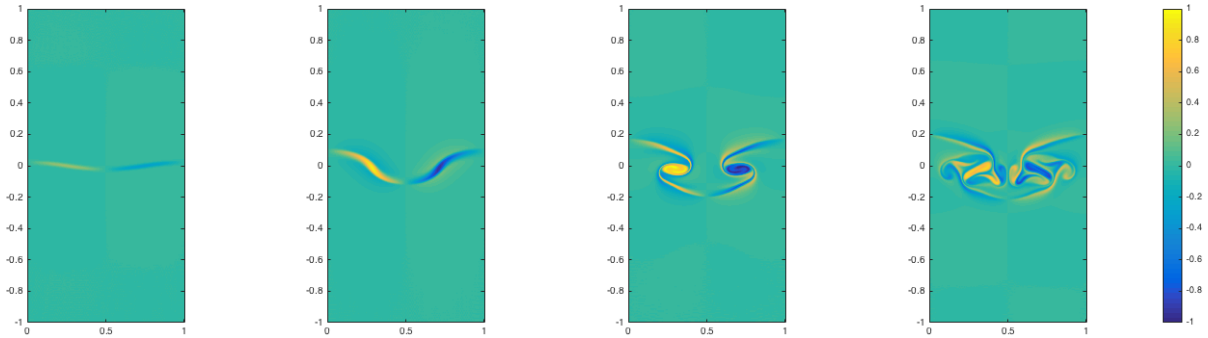

(e) M=1.2, t=5 (f) M=1.2, t=10 (g) M=1.2, t=15 (h) M=1.2, t=20

Figure 4.19: The evolution of vorticity plotted over time (left to right) for both the M=0.3 case (top) and the M=1.2 case (right).

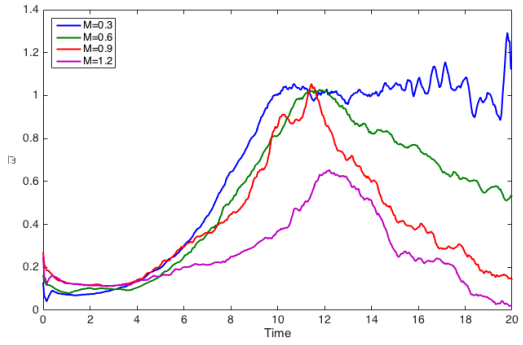

Figure 4.20: The evolution of the average vorticity over the left half of the domain. The lowest Mach number continuously increases while the rest of the numbers reach a peak vorticity and then begin decaying as the vortical structures are broken and suppression is reached.

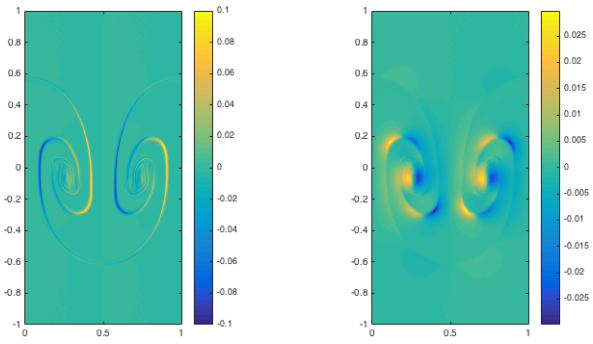

(a) Dilitation effects for M=0.3

(b) Pressure perturbation effects for M=0.3

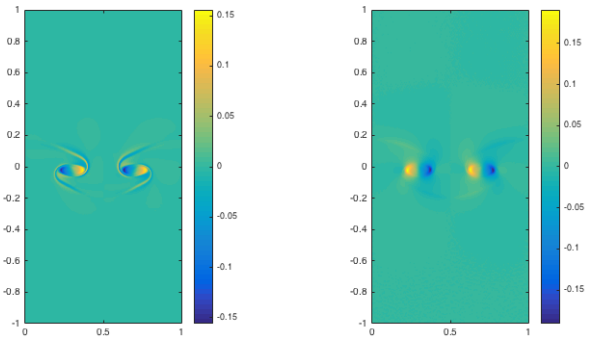

(c) Dilitation effects for M=1.2

(d) Pressure perturbation effects for M=1.2

Figure 4.21: The resulting fields for the first two terms of the modified vorticity equation for M=0.3 and M=1.2 at a t=15. It can be seen that these two terms largely counteract eachother and act on a small order of magnitude.

on the exteriors of the vortex pairs where the fluid is starting to be entrained. In the high strength scenario, though, this terms acts as both a source and sink making the vorticity to be lost at almost the same rate that it is gained. This is especially evident in the regions where there are shearing in which normally additional vorticity would be generated through the Kelvin-Helmholtz instability, but in this case it is lost.

The final term of interest from the modified vorticity equation is the perturbation baroclinic term. The resulting evolution of this field can be viewed in Figure 4.23. Immediately, it becomes apparent that at high stratification, this term has very minimal effects and is the smallest term in this equations by an order of magnitude. This puts the perturbation baroclinic term at roughly the same scale as the dilatation term which agrees with the aforementioned scaling. Also in agreement with the theoretical scaling is the large relative magnitude of the low stratification strength perturbation baroclinic term. For low Mach numbers, this term is roughly half an order of magnitude smaller than the perturbation specific volume term. This means that even though the perturbation baroclinic term isn't solely responsible for the growth of the instability, it does still have a great impact on the evolution, especially when compared to the first two terms. It is of particular interest to note that in this case, the perturbation baroclinic term helps to add additional vorticity to the spike evolution but works to remove vorticity from the bubble. Thusly, the presence of this term in the low Mach number regime leads to this increased asymmetry in the late times, while the absence of this term in the high Mach number regimes leads to the growth to remain symmetrical.

Finally, we can apply this same analysis to the vortex pair simulations as well. For this analysis, we find similar results for the first two terms of the equation, meaning that they are a small enough order of magnitude that they can be neglected. The resulting fields for the effects of the perturbation specific volume and perturbation baroclinic terms can be viewed in Figure 4.24. It becomes immediately apparent that the perturbation baroclinic terms in these scenarios are also negligible, being 2 orders of magnitude less than the effects of the perturbation specific volume terms. The specific volume terms, though, still act as the major contributor to the evolution of the scenario. For the high stratification case, this term strictly acts as a sink, removing vorticity

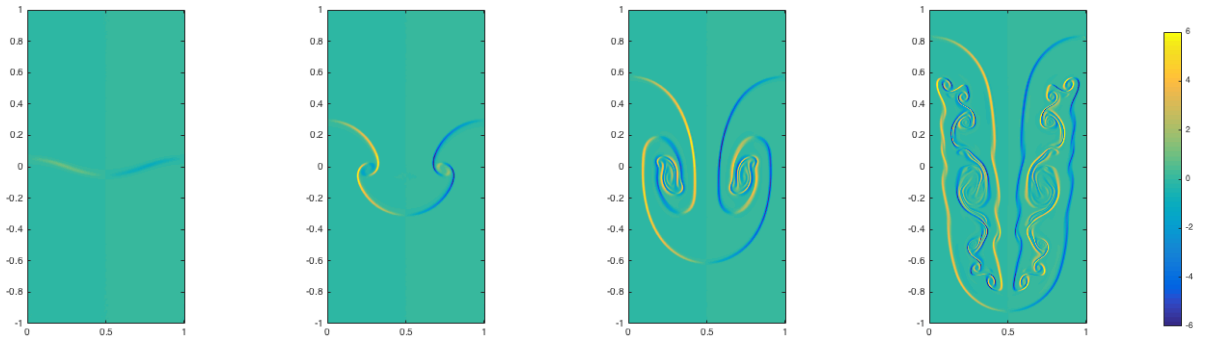

(a) M=0.3, t=5 (b) M=0.3, t=10 (c) M=0.3, t=15 (d) M=0.3, t=20

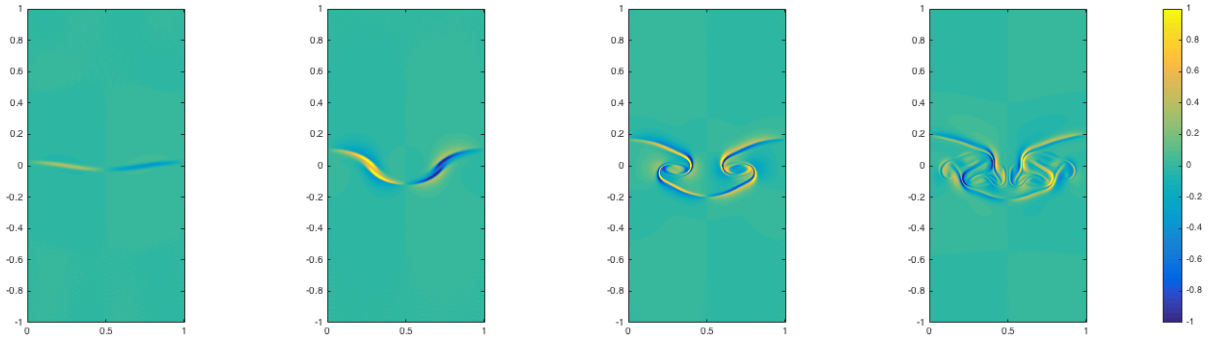

(e) M=1.2, t=5 (f) M=1.2, t=10 (g) M=1.2, t=15 (h) M=1.2, t=20

Figure 4.22: The evolution of the perturbation specific volume term as a function of time (left to right) and Mach number (top and bottom).

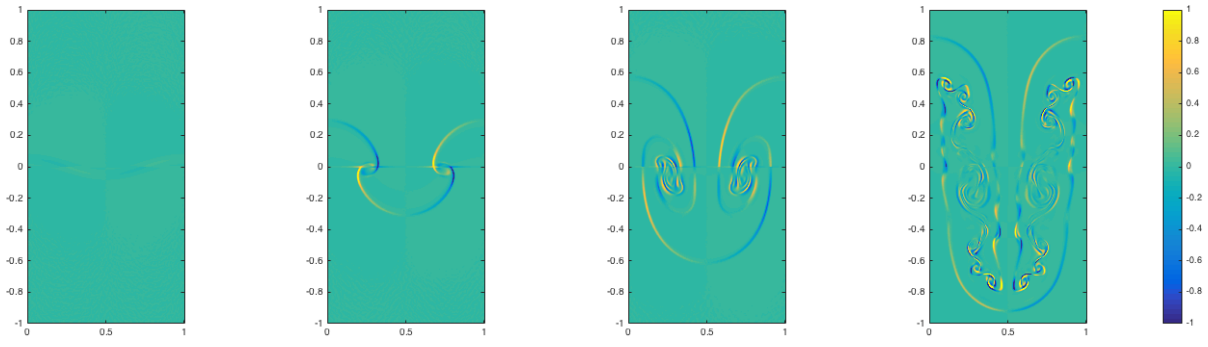

(a) M=0.3, t=5 (b) M=0.3, t=10 (c) M=0.3, t=15 (d) M=0.3, t=20

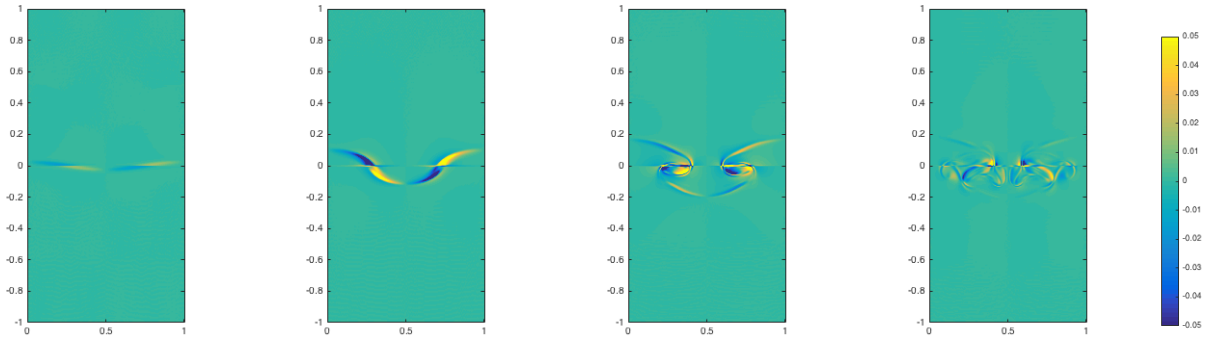

(e) M=1.2, t=5 (f) M=1.2, t=10 (g) M=1.2, t=15 (h) M=1.2, t=20

Figure 4.23: The evolution of the perturbation baroclinic term as a function of time (left to right) and Mach number (top and bottom).

from the core of the vortex pairs. For the low stratification, though, this interaction becomes more complex causing the addition of vorticity to the core while removing vorticity from the exteriors, essentially acting to compress the vorticies into smaller but more intense formations. Eventually, though, the removal of vorticity out-powers the addition and causes the vortex pairs to be completely destroyed. Both of these mechanisms also act on the RTI growth and contribute to the evolution of the instability, but their effects can be seen clearer through the vortex pairs.

4.5.4 Three Dimensional Effects

To fully explore this regime, three-dimensional simulations also need to carried out. Because of the expensive nature of large scale, three-dimensional, direct numerical simulations, only a few can be completed. In this case, it was chosen to explore the highest stratification to see if the complete suppressive effects still exist in the expanded dimension. The comparison of the growth of the two-dimensional M=1.2 case and the three-dimensional one can be seen below in Figure 4.25.

Though it is immediately clear that the two do not match perfectly, it is also clear that the two simulations exhibit very similar qualitative behavior. To further this similarity, we can explore the plots of their respective velocities over time in Figure 4.26.

In the end, both instabilities result in being completely suppressed and tend towards a zero velocity. The main difference is that in three dimensions, there is a larger source of potential energy to generate the initial vorticity field. This results in a higher strength field, and thusly a more steady velocity with a higher inertia. This greater inertia is then transferred into a greater distance that the instability is able to travel before being suppressed and results in a greater bounce back resulting in a greater magnitude negative velocity. In the end, though, both cases result in creating a mixing region that does not grow any larger.

4.6 Conclusions

Through this paper we have explored the effects of isothermal background stratifications on the growth of the Rayleigh-Taylor instability. The Parallel Adaptive Wavelet Collocation Method

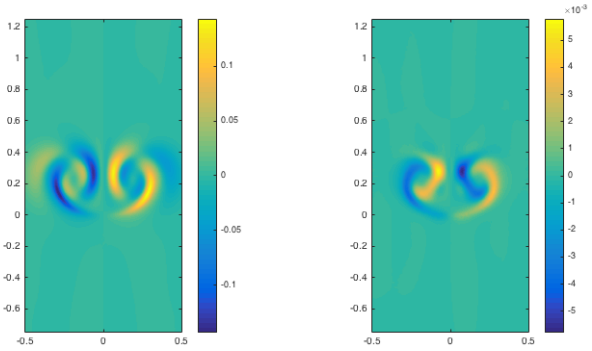

(a) The perturbation specific volume term for M=0.3

(b) The perturbation baroclinic term for M=0.3

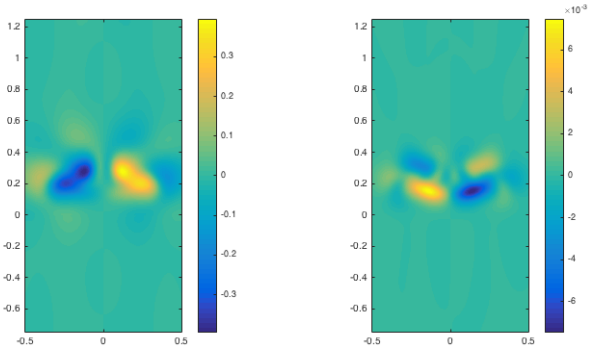

(c) The perturbation specific volume term for M=1.2

(d) The perturbation baroclinic term for M=1.2

Figure 4.24: The resulting fields for the last two terms of the modified vorticity equation for vortex pairs in the M=0.3 (top) and M=1.2 (bottom) stratifications.

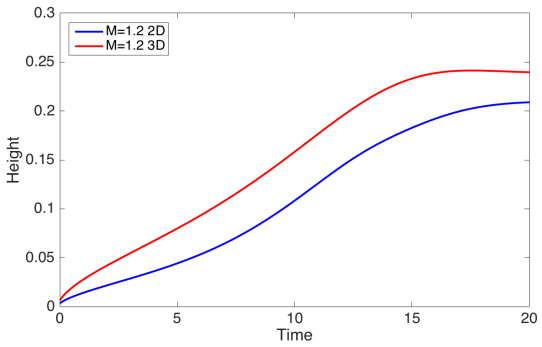

Figure 4.25: A comparison of the spike growth height for the 2 and 3 dimensional cases with the Mach number of 1.2.

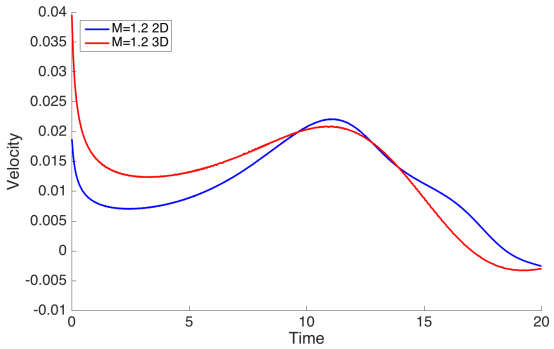

Figure 4.26: A comparison of the spike growth velocity for the 2 and 3 dimensional cases with the Mach number of 1.2.

was effectively applied and used to run high fidelity wavelet based direct numerical simulations in previously untouched regimes. Through this, it was discovered that isothermal background stratifications have a wide range of effects on the growth of RTI. Firstly, any stratification with a strength above the incompressible limit results in the complete suppression of the instability. Increasing the strength of the stratification causes the suppression of the instability to occur faster and results in a smaller mixing region. Secondly, it was found that even weak stratifications in the nearly incompressible limit have an affect on the growth, namely, it results in the exaggeration of the asymmetry between the bubble and spike growth in low Atwood number RTI. Finally, these interactions were confirmed to occur in both two and three dimensions.

In addition to the study of RTI, an exploration on the effects of background stratification on the development of other vortical fields was simultaneously carried out. Vortex pairs were allowed to traverse through the same stratified media as the RTI, and it was found that the suppressive effects of the stratification are caused by the destruction of these vortical structures. It has been found that through the analysis of the distance traveled by the vortex pairs, it is possible to predict the suppressive power on the RTI case, but when the near incompressible limit is reached, this predictive method is no longer valid.

Also, a new form of the vorticity equation was presented and studied for both of these cases. It was found that the dilatation term and the perturbation pressure term had minimal impact

on the growth of the instability and the evolution of the vortex pairs. For the RTI case, it was found that the perturbation specific volume term had the greatest impact on the growth and was responsible for both the addition of vorticity to low Mach number scenarios as well as the removal of vorticity and the eventual suppression in high Mach number cases. It was also found that for the RTI case, the perturbation baroclinic term was responsible for the asymmetry in the bubble and spike formations for low Mach numbers. For the vortex pairs, it was found that the same mechanism exacts itself through the perturbation specific volume term, but the perturbation baroclinic term was negligible. This confirms the idea that idea that the perturbation specific volume term is truly the term responsible for the growth and evolution of vorticity while in a background stratification.

Chapter 5

Effects of Stratification Type on the Single Mode Compressible Rayleigh Taylor Instability

5.1 Abstract

Wavelet-based direct numerical simulations of compressible, single-mode Rayleigh-Taylor instability (RTI) have been performed in order to study the effects of background stratification on instability development. Simulations have been performed for different strengths of the initial background stratification which is varied between the isothermal, isentropic, and isopycnic conditions. To understand the effects of the vorticity transport between the different stratifications, an analysis is performed using the vorticity equation. It has been found that background stratifications, regardless of strength or type (e.g., isothermal, isentropic, or isopycnic) generally increase the tendency towards asymmetry between bubble and spike growth, compared to the incompressible case with similar Atwood number. This effect is the largest for the isentropic stratification. The simulation with an isothermal background stratification quickly leads to complete suppression of RTI growth at moderate and high stratification strengths that is expressed through a decaying vortical field. The isentropic case causes an inhibition of the initial growth, followed by the continuous generation of vorticity which leads to an increased asymmetry between the bubble and spike. The isopycnic stratification has the least suppressive effect on the instability growth and, at higher strengths, it seems to even lead to accelerated growth along with the most vorticity generation. The analysis of the vorticity equation shows that this happens due to the interaction of the fluctuation of the specific volume field with the hydrostatic pressure field.

5.2 Introduction

Rayleigh-Taylor instability (RTI) arises when there is a mean density gradient in the direction opposite that of an acceleration. This acceleration can result from a gravitational force or the force from an accelerating front, and the RTI appears form the interaction of this acceleration with a perturbed interface at the density gradient[50, 59]. RTI can be observed in a huge range of systems, from large astrophysical flows to flows at the molecular level, and plays a large part in many engineering systems of interest such as inertial confinement fusion (ICF). A significant portion of these systems, including ICF[7], supernovae ignition fronts[31, 28, 8], x-ray bursts[39], and more, involve highly compressible fluid flow effects. Between the acoustic effects, material properties, and various stratifications, it becomes clear that there is not one single parameter that can capture the entirety of compressibility effects on the growth of the instability[43, 42]. As the instability continues growing into late times, the characteristics become more nonlinear, chaotic, and unpredictable. In short, little is known about these effects on RTI and there is a need to better understand them [43, 20].

Historically, the incompressible case has been the main subject of RTI studies[57, **?**]. Even in instances where a compressible solver has been used, simulations were carried out in the nearly incompressible regime and, in many cases, additional numerics were added to dampen out what few effects of compressibility are left[16]. In very rare cases, compressibility and background stratification effects have been examined, but none have been robust and complete in their analysis of different stratifications and strengths, leaving knowledge gaps and unanswered questions[20, 36]. This has led to the complete picture of compressibility effects on RTI growth not being well understood. Thusly, a full investigation using direct numerical simulation (DNS) is needed to uncover any previously unseen physics, and to develop better models so the cascade of energy from small scales to large can be completely captured.

In order to fully resolve all time and length scales associated with compressible RTI, the computational cost is quite high. Between the thin interfaces leading to high gradients, acoustic

waves, and even shock waves generated by RTI itself, a very high resolution is needed. In order to reach self-similar or asymptotic states, the simulations require domains that are much longer than the initial perturbation wavelength. Also, the nature of the stratification leads to a range of scales that spans many orders of magnitude in density, pressure, or temperature. In order to satisfy stability requirements, the time step must also be kept quite small. When all of these factors are brought together, it becomes clear that a complex and advanced computational method is needed in order to actually complete the simulations. To overcome this, the adaptive wavelet based DNS methodology originally presented in Reckinger **et al.**, [51, 52] will be used.

In this paper, we present an extension of our previous investigation into compressible RTI [65]. The past research was solely focused on the isothermal background stratifications, but in this paper we present the extension of this methodology to additional background stratifications, namely the isentropic and isopycnic cases, along with additional isothermal results. The focus continues to be on the low-Atwood number motivated by Wei and Livescu [64]. The main goal of this paper is to investigate the effects of varying both type and strength of background stratification on 2D RTI, along with developing a complete understanding of the vorticity transport that drives these mechanisms.

The rest of this paper discusses the following. First, Section 2 has a discussion of the problem setup and the various background stratifications that will be used in the simulations. It continues on to also presents the vorticity equation in the form that will be used to study the problem. Then, in Section 3, there is a brief discussion of the numerical method used to perform these simulations. Section 4 continues on to present the results of RTI simulations for all background stratifications. This is then followed with an analysis of the vorticity dynamics and transport that are responsible for the growth. Section 5 then finishes the paper with the conclusions.

5.3 Problem Setup

5.3.1 Governing Equations

RTI occurs when a heavier fluid rests on top of a lighter fluid, and the interface is perturbed all in the presence of an accelerative body force such as gravity. As the perturbation begins to grow, the heavy fluid falls into the light fluid to create spike-like structures as the light fluid rises to create bubble-like structures. Initially, if the perturbation amplitude is small, the growth is described by the linearized equations, but as the growth continues, it becomes more and more complex [50, 59]. In the early nonlinear stages, vorticity appears at the interface between the two fluids, and potential flow theory can be used to predict a stage of constant velocity growth. Due to the continuing addition of vorticity from the Kelvin-Helmholtz instability on the sides of the bubbles and spikes, the vorticity dynamics quickly become too complex to predict with a simplified model such as potential flow (i.e., the vorticity distribution cannot be understood from simple vortex sheets or point vortices)[43]. The interactions lead to a re-acceleration of the bubble/spike growth and late time chaotic development in the classical incompressible case [64]. How these regions are affected by compressibility and both stratification type and strength is not fully known. The complexity of the problem requires full DNS to be carried out in order to ensure the preservation of all physics in the flow and to truly capture the inverse cascade of energy that develops over time.

Simulations have been performed using the standard multi-species compressible fluid dynamics equations. The full system of equations is[43, 68]

$$\frac{\partial \rho}{\partial t} + \frac{\partial (\rho u_j)}{\partial x_j} = 0, \tag{5.1}$$

$$\frac{\partial (\rho u_i)}{\partial t} + \frac{\partial (\rho u_i u_j)}{\partial x_j} = -\frac{\partial p}{\partial x_i} - \rho g_i + \frac{\partial \tau_{ij}}{\partial x_j}, \tag{5.2}$$

$$\frac{\partial (\rho e)}{\partial t} + \frac{\partial (\rho e u_j)}{\partial x_j} = -\frac{\partial (p u_i)}{\partial x_i} - \rho u_i g_i + \frac{\partial (\tau_{ij} u_i)}{\partial x_j} - \frac{\partial q_j}{\partial x_j} + \frac{\partial c_{pl} T s_{jl}}{\partial x_j}, \tag{5.3}$$

$$\frac{\partial(\rho Y_l)}{\partial t} + \frac{\partial(\rho Y_l u_j)}{\partial x_j} = \frac{\partial s_{jl}}{\partial x_j}, \tag{5.4}$$

where ρ is density, p is pressure, T is temperature, u_i is the velocity in the x_i direction, Y_1 is the mass fraction for the bottom fluid, Y_2 is the mass fraction for the top fluid, R is the gas constant, and the ideal gas law $p = \rho RT$ is enforced. Repeated indices imply summation. The specific total energy is

$$e = \frac{1}{2} u_i u_i + c_p T - \frac{p}{\rho}, \tag{5.5}$$

the viscous stress is assumed to be Newtonian and is

$$\tau_{ij} = \mu \left(\frac{\partial u_i}{\partial x_j} + \frac{\partial u_j}{\partial x_i} - \frac{2}{3} \frac{\partial u_k}{\partial x_k} \delta_{ij} \right), \tag{5.6}$$

the heat flux is written as

$$q_j = -k \frac{\partial T}{\partial x_j}, \tag{5.7}$$

and the species mass flux is defined as

$$s_{jl} = \rho D \frac{\partial Y_l}{\partial x_j}. \tag{5.8}$$

To initialize the simulations, the first step is to set the upper fluid to occupy the space where x_1 is greater than 0, and the lower fluid to occupy the space where it is less than zero. This results in the interface being at $x_1 = 0$ where the species mass fraction is smoothed using the error function since it is the exact solution to the diffusion equation between the species. For RTI to be present, it is required that the density be greater in the upper fluid than in the lower fluid at the interface and that the molecular weight of the upper fluid is higher than the lower. The normalized difference between the two densities is typically measured by a non-dimensional parameter called the Atwood number. For the compressible case, the density is not uniform in the two fluids, and so to avoid additional complications due to thermodynamic effects, we uniquely define the Atwood number as

$$A = \frac{W_2 - W_1}{W_2 + W_1}. \tag{5.9}$$

where W_l denotes the molecular weight of the fluid l, with $W_1 < W_2$.

For this study, the majority of fluid properties were taken to be the same between the two species. This includes the dynamic viscosity, μ, the heat conduction coefficient, k, the mass diffusion coefficient, D, and the gravitational acceleration, g_i, which is taken to only act in the vertical, x_1, direction. Finally, the gas constants are found based on the molecular weights as

$$R_l = \mathcal{R}\frac{Y_l}{W_l}, \tag{5.10}$$

where $\mathcal{R}$ is the universal gas constant. Following from this, the mixture specific heat at constant pressure, c_p, is calculated as a mass weighted average as well (i.e., $c_p = c_{pl}\, Y_l$). The ratio between the specific heat, γ, is taken to be constant between the two fluids at 1.4.

Compressibility can be characterized by several parameters [42, 43]. Here, we are mainly concerned with flow compressibility. In this case, the corresponding incompressible limit can be obtained by increasing the speed of sound through increasing the background pressure (or temperature), such that the densities are not affected. The Mach number associated with this compressibility is defined as the ratio of the gravity wave speed, $\sqrt{g\lambda}$, and the isothermal speed of sound, $a_0 = \sqrt{P_I/\rho_I}$, at the interface. This gives the definition of M as

$$M = \sqrt{\frac{\rho_I g\lambda}{p_I}}, \tag{5.11}$$

where the subscript I implies "interfacial". The interface density, ρ_I, is found using

$$\rho_I = \frac{p_I}{\mathcal{R}T_I}\left(\frac{W_1 + W_2}{2}\right). \tag{5.12}$$

Since the background state needs to be in hydrostatic equilibrium away from the interface, the Mach number defined above also characterizes the background stratification. The simulations presented here have the same ρ_I, W_l (which fixes the Atwood number), perturbation wavelength λ, and g, so that varying M results in a change of P_I and, subsequently, T_I.

5.3.2 Initial Conditions

For this study, three different sets of stratifications were used to initialize the simulations, namely isothermal, isentropic, and isopycnic. For the isothermal stratification, the density and

pressure fields are

$$p(x_1) = p_I \exp\left(-\frac{g x_1}{R_l T_I}\right), \tag{5.13}$$

$$\rho(x_1) = \frac{P_I}{R_l T_I} \exp\left(-\frac{g x_1}{R_l T_I}\right), \tag{5.14}$$

where, in this case, T_I is not only the temperature for the interface, but is constant in the whole domain. For the isentropic case, the background stratification results from

$$p(x_1) = p_I \left(1 - \frac{\gamma - 1}{\gamma} \frac{g x_1}{R_l T_I}\right)^{\left(\frac{\gamma}{\gamma - 1}\right)}, \tag{5.15}$$

$$\rho(x_1) = \rho_l \left(1 - \frac{\gamma - 1}{\gamma} \frac{\rho_l g x_1}{p_I}\right)^{\left(\frac{1}{\gamma - 1}\right)}, \tag{5.16}$$

and the temperature field is set to satisfy the equation of state. Finally, for the isopycnic case, ρ is set to be constant above and below the interface and the pressure field is set as

$$p(x_1) = -\rho_l g x_1 + p_I, \tag{5.17}$$

where P_I is added to ensure the correct interface pressure and T is again set to satisfy the equation of state. An example of the different stratifications can be seen in Figure 6.1.

These equations can be non-dimensionalized and thusly written in therms of the Mach number and the Atwood number. By taking $\rho = \rho_I \rho^*$, $p = p_I p^*$, $x_1 = \lambda x_1^*$, and invoking that $\frac{R_I}{R_l} = 1 + (-1)^l A$, the procedure can be completed. The resulting non-dimensional form of equation 6.9 and 6.10 is

$$p_0^*(x_1^*) = \exp\left[-M^2(1 \mp A) x_1^*\right], \tag{5.18}$$

$$\rho_0^*(x_1^*) = (1 \mp A) \exp\left[-M^2(1 \mp A) x_1^*\right]. \tag{5.19}$$

Following the same procedure, the resulting forms for the isentropic case, i.e. equations 5.15 and 5.16, are

$$p_0^*(x_1^*) = \left[1 - \left(\frac{\gamma}{\gamma - 1}\right)(1 \mp A) M^2 x_1^*\right]^{\left(\frac{\gamma}{\gamma - 1}\right)}, \tag{5.20}$$

$$\rho_0^*(x_1^*) = (1 \mp A) \left[1 - \left(\frac{\gamma}{\gamma - 1}\right)(1 \mp A) M^2 x_1^*\right]^{\left(\frac{1}{\gamma - 1}\right)}. \tag{5.21}$$

Finally, applying this procedure to the isopycnic case results in 5.17 becoming

$$p_0^*(x_1^*) = 1 - (1 \mp A)\, M^2 x_1^* \,. \tag{5.22}$$

Essentially, using these three backgrounds states gives us one in exponential form, one in power law form, and one in linear form, allowing for a full comparison of the various states. The last step is to begin the RTI simulations by applying a small amplitude velocity perturbation directly at the interface and then carrying the simulation out from that state [52].

5.3.3 Vorticity Equation

The growth of RTI is driven by vorticity. Previously, a comparison had been made between RTI growth in a stratified media and the evolution of a vortex pair in the same media. An example of this comparison can be seen in Figure 5.2. This comparison lead to the ability to predict the height of the growth of the RTI before full suppression stopped the continued growth. It was found that this prediction capability was valid for isothermal background stratifications of $M \geq 0.6$ where the suppression occurred before any re-acceleration [65]. An attempt at a similar comparison was made for the isopycnic and isentropic background states and an example can be seen in Figure 5.3. In this Figure, the movement of the vortex pair in the isothermal background state is compared to the same vortex pair in an isentropic background state for two Mach numbers. It was found that the isentropic case caused some suppression at higher Mach numbers, but in all cases the vortex pair was able to travel until it met a wall. The vortex pair in the isopycnic case was suppressed even less, and thusly we cannot conclude any true results from the vortex pair comparison.

It can be noted, though, that this predicts an inherently different result for the two new background states. Namely, if the traversal of the vortex pair tells us anything, it is that vorticity is suppressed at a much lower rate for the isentropic and isopycnic stratifications. Based on this, it can be predicted that full suppression should not occur, but more importantly, a full analysis of the vortical fields generated must be completed in order to understand the dynamics of the problem. To begin, the non-dimensionalized 2-D vorticity equation is presented below, in which

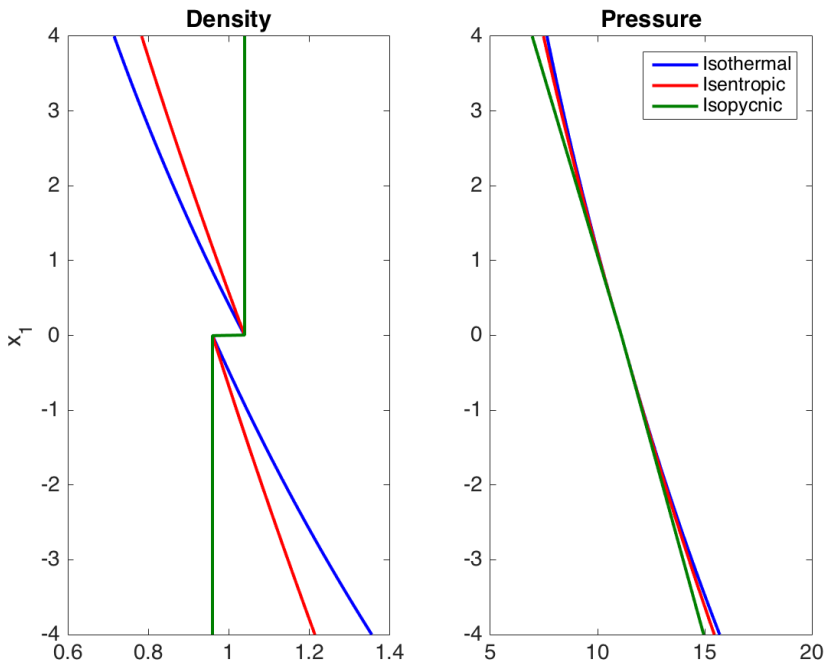

Figure 5.1: Density and pressure stratifications for $M = 0.3$ and $A = 0.04$ for the three different stratification types.

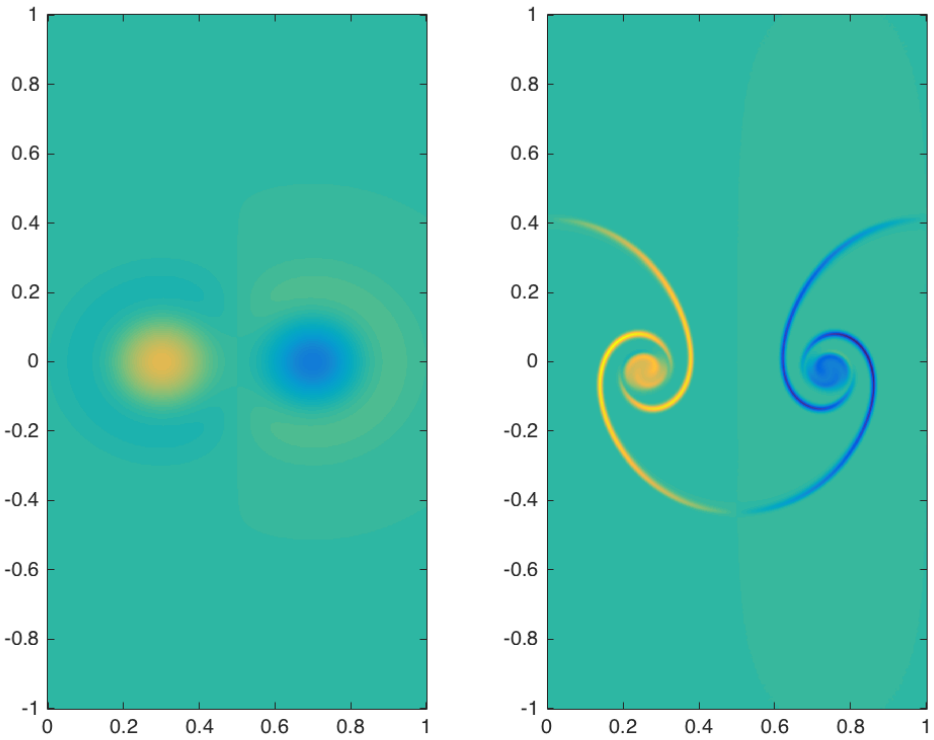

Figure 5.2: A comparison of the vorticity field generated by a vortex pair (left), and Rayleigh-Taylor instability (left).

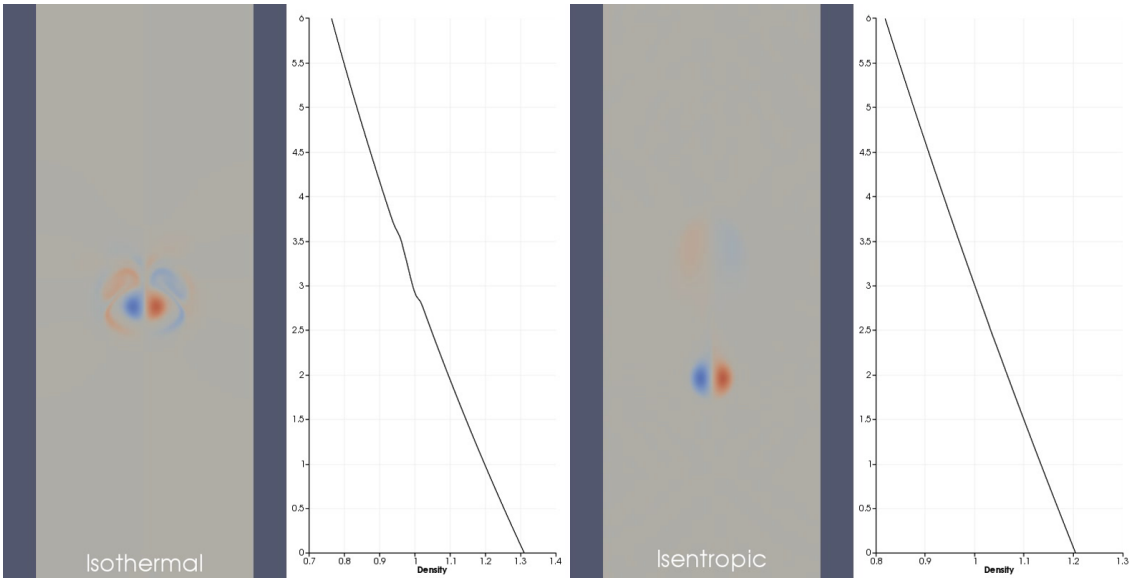

(a) M=0.3

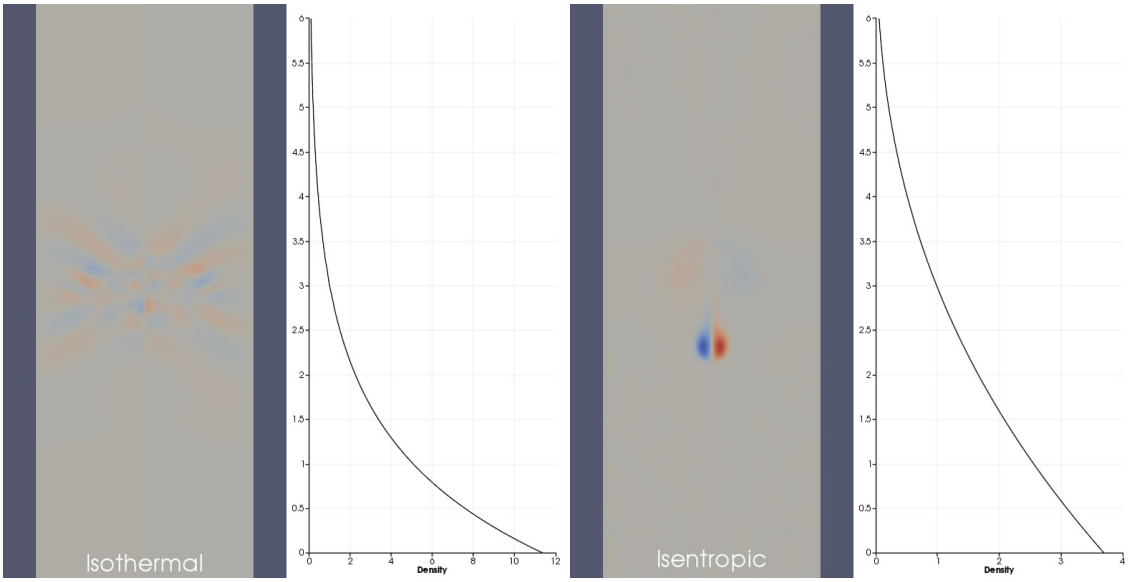

(b) M=0.9

Figure 5.3: A comparison of the vortex pair propagation through stratified media. On the left of each image are the results for the isothermal stratification, and the right shows the isentropic stratification results. The main representation is the vorticity field, and to the right of each vortical field is the resulting density along the centerline of the domain. The top image is for a Mach number of 0.3, and the bottom image for 0.9. Time is the same for all images.

the characteristic time scale has been taken to be $\sqrt{\lambda/g}$ [65].

$$\frac{D\omega_3^*}{Dt^*} = -\omega_3^* S_{kk}^* + \frac{1}{M^2}\frac{\epsilon_{3jk}}{\rho^{*2}}\frac{\partial \rho^*}{\partial x_j^*}\frac{\partial p^*}{\partial x_k^*} + \sqrt{\frac{A}{1+A}}\frac{1}{Re_p}D_j^*\,, \tag{5.23}$$

For convenience, a substitution can be made to replace ρ^* with the specific volume, v^*. The resulting equation becomes

$$\frac{D\omega_3^*}{Dt^*} = -\omega_3^* S_{kk}^* - \frac{\epsilon_{3jk}}{M^2}\frac{\partial v^*}{\partial x_j^*}\frac{\partial p^*}{\partial x_k^*} + \sqrt{\frac{A}{1+A}}\frac{1}{Re_p}D_j^*\,, \tag{5.24}$$

and we can then split v^* and p^* into the hydrostatic and fluctuating parts as

$$v^*(x_1,x_2,t) = v_0^*(x_1^*) + v'^*(x_1,x_2,t)\,, \quad p^*(x_1,x_2,t) = p_0^*(x_1^*) + p'^*(x_1,x_2,t)\,. \tag{5.25}$$

After completing this step, we are left with the final form of our non-dimensional vorticity equation shown below.

$$\frac{D\omega_3^*}{Dt^*} = -\omega_3^* S_{kk}^* + \frac{1}{M^2}\left[-\frac{\partial v_0^*}{\partial x_1^*}\frac{\partial p'^*}{\partial x_2^*} + \frac{\partial p_0^*}{\partial x_1^*}\frac{\partial v'^*}{\partial x_2^*}\right] - \frac{\epsilon_{3jk}}{M^2}\frac{\partial v'^*}{\partial x_j^*}\frac{\partial p'^*}{\partial x_k^*} + \sqrt{\frac{A}{1+A}}\frac{1}{Re_p}D_j^*\,. \tag{5.26}$$

In this equation, the first term encompasses dilatation effects, while the second term combines the effects of the initial hydrostatic specific volume interacting with the fluctuating or perturbation pressure. The third term accounts for the interaction of the background pressure with the perturbation specific volume, and the fourth accounts for the baroclinic generation due to the fluctuating terms. The fifth and final term, of course, accounts for the viscous dissipation. It is important to note that the derivatives of the hydrostatic terms can easily be found analytically by referring back to equations 6.14 through 5.22

5.4 Numerical Method

The compact spatial localization of RTI development, at least during the early stages of growth, naturally lends itself to using state-of-the-art adaptive grid methods. The nature of the instability means that it will require a very long domain so that the late time growth can be fully captured, but also a very small grid spacing is required so that sharp gradients along the interfaces are well resolved. However, within the majority of the simulation domain, there is no flow development occurring far away from the interface. As a result, high grid resolution is initially only needed in the center of the domain, and a coarse grid can be used elsewhere. In order to

minimize computational cost, a highly adaptive method is utilized so that high grid resolution is localized to only the areas in which there are important flow features present. It has already been successfully shown that wavelet-based methods work very well to accomplish exactly this task [51, 52].

The Parallel Adaptive Wavelet Collocation Method (PAWCM) adapts on physical features to take advantage of this localization. PAWCM utilizes the inherent properties of wavelets to adapt the grid to physical quantities in areas of high variation. This leads to PAWCM automatically being able to add more resolution to areas in which important flow physics are occurring. PAWCM is already parallelized, has adaptive mesh refinement, direct error control, arbitrary dynamic domain decompositions for load balancing, and a tree-like data structure for efficient message passing and data storage. Any of the extra computational cost added by the wavelet transformation is inherently made up for by the large amounts of compression in the grid for a localized system, such as the RTI problem examined here [61, 55, 47]. In the end, using PAWCM for the RTI problem allows the simulation to run using only about 1-10% of the effective grid resolution.

PAWCM essentially works by taking the wavelet transform of the flow field variable of interest. The resulting wavelet basis functions are localized in both wave number and physical space. From there, the adaptation and compression of the field happens through thresholding. Essentially, a threshold parameter, ϵ, is defined and coefficients greater than that parameter are kept while coefficients less than it are ignored. This results in the decomposition

$$u_{\geq}(x) = \sum_{k} c_k^0 \phi_k^0(x) + \sum_{j=0}^{\infty} \sum_{\mu=1}^{2^n-1} \sum_{\substack{l \\ |d_l^{\mu,j}| \geq \epsilon ||u||}} d_l^{\mu,j} \psi_l^{\mu,j}(x), \tag{5.27}$$

where u is a variable of interest, ϕ_k^0 represents the scaling functions on the coarsest level, $\psi_l^{\mu,j}$ represents the scaling interpolating functions on any arbitrary level, l and k represent physical grid points, and μ and j represent the wavelet family and level of resolution, respectively [61, 47].

As mentioned above, the wavelet thresholding technique results in any d below the threshold ϵ being effectively set to 0 and removed along with the wavelet it is associated with, resulting in the

removal of the grid point. It is in the regions of high variability that d is also high, and so in smooth regions, d is low with respect to the j level of resolution and is most likely deemed insignificant. In the end, this results in a reduced number of points with only these significant points remaining, while still maintaining an error that is of the order of ϵ. In addition to these significant points, in order to ensure accuracy in time stepping, the points adjacent to any significant point on the the same j level are also retained. Finally, finite differences are used to approximate derivatives with the addition of ghost points to ensure that the order of accuracy of the simulation is maintained. To do this finite differencing, second generation wavelets are used so that many different orders of accuracy are easily accessible [61, 47].

For boundary conditions, all of the faces besides the top and the bottom are taken as periodic. This allows for the symmetry of the simulation to be maintained while only needing to simulate a single wavelength. For the top and bottom of the domain, however, the boundary conditions are much more difficult. The hope is to maintain the illusion of a near-infinite domain, but due to the generation of pressure and shock waves from the application of the perturbation and the growth of the RTI, it must be ensured that there are little to no reflections of waves back into the domain, while also not affecting the background stratification. For this, the top and bottom boundary conditions have been set to shear-free slip boundaries with numerical diffusion buffer zones before them. This ensures that as a pressure wave is sent towards the top or bottom boundaries, the diffusion zone dissipates and dampens the wave causing there to be no need to fully resolve the wave as it hits the boundary. This approach also eliminates most of the wave energy before it can reflect. Any reflections that may be left over are weakened enough to have no consequence on the instability, and the domain is chosen to be large enough so that the instability does not reach these diffusion zones [52].

5.5 Results

A total of nine two-dimensional (2D) DNS simulations have been carried out for this investigation. These include the three stratification types (i.e., isothermal, isentropic, and isopycnic)

along with three stratification strengths for each (i.e., $M = 0.3, 0.6, \text{and } 0.9$). This selection of simulation parameters allows us to capture phenomena from the near-incompressible limit to high strength stratifications. Above $M = 1.0$, the isentropic and isopycnic case provides solutions that cause unphysical pressures before the domain is large enough to capture the entire flow without having boundary interactions. This results in limiting the stratification strengths we are able to simulate to below unity. It can be noted, however, that smaller domain simulations did show good agreement with the trends that will be presented below. For these simulations, the domain size is taken to be $[0, 1] \times [-4, +4]$ with the smallest allowed grid spacing to be $\frac{1}{2048}$. All of these simulations have been carried out for an Atwood number of 0.04, and a Reynolds perturbation number of 5,000 for this study. This Reynolds number is defined as

$$Re_p = \sqrt{\frac{Ag\lambda^3}{(1+A)\nu^2}}, \tag{5.28}$$

and is a measure of the potential of the perturbation growth to the viscous forces. It also sets the minimum vortex scales achievable on the mesh[64].

5.5.1 Isothermal Simulations

To begin with, an analysis is done on the isothermal simulations. A time series of the evolution for the various Mach numbers can be seen in Figure 5.4. As is expected, increasing the Mach number in this stratification quickly leads to the complete suppression of the instability's growth. This can be seen by looking at Figure 5.5. This figure shows the evolution of the bubble and spike tip height and velocity over time. The heights begin to approach an asymptote for the Mach numbers above 0.3, and the velocity of the tips begins decaying. As shown previously, Reynolds number has minimal impact on the growth of the instability in the isothermal stratification, so these results are in perfect agreement with what has come before.

To continue this investigation, though, and to enhance our understanding of the growth, an analysis of the vorticity must be completed. It is known that out of all of the terms in the vorticity equation presented in equation 5.26, only the third and fourth terms, namely the interaction of

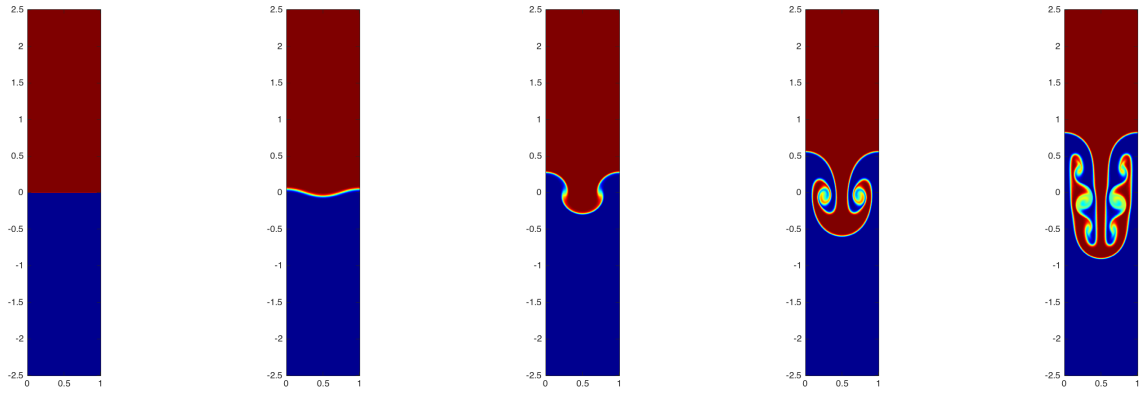

(a) M=0.3, t=0 (b) M=0.3, t=5 (c) M=0.3, t=10 (d) M=0.3, t=15 (e) M=0.3, t=20

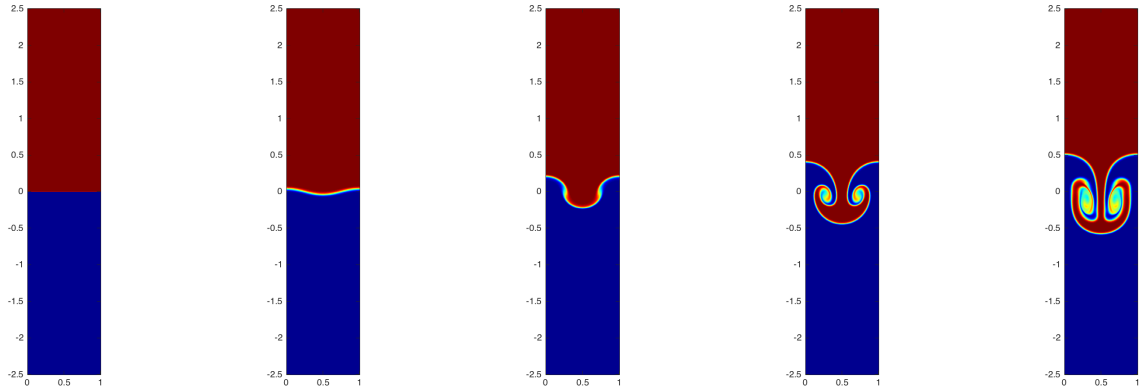

(f) M=0.6, t=0 (g) M=0.6, t=5 (h) M=0.6, t=10 (i) M=0.6, t=15 (j) M=0.6, t=20

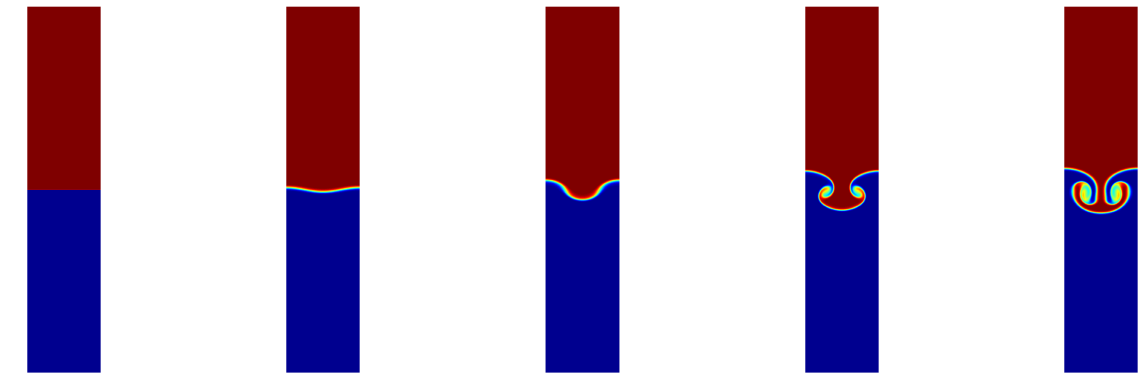

(k) M=0.9, t=0 (l) M=0.9, t=5 (m) M=0.9, t=10 (n) M=0.9, t=15 (o) M=0.9, t=20

Figure 5.4: RTI growth as a function of time (left to right) and Mach number (top to bottom) for the isothermal background stratification.

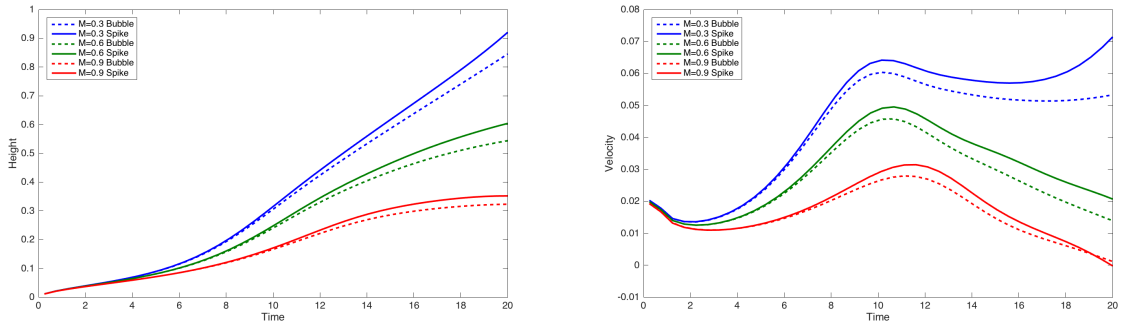

(a) Height

(b) Velocity

Figure 5.5: The growth of the height and corresponding velocities for both the bubble and spike for various Mach numbers in the isothermal stratification.

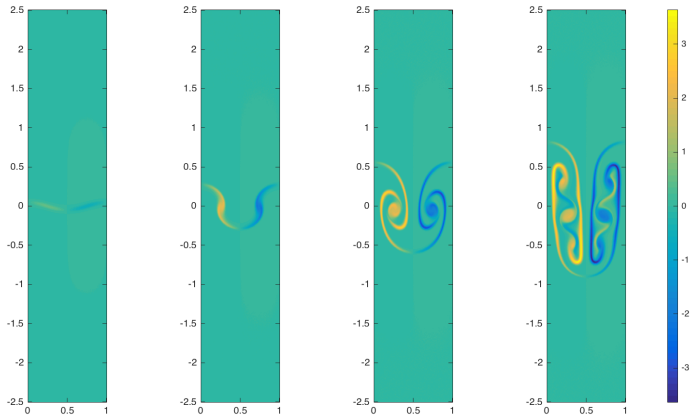

(a) t=5 (b) t=10 (c) t=15 (d) t=20

Figure 5.6: The evolution of vorticity plotted over time for the isothermal M=0.3 case.

the hydrostatic background pressure with the fluctuating specific volume and the perturbation baroclinic term, have a great impact on the vorticity generation and thusly the growth of the instability. Essentially, the fluctuating specific volume term is responsible for dictating the overall growth of the instability while the perturbation baroclinic term is responsible for the development of the asymmetry and is less present with increasing Mach numbers. An example of these terms is shown for $M = 0.3$ in Figures 5.6, 5.7, and 5.8. Notice that the fluctuating specific volume term is responsible for the transport of vorticity almost everywhere, whereas the perturbation baroclinic term adds additional vorticity to the spike while removing vorticity from the bubble.

Essentially, viewing these terms and the vortical structures themselves, shows that even in the lowest Mach number case, there is still significant removal of vorticity. For example, in the left half of the domain, the entire vortical field should be positive to keep the instability continuously growing, but the fluctuating specific volume term supplies a significant negative contribution that results in the removal of vorticity. This can be seen by viewing the average vorticity in that same half of the domain as shown in Figure 5.9. this figure shows that as opposed to a continuous addition and growth in vorticity, as is expected for RTI, the lowest Mach number reaches a peak

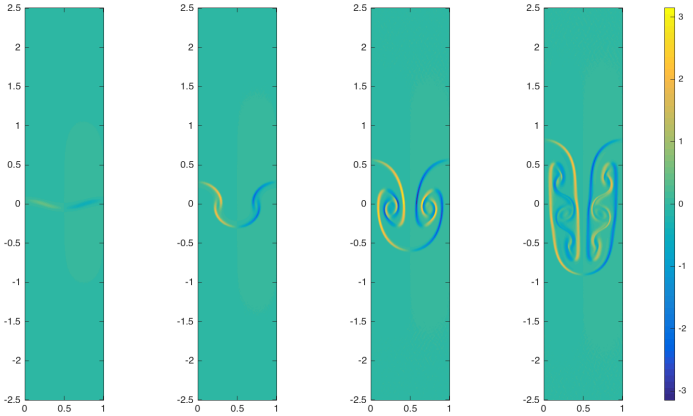

(a) t=5 (b) t=10 (c) t=15 (d) t=20

Figure 5.7: The evolution of the third term in the vorticity equation, i.e. the fluctuating specific volume term, over time for the isothermal M=0.3 case.

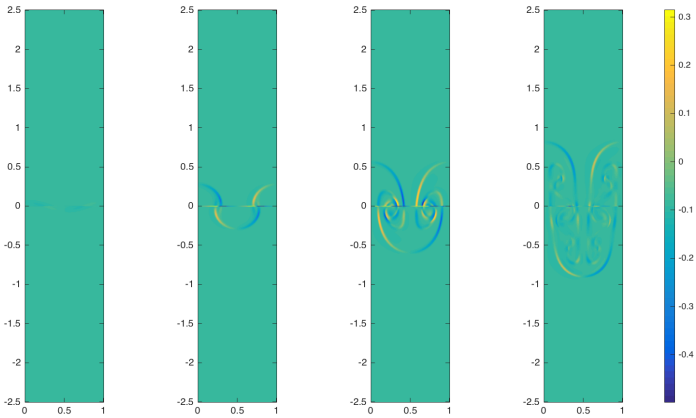

(a) t=5 (b) t=10 (c) t=15 (d) t=20

Figure 5.8: The evolution of the fourth term in the vorticity equation, i.e. the perturbation baroclinic term, over time for the isothermal M=0.3 case.

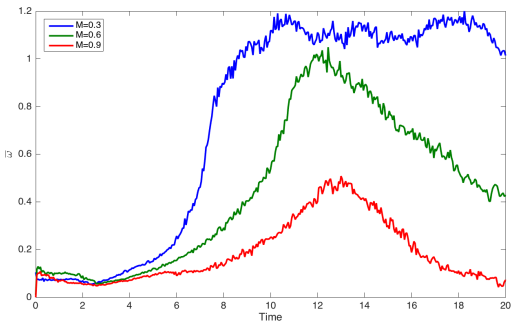

Figure 5.9: The evolution of the average vorticity over the left half of the domain. The lowest Mach number increases and then appears to asymptote, and may even start decaying. The higher Mach numbers all reach a peak vorticity and then begin to decay to a zero or negative quantity as the full suppression sets in.

vorticity and stays relatively constant whereas the other Mach numbers even begin to decay. This effect of the fluctuating specific volume term leads to the suppression of the instability and the corresponding decrease in the average vorticity that happens at greater rates with higher Mach numbers.

5.5.2 Isentropic Simulations

The isentropic simulations, though, tell a vastly different story. A quick glance at Figure 5.10 shows the growth and development of the instability over time for the various Mach numbers. One apparent trend is that in the initial times, the differences in the growth between Mach numbers is small. This becomes readily apparent by looking at the height of the bubble and spike tip over time in addition to the velocity of the same point. This can be viewed in Figure 5.11. This shows that the growth of the instability is relatively constant for the isentropic background state until approximately t=13. At this point, the background stratification starts affecting the growth, and while the bubble continues traveling at a nearly constant velocity, the spike starts accelerating rapidly. This acceleration of the spike along with the increase in asymmetry between the bubble and spike increases with the Mach number.

Similarly to before, to find the underlying cause of these dynamics, an analysis of the vorticity

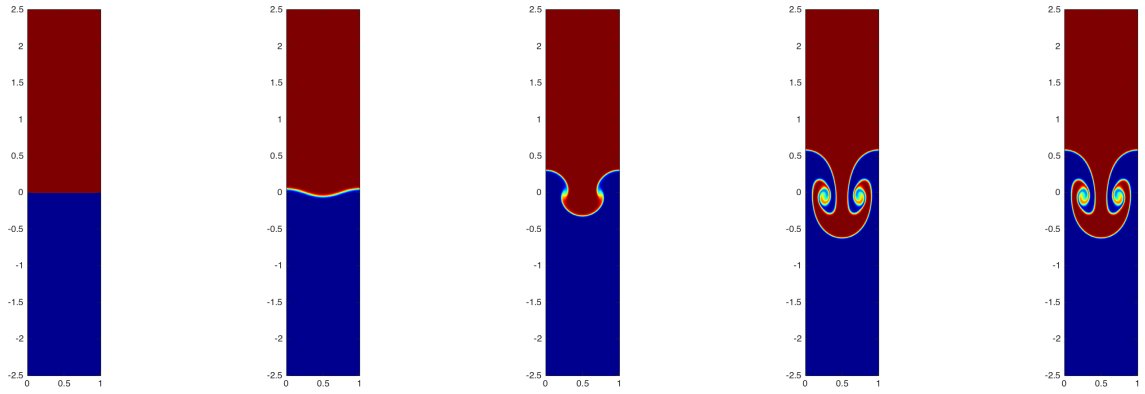

(a) M=0.3, t=0 (b) M=0.3, t=5 (c) M=0.3, t=10 (d) M=0.3, t=14 (e) M=0.3, t=14

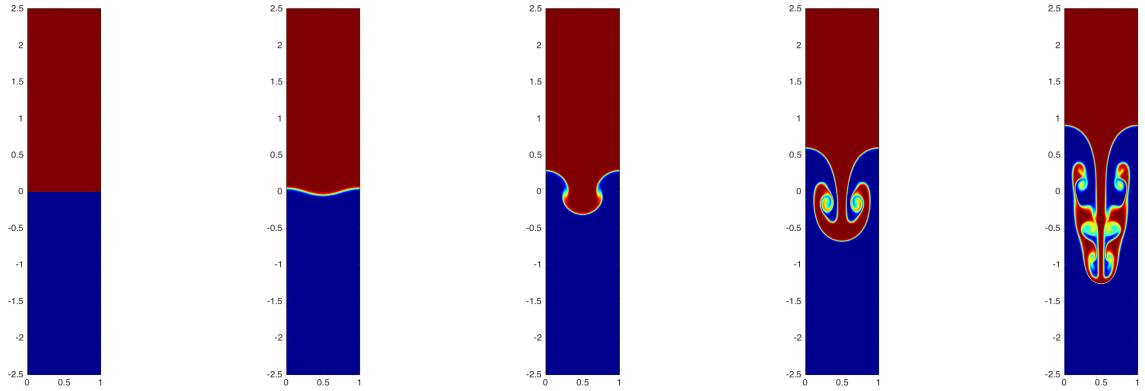

(f) M=0.6, t=0 (g) M=0.6, t=5 (h) M=0.6, t=10 (i) M=0.6, t=15 (j) M=0.6, t=20

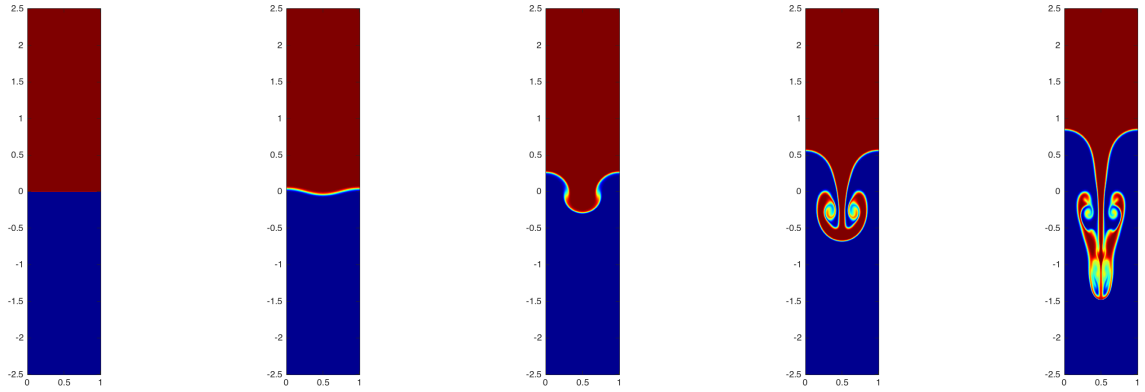

(k) M=0.9, t=0 (l) M=0.9, t=5 (m) M=0.9, t=10 (n) M=0.9, t=15 (o) M=0.9, t=20

Figure 5.10: RTI growth as a function of time (left to right) and Mach number (top to bottom) for the isentropic background stratification.

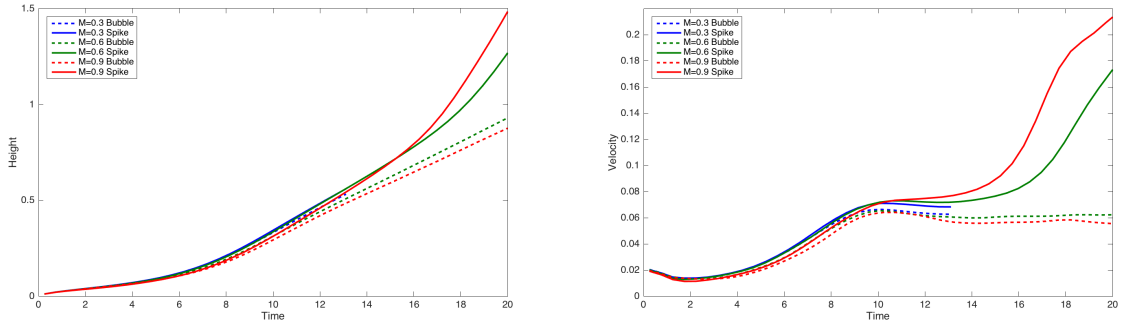

(a) Height

(b) Velocity

Figure 5.11: The growth of the height and corresponding velocities for both the bubble and spike for various Mach numbers in the isentropic stratification.

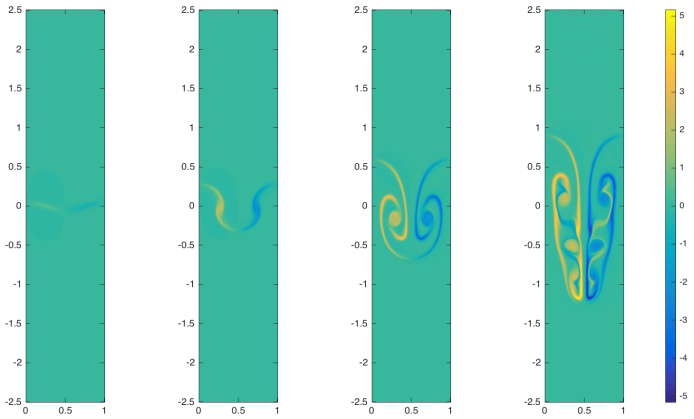

(a) t=5 (b) t=10 (c) t=15 (d) t=20

Figure 5.12: The evolution of vorticity plotted over time for the isentropic M=0.6 case.

must be completed. To start off, we can view a time series of the progression of the vorticity for the isentropic case. This progression can been seen for the M=0.6 case in Figure 5.12. From this figure, it is immediately apparent that the isentropic case has a larger magnitude of vorticity than the isothermal case. This also agrees with the fact that there is both an increase in the heights achieved by the bubbles and spike tips along with their corresponding velocities over the isothermal case. More evidence to support this enhanced growth over the isothermal case comes from the average vorticity plots shown in Figure 5.13, where we both have an increased magnitude and a constantly increasing field. The underlying reason for this, though, still lies hidden within equation 5.26.

In splitting apart the vortical fields into their respective components, an interesting phenomenon arises. Examples of the respective terms of the vortical fields for both the $M = 0.6$ and $M = 0.9$ cases are shown in Figure 5.14 and 5.15. In these figures the effects of the first, third, and fourth terms of the presented vorticity equation are shown. It was found that the second term, namely the fluctuating pressure term, was insignificant in comparison to the other terms. Essentially, doing this analysis showed that the evolution of the fluctuating specific volume term, the third term in the equation, followed a relatively similar development to the isothermal case, and

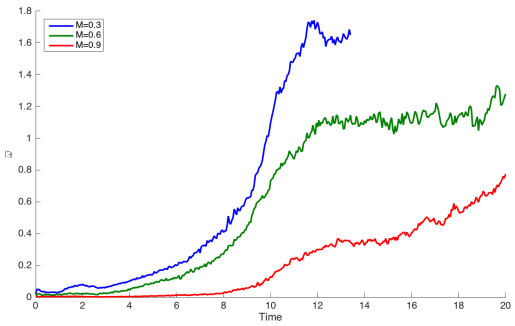

Figure 5.13: The evolution of the average vorticity over the left half of the domain for the isentropic case. It appears as though the generation of vorticity is constant and ever increasing resulting in a greater average than in the isothermal case.

is largely responsible for the growth of the vorticity in the field. However, it was found that both the dilatational effects and the perturbation baroclinic effects act on similar scales. Essentially, in the isentropic case, the dilatation term becomes significant. The dilatation term and the baroclinic term both affect the instability in a asymmetric way, adding vorticity at a greater rate and magnitude to the spike formation, and affecting the bubble much less. It was found that these terms only become significant at later times, when the asymmetry begins appearing, and the effects of these terms increases with increasing Mach number. In the end, the dilatation and baroclinic effects are responsible for trend in the asymmetry that can be seen in this case.

5.5.3 Isopycnic Simulations

The final background stratification to investigate is the isopycnic case. The evolution of the instability for all three Mach numbers can be seen in Figure 5.16 below. In this stratification, it is readily apparent that Mach number plays an inverse role as that in the isothermal case. As the Mach number is increased, the instability starts growing at a greatly increased rate. To put together an idea of the complete evolution of the problem, Figure 5.17 shows the evolution of the spike and bubble distance traveled and the corresponding velocities. It is very interesting to note, that in this case, very similar patterns arise compared to the isothermal, before they start departing from each other. By looking at the snapshots at t=15, it can be noted that the growth looks qualitatively

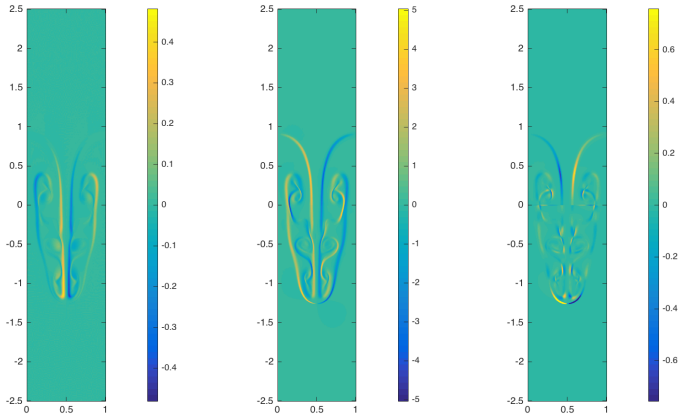

(a) Dilatation

(b) Fuctuation Specfic Volume

(c) Perturbation Baroclinic

Figure 5.14: The three important terms for the vortical evolution of the isentropic case with M=0.6 shown at t=20.

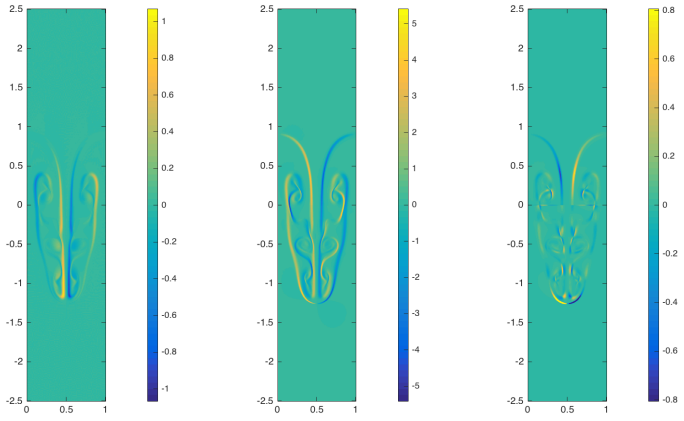

(a) Dilatation

(b) Fuctuation Specfic Volume

(c) Perturbation Baroclinic

Figure 5.15: The three important terms for the vortical evolution of the isentropic case with M=0.9 show at t=20.

similar to that of the isothermal case at M=0.3 at t=20. In comparing the distances traveled by the instability, they are all very similar having moved about 1λ away from the initial interface while also retaining close symmetry between the bubble and spike. After t=15 for the isopycnic case, though, the growth departs greatly.

It is important to note that the path departs greatly enough, that the M=0.9 case grows to a point in which the buffer zone of the boundary layer may play a part after roughly t=18, this is why this simulation is stopped here. To gather a more full understanding of the growth of this case, a similar vortical analysis has been completed as the previous scenarios. First, a comparison of the vortical fields at t=10 is shown below in Figure 5.18. It is interesting to see that at this time, the vortical fields are almost identical with a slight increase in the magnitude as the Mach number is increased. A fuller picture can be seen by viewing Figure 5.19 which shows that the average vorticity is very similar in the early times, but the higher Mach numbers have an increased vorticity at later times.

Of particular interest in this case, is the increased growth rate at the higher Mach numbers. The evolution of the vortical field for the highest Mach number, M=0.9, case can be viewed in Figure 5.20. This time series clearly shows the intense increase of the vorticity over time. Essentially, between t=10 and 18, the vorticity field increases by an order of magnitude! This intense increase in the vortical field is responsible for the increased growth rate and is unique to the isopycnic case. Using the vorticity equation, the reason behind this intense increase can be uncovered.

Similarly to the isothermal case, the dilatational field is an order of magnitude less than the rest of the terms and can therefore be ignored. Also for this case, the second term, namely the fluctuating pressure term, is analytically zero because the derivative of the initial hydrostatic background for the density is zero everywhere besides on the density jump itself, which should be ignored. The last two remaining terms, i.e. the fluctuating specific volume term, and the perturbation baroclinic term, are plotted in Figures 5.21 and 5.22, respectively. These figures show that as expected, the fluctuating specific volume term is largely responsible for the growth of the instability and its resulting vortical field. This can easily be seen by how well the vortical field and

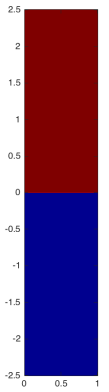

(a) M=0.3, t=0

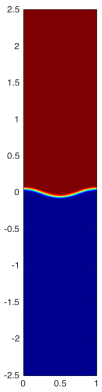

(b) M=0.3, t=5

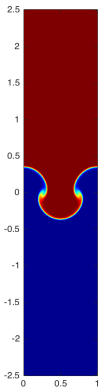

(c) M=0.3, t=10

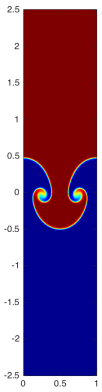

(d) M=0.3, t=11

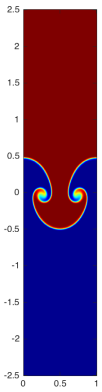

(e) M=0.3, t=11

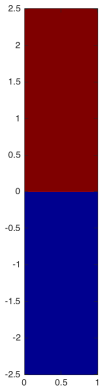

(f) M=0.6, t=0

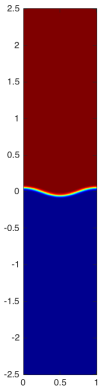

(g) M=0.6, t=5

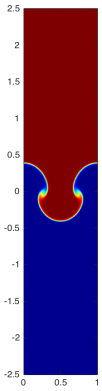

(h) M=0.6, t=10

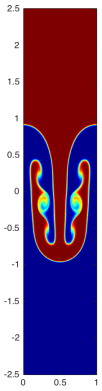

(i) M=0.6, t=15

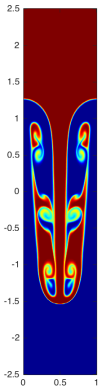

(j) M=0.6, t=17

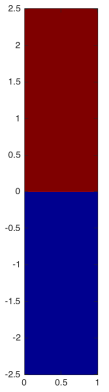

(k) M=0.9, t=0

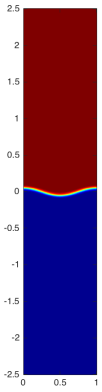

(l) M=0.9, t=5

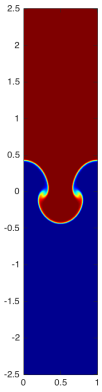

(m) M=0.9, t=10

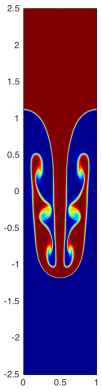

(n) M=0.9, t=15

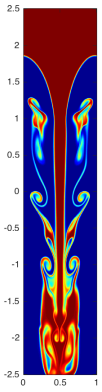

(o) M=0.9, t=18

Figure 5.16: RTI growth as a function of time (left to right) and Mach number (top to bottom) for the isotpycnic background stratification.

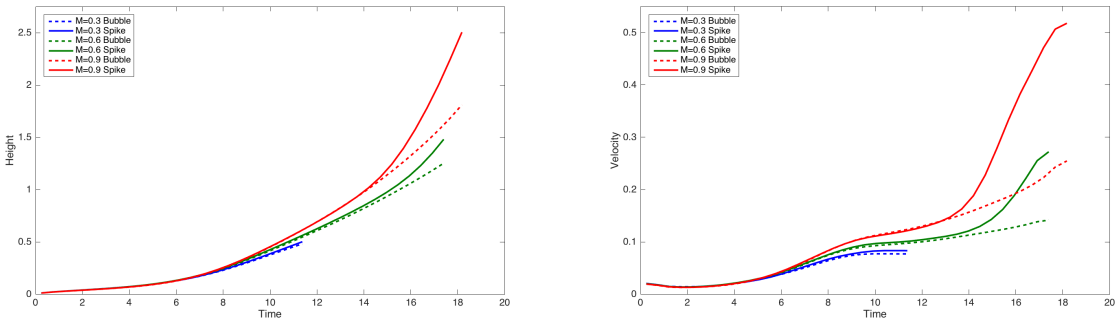

(a) Height (b) Velocity

Figure 5.17: The growth of the height and corresponding velocities for both the bubble and spike for various Mach numbers in the isopycnic stratification.

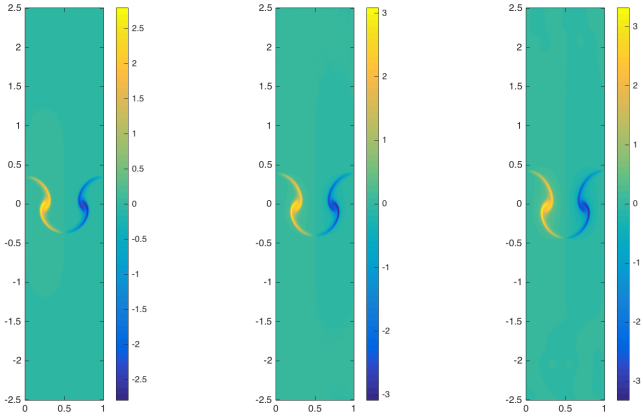

(a) M=0.3 (b) M=0.6 (c) M=0.9

Figure 5.18: A comparison of the vortical fields for the various Mach numbers at t=10 for the isopycnic case.

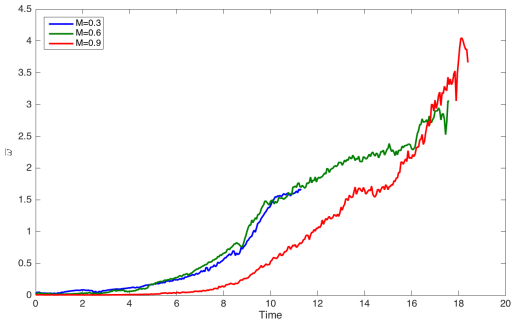

Figure 5.19: The evolution of the average vorticity over the left half of the domain for the isopycnic case. This shows how the average vortical development is nearly identical in the early times, but in the late times, the higher Mach numbers have an increased vorticity development.

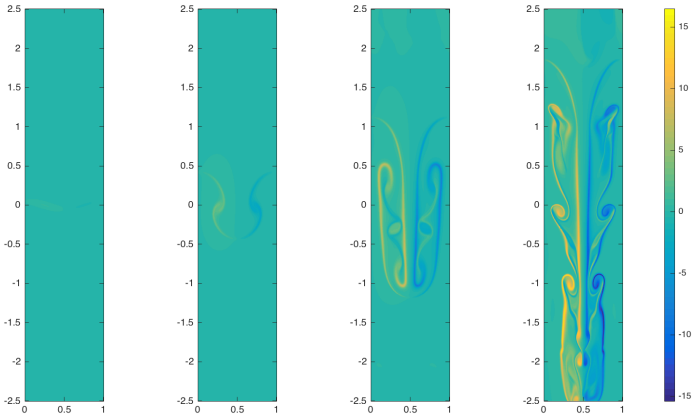

(a) t=5 (b) t=10 (c) t=15 (d) t=18

Figure 5.20: The evolution of vorticity plotted over time for the isopycnic M=0.9 case.

this term match. The most interesting result, though, is that for the baroclinic term. In this case, the baroclinic term is actually able to grow larger than the main generation of vorticity itself, but this term does not become significant until after t=10. The delayed effects of this term explain the onset of the late time asymmetry that develops in the isopycnic stratification and results in the spike growing at a much fast rate than the bubble.

5.6 Conclusions

Simulations of the Rayleigh Taylor instability have been carried out for isothermal, isentropic, and isopycnic background stratifications. Each stratification was tested at various strengths corresponding to isothermal Mach numbers of 0.3, 0.6, and 0.9. It was observed that the isothermal stratification leads to the full suppression of the instability for all but the weakest background stratification, but even the weakest background stratification is significantly suppressed in comparison to the growth with the other stratifications. The main mechanism for the growth in this case is derived from the vorticity generated by the effects of the interaction between the hydrostatic pressure and the fluctuating specific volume fields whereas the perturbation baroclinic term leads to a moderate increase in asymmetry for the low Mach number stratifications.

For the isentropic stratification, it was found that the initial growth is suppressed in a similar way with the isothermal stratification, but at late times there is an acceleration of the spike tips while the bubble maintains growth at a constant velocity. At higher Mach numbers, the growth is able to accelerate at an even faster rate and an increased asymmetry is experience between the bubble and spike. The growth overall is largely dictated by the same term as the isothermal case, but these unique effects are caused largely by the interaction of the dilatation field and the baroclinic term which causes a significant increase in the production of vorticity in the spike while affecting the bubble very little.

Finally, the isopycnic stratification was found to also lead to the initial suppression in the early growth stages, and then exhibit a similar trend to the isentropic case. As the instability is allowed to grow in the isopycnic scenario, a similar increase in both growth rate and asymmetry is

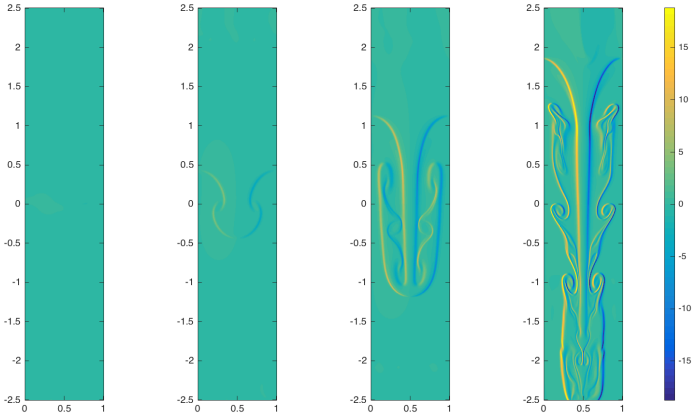

(a) t=5 (b) t=10 (c) t=15 (d) t=18

Figure 5.21: The evolution of the third term in the vorticity equation, i.e. the fluctuating specific volume term, over time for the isopycnic M=0.9 case.

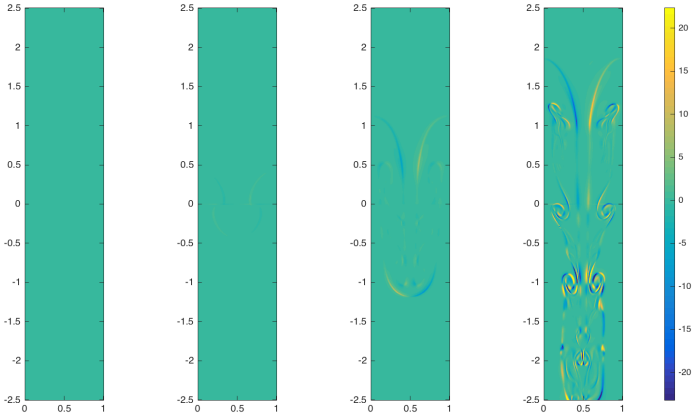

(a) t=5 (b) t=10 (c) t=15 (d) t=18

Figure 5.22: The evolution of the fourth term in the vorticity equation, i.e. the perturbation baroclinic term, over time for the isopycnic M=0.9 case.

exhibited as the isentropic case, but with the bubble also having a slightly accelerated growth. This case, however, grows at the fastest rate due to the intense generation of vorticity by the fluctuating specific volume term in the vorticity equation. Also, as the flow continues to progress the baroclinic term grows very large, even gaining a greater magnitude than the previously mentioned term. This large spike leads to the highly exaggerated asymmetry experienced in the late times of this case, and it increases along with an increasing Mach number.

Initially, predictions were made that both the isothermal and isentropic cases should not be fully suppressed based on the effects of the background stratification on the evolution of vortex pairs. These predictions appear to have been correct, and neither case shows any sign of the onset of full suppression. More extreme cases may exist, but this shows that the effects of the exponential background stratification exhibited by the isothermal case are unique. It is only through a strongly stratified state, such as an exponential growth, that a RTI can fully be suppressed, but by using other stratifications the growth can be modified and tuned to achieve the desired results.

Chapter 6

Effects of Stratification on the Multi-mode Compressible Rayleigh-Taylor Instability

6.1 Abstract

The multi-mode compressible and miscible Rayleigh-Taylor instability (RTI) is studied through the use of high resolution wavelet-based direct numerical simulations. Using classical methodologies, the most unstable mode is identified and used as the center of the perturbation wavelength spectrum. The simulations are carried out with an isothermal background state with varying strengths from M=0.3 (weakly stratified) to 0.9 (strongly stratified) at a Reynolds number of 5,000. It has been found that all background stratifications lead to the suppression of the instability and the transition to a decaying mixing regime. The width of this regime is determined based on the initial background stratification strength with weaker stratifications leading to wider mixing regions. This mixing is caused by the interaction of the hydrostatic pressure and the gradient of the fluctuations in the specific volume causing the generation of vorticity in the opposite direction as that needed to cause growth leading to a decay in the overall magnitude of vorticity. This leads to the smoothing of the initial density jump resulting in a completely stable mixing layer.

6.2 Introduction

Rayleigh-Taylor instability (RTI) is experienced in a two fluid system when there is a density jump between the two fluids in addition to an accelerative force that opposes this density gradient [50, 59]. This instability appears in a plethora of physical scenarios from cream mixing into coffee

all the way to supernova explosions. This wide range of scenarios makes the instability a vastly interesting choice of subjects to explore for there are a wide range of physics that can either be included or excluded based on the physical scenario of interest. Reactions, electromagnetics, miscibility, surface tension, compressibility, and thermal effects are just a few examples of the additional physics that could be chosen to be included [7, 31, 28, 8, 39]. The full effects of many of these forces and conditions are not completely understood, and the goal of this paper is to further the understanding of at least one: compressibility.

In order to gain a better understanding of the role of compressibility on RTI development, this paper completes a rigorous study on the effects of the background stratification that arises from satisfying the governing equations in a compressible fluid. Previously, the effects of the isothermal, isentropic, and isopycnic initial background stratifications on the single mode RTI were studied [65, 66, 67] but here, this analysis will be extended to the multi-mode regime, beginning with the isothermal background stratification. This will be done by studying the evolution of the RTI in different strengths of the background stratification achieved by varying the isothermal Mach number which essentially correlates to varying the static compressibility effects.

In RTI, the incompressible scenario has been well explored, but the fully compressible case has not. There have been a significant number of works devoted to understanding the linear regime of the compressible RTI, but few have been done to understand the nonlinear behavior and late time growth. Out of these that have been accomplished, many of them have chosen to use models such as large eddy simulations or Boussinesq approximations but without a truth case to compare to. Recently, Gauthier has presented a direct numerical simulation (DNS) investigation of the multi-mode fully compressible RTI at high Reynolds number (i.e. 6×10^4) with a very high stratification (approximately our isothermal Mach equivalent of 2.5) at an Atwood number of 0.25. He has found that the flow erases the density jump at the interface through turbulence bringing about the instability's suppression and ends with this same turbulence decaying within a stable stratification. The question still remains, though, in multi-mode compressible RTI, what effect do the stratification strength, Atwood number, and Reynolds number have on the growth of the

instability [20, 21, 46, 71, 63, 22, 30]?

In order to truly understand these effects, a model cannot be relied on to capture all of the physics, and also, RTI presents an interesting challenge in which small scale perturbations grow to drive the large scale mixing. Because of both of these, it is necessary to use DNS to resolve all of the scales of the flow in order to ensure that the proper physics is observed. Though this is the case, resolving all of the scales is quite a challenge because of the naturally occurring sharp gradients and the possible generation of both acoustic waves and shockwaves. If the instability grows unimpeded, the domains need to be much taller than they are wide to allow for this growth in addition to allowing the various waves to dissipate. This all leads to the cost of the simulations being quite high [64].

To overcome these costs, a highly adaptive wavelet based method, the Parallel Adaptive Wavelet Collocation Method (PAWCM), is used. PAWCM is a fully functional code capable of solving the entire set of compressible flow equations. By utilizing the natural localization of wavelets in both physical and wavenumber space, additional grid resolution is able to be generated in areas with complex dynamical effects (i.e. vorticity generation, density gradients, etc.). This additional resolution allows all of the scales to be resolved while still maintaining accuracy with little additional overhead. This method has been used multiple times before and has proven to work well for a highly localized problem such as this [51, 52, 65, 66].

In order to fully understand the evolution of the problem, a complete understanding of the evolution of vorticity must be achieved [64]. It has been shown that the vortical generation is responsible for the growth of the instability, and that the diminishing of this field is responsible for the suppression. Through the splitting of the pressure and density fields into their hydrostatic and fluctuating parts, we can investigate the vorticity production in a clear fashion. By analyzing this and the resulting mixing that occurs, a full picture of the development is achieved.

The rest of this paper is organized as follows. In the first section, a discussion of the governing equations, initial conditions, and the perturbation generation is presented. In the second section, a brief overview of AWCM is given. In section three, the results of the simulations, including an in

depth vorticity analysis, is done. Finally, the fourth and last section presents the conclusions from this paper.

6.3 Problem Setup

6.3.1 Governing Equations

Rayleigh-Taylor instability (RTI) occurs when a lighter fluids supports a heavy fluid in the presence of a gravity-like accelerative force. Any perturbations to the interface where the two fluids meet, results in the loss of the pseudo-stable configuration and the perturbations begin growing non-linearly resulting in the two fluids to begin mixing [50, 59]. First, they begin evolving according to linear perturbation theory, but it quickly evolves into a regime that is captured by potential flow models. After this, the instability begins growing non-linearly and it becomes difficult to predict the growth. The effects of compressibility are well understood for the early times, but this unpredictable late time growth is convoluted even more-so by the presence of compressibility effects [43]. In order to describe the motion of these fluids, the standard set of compressible, miscible, multi-species, and Newtonian fluid equations are used [43, 68]. This system of equations is

$$\frac{\partial \rho}{\partial t} + \frac{\partial (\rho u_j)}{\partial x_j} = 0, \tag{6.1}$$

$$\frac{\partial (\rho u_i)}{\partial t} + \frac{\partial (\rho u_i u_j)}{\partial x_j} = -\frac{\partial p}{\partial x_i} - \rho g_i + \frac{\partial \tau_{ij}}{\partial x_j}, \tag{6.2}$$

$$\frac{\partial (\rho e)}{\partial t} + \frac{\partial (\rho e u_j)}{\partial x_j} = -\frac{\partial (p u_i)}{\partial x_i} - \rho u_i g_i + \frac{\partial (\tau_{ij} u_i)}{\partial x_j} - \frac{\partial q_j}{\partial x_j} + \frac{\partial c_{pl} T s_{jl}}{\partial x_j}, \tag{6.3}$$

$$\frac{\partial (\rho Y_l)}{\partial t} + \frac{\partial (\rho Y_l u_j)}{\partial x_j} = \frac{\partial s_{jl}}{\partial x_j}, \tag{6.4}$$

where ρ is density, p is pressure, T is temperature, u_i is the velocity in the x_i direction, Y_1 is the mass fraction for the bottom fluid, Y_2 is the mass fraction for the top fluid, R is the gas constant,

and the ideal gas law $p = \rho RT$ is enforced. Repeated indices imply summation. The specific total energy is

$$e = \frac{1}{2}u_i u_i + c_p T - \frac{p}{\rho}, \tag{6.5}$$

the viscous stress is assumed to be Newtonian and is

$$\tau_{ij} = \mu\left(\frac{\partial u_i}{\partial x_j} + \frac{\partial u_j}{\partial x_i} - \frac{2}{3}\frac{\partial u_k}{\partial x_k}\delta_{ij}\right), \tag{6.6}$$

the heat flux is written as

$$q_j = -k\frac{\partial T}{\partial x_j}, \tag{6.7}$$

and the species mass flux is defined as

$$s_{jl} = \rho D\frac{\partial Y_l}{\partial x_j}, \tag{6.8}$$

where the dynamic viscosity is given by $\mu = \rho\nu$, k is the thermal conductivity, and D is the mass diffusivity. All of these are assumed to be constant and temperature independent in addition to being constant between the two fluids. Both the Prandtl and Schmidt numbers are taken to be unity.

6.3.2 Initial Conditions

In order to remain consistent with the governing equations and the ideal gas law while still being in an initially hydrostatic state, a background stratification must be used. In the initial study, it was chosen to minimize the effects resulting from being out of thermal equilibrium, so an isothermal background was chosen. The pressure, $p(x_1, x_2, t)$, and density, $\rho(x_1, x_2, t)$, fields arising from this state are

$$p_{0\alpha}(x_1) = p_I \exp\left(-\frac{g x_1}{R_\alpha T_0}\right), \tag{6.9}$$

$$\rho_{0\alpha}(x_1) = \frac{p_I}{R_\alpha T_0}\exp\left(-\frac{g x_1}{R_\alpha T_0}\right), \tag{6.10}$$

where p_I is the pressure at the interface. These states assume that the gravitational acceleration acts only in the negative x_1 direction (i.e., $g_i = -g\delta_{i1}$), and the interface between the two fluids

appears at $x_1 = 0$, with the heavy fluid, i.e. $\alpha = 2$, existing in the region where $x_1 > 0$ and the light fluid, i.e. $\alpha = 1$, in the region where $x_1 < 0$. In these equations, g is the magnitude of the gravitational acceleration, and the gas constant, $R_\alpha = \mathcal{R}/W_\alpha$,is based on the molar mass of fluid α. From these relations, the density at the interface is found by using the ideal gas law which results in $\rho_I = p_I/(R_I T_0)$ where $R_I = \mathcal{R}[(W_1 + W_2)/2]^{-1}$.

To study the effects of compressibility, there are multiple options that present themselves, namely either varying the ratio of heat capacities, γ, or by altering the interfacial pressure, P_I [42, 43]. In this present study, the most relevant incompressible limit is obtained by increasing this interface pressure. Using this assumption, we can create an isothermal Mach number by taking the ratio of the speed of a gravity wave to that of the isothermal speed of sound, $a_0 = \sqrt{P_I/\rho_I}$. In order to keep the background stratification the same as that in the single mode studies, the gravity wave speed used is based on a wave with wavelength equivalent to that of the domain. This results in an isothermal Mach number being defined as

$$M = \sqrt{\frac{\rho_I g L_{x_2}}{p_I}} \quad \Rightarrow \quad M^2 = \frac{g L_{x_2}}{R_I T_0}\,, \tag{6.11}$$

where L_{x_2} is the width of the domain in the x_2 direction.

To categorize the strength of the density difference at the interface, the Atwood number is defined as

$$A \equiv \frac{W_2 - W_1}{W_2 + W_1}\,. \tag{6.12}$$

In this W_α is the corresponding molecular weight of the respective fluid, and because $\alpha = 2$ is the heavier fluid, A will always be a positive number ranging from 0 to 1. Using a similar argument to the Mach number, we can define the Reynolds number based on the perturbation. Again, we can do this by using the width of the domain as our normalization factor to have a one to one comparison with that of the single mode case. This results in the definition as

$$Re_p \equiv \sqrt{\frac{A g L_{x_2}^3}{(1+A)\nu^2}} \quad \Rightarrow \quad \nu = \sqrt{\frac{A g L_{x_2}^3}{(1+A) Re_p^2}}\,. \tag{6.13}$$

Given all of these non-dimensional numbers, the initial states for p and ρ can also be non-dimensionalized to show their dependence on the Mach and Atwood numbers as shown above. The

resulting non-dimensional forms of equations 6.9 and 6.10 are

$$p_0^*(x_1^*) = \exp\left[-M^2(1 \mp A)x_1^*\right] , \tag{6.14}$$

$$\rho_0^*(x_1^*) = (1 \mp A)\exp\left[-M^2(1 \mp A)x_1^*\right] , \tag{6.15}$$

and examples of these stratifications can be seen in Figure 6.1.

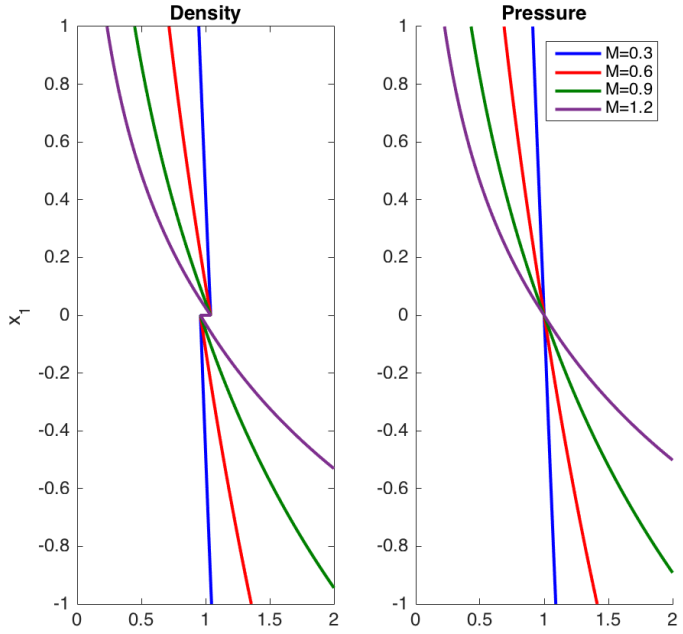

Figure 6.1: Density and pressure stratifications for $M = 0.3to1.2$ and $A = 0.04$.

After defining these initial conditions, there exists a complete and consistent pseudo-stable two fluid system with the lighter fluid supporting the heavier fluid. In order for the two fluids to begin mixing, a perturbation must be applied to the interface. In this present study, a multi-modal perturbation is applied. The process of generating this perturbation is based on the results found by Duff and Harlow. Using their methodology, the most unstable mode is found based on the viscous and dissipative effects. This is shown by finding dispersion curves for the growth factor as a function of both time and wavenumber. An example of one such series of curves is shown below in Figure 6.2 [17]. After finding this series of dispersion curves, the most unstable mode is

selected from the $t = 0.2$ curve since it accounts for the early diffusive phase, but will still supply the highest wavenumbers possible.

After selecting this mode, random amplitudes and phase shifts are found for a sufficient wavenumber space, and then a hat function is applied with the center at the found mode. The half-width of this hat function is kept at 10π to allow for an adequate range of modes to be applied while still keeping them relatively high frequency. Finally, all of the modes are forced to be periodic in the selected domain. An example of the resulting spectrum generated can be seen in Figure 6.3. The total perturbation is converted to a velocity perturbation on a mode by mode basis and then applied through a summation as follows

$$\dot{h}(y) = \Gamma \sum_{k=1}^{k_max} a_k \sin(2\pi k + \theta_k). \tag{6.16}$$

In this equation, k is the wavenumber, a_k is the corresponding amplitude, θ_k is the random phase shift and is limited to $0 \leq \theta_k \leq 2\pi$, and Γ is a parameter set to keep the energy constant between the single and multi-mode simulations.

6.4 Numerical Method

The combination of the need for highly resolved simulations with the inherent locality of the RTI leads these simulations to be the perfect setup for highly adaptive numerical methods. For this study, the Parallel Adaptive Wavelet Collocation Method (PAWCM) was chosen for exactly this reason, and has shown to work very well for this problem. Essentially, at all times, the flow fields of interest are localized to exist just around the interface of the two fluids. The area in which this interface exits is very small in comparison to the entirety of the domain, but the interface needs multiple points across it to resolve the flow. In order to have a large enough domain to account for the late time growth and wave dissipation would be prohibitively expensive. By using the adaptivity of PAWCM, though, the domains can both remain as large as needed and have enough resolution on the interface while still remaining comparatively inexpensive [51, 52].

The basis of how PAWCM works is the by transforming from physical to wavelet space.

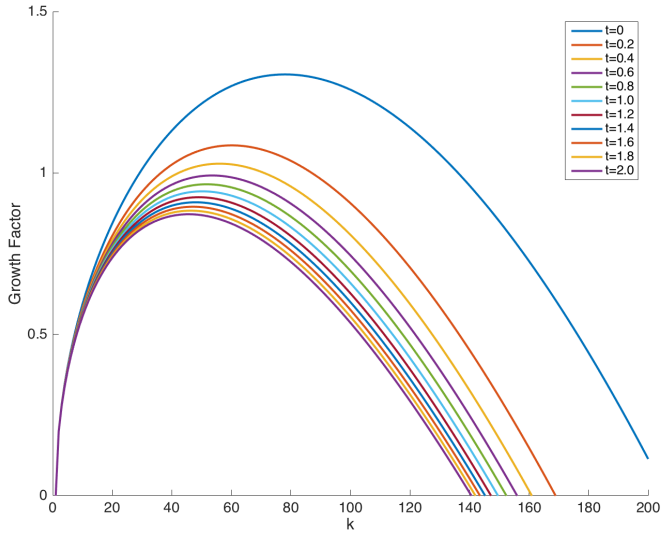

Figure 6.2: The growth factor as a function of both time and wavenumber after taking into account all of the interactions of viscosity and diffusion. This was found for $Re_p = 5,000$ and a Schmidt number of 1.

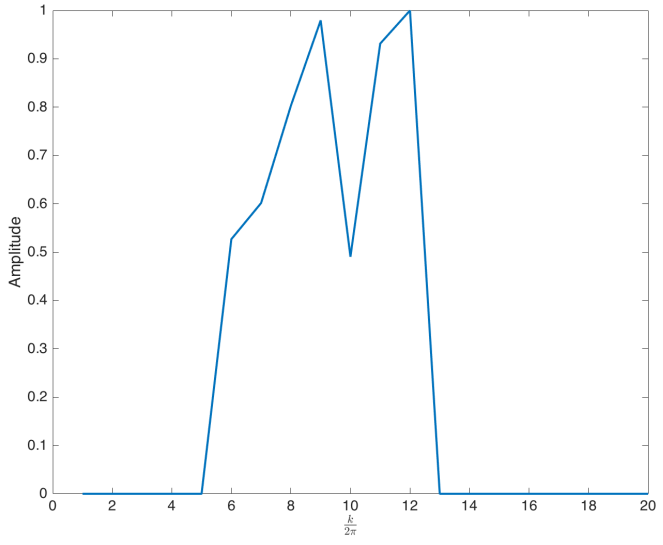

Figure 6.3: The resulting spectrum and its corresponding random amplitudes after applying the hat function to the wavenumber space.

This transform can be performed on any variable, whether it is conserved, part of the system that is solved, or is derived from other variables. The resulting description of the variable maintains locality in both physical and wavelet space. The resulting decomposition appears as follows

$$u_{\geq}(x) = \sum_{k} c_k^0 \phi_k^0(x) + \sum_{j=0}^{\infty} \sum_{\mu=1}^{2^n-1} \sum_{\substack{l \\ |d_l^{\mu,j}| \geq \epsilon ||u||}} d_l^{\mu,j} \psi_l^{\mu,j}(x), \tag{6.17}$$

where u is a variable of interest, ϕ_k^0 represents the scaling functions on the coarsest level, $\psi_l^{\mu,j}$ represents the scaling interpolating functions on any arbitrary level, l and k represent physical grid points, and μ and j represent the wavelet family and level of resolution, respectively. ϵ represents the thresholding parameter and serves as the function through which the adaptivity is achieved. Essentially, any coefficient d that is below the thresholding value, is set to 0 and this is equivalent to removing that grid point from the domain. [61, 55, 47].

The power of this method is that the magnitude of d relates directly to the variation of that particular variable for the grid point at that level of resolution, j. Essentially, d is large when the variation is large, and d is small when the variation is small. This means that if a quantity of interest is fluctuating largely, there will be many more coefficients that are large and thusly more points will be retained. On the other hand, if the quantity of interest is relatively constant the coefficients will be small, and not as many points will be kept because less will be needed to exactly represent the field. To fully generate the grid, a base number of points p needs to be chosen, and a maximum grid level of j, i.e. a j_{max} needs to be chosen. Based on this, the maximum resolution in any given direction is described as $2^{j_{max}-1} * p$. Finally, in addition to determining which points are kept and which are discarded, the thresholding parameter ϵ also acts as a direct source for error control of the problem. It can be shown mathematically that the error will be $\mathcal{O}(\epsilon)$ [61, 55, 47].

All of the sides of the domain are taken to be periodic, and the top and the bottom of the domain are set to shear-free slip boundaries with numerical diffusion buffer zones before them to dissipate any incoming waves to minimize reflections. The code solves the governing equations using fourth order finite differences in space and a third order total variation diminishing Runge-Kutta

scheme for time integration. The domain is decomposed arbitrarily at each time step using the Zoltan library in order to ensure the best load balancing during parallelization. When all of these features are taken into consideration, an ideal environment for simulating RTI is achieved and able to be executed in an efficient and highly parallel manner [52].

6.5 Results

6.5.1 RTI Simulations

The following simulations have been completed in a 2D domain that ranges from -4 to 4 in the x_1 direction and 0 to 1 in the x_2 direction. Re_p was taken to be 5,000 and the isothermal Mach numbers presented here are 0.3 and 0.9. The maximum resolution was the same for both directions and was taken to be $\frac{1}{2048}$. The initial results of the simulation can be seen below in Figures 6.4 and 6.5 where the mass fraction of the upper (heavy) fluid is visualized to show the progression of the instability. The same perturbation is applied to both background stratifications, and it can be seen that at least in the early times, the two simulations produce similar results. As time goes on, though, the two simulations appear to diverge. To fully investigate this, we can plot the maximum depth that the heavy fluid travels downwards as the max spike height, and the maximum height of the light fluid traveling upwards as the max bubble height. These results can be seen in Figure 6.6.

Essentially, the tracking of the height of these two fluids interpenetrating one another can gives us a general idea of what is happening in the fluid system. This plot shows that it is quite evident that after the early times, the $M = 0.9$ case is significantly more suppressed than the $M = 0.3$ case. The higher stratification results in the maximum height traveled to begin to asymptote and the velocities to continually decay towards zero. In the lower stratification case, though, the growth is still greatly suppressed in comparison to that of the single mode case, but it still is able to grow at a significantly higher rate than that of the higher stratification [65]. At this point, it appears as though both the bubble and spike are trending towards a relatively constant

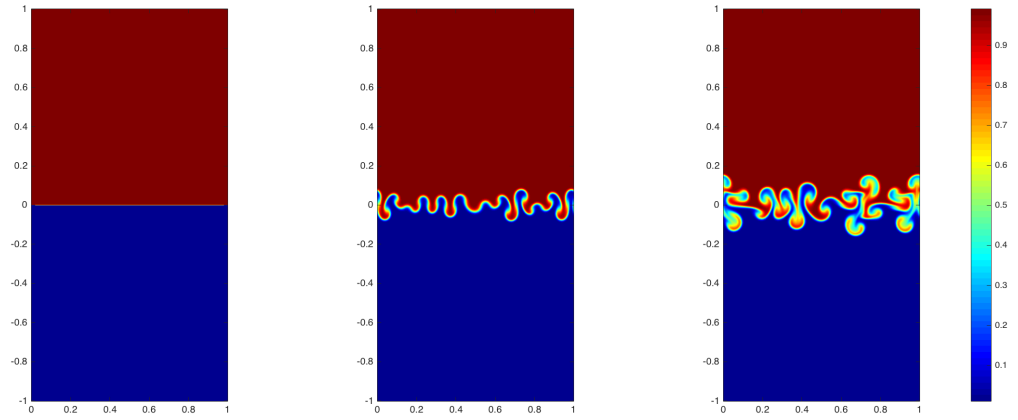

(a) t=0 (b) t=2 (c) t=4

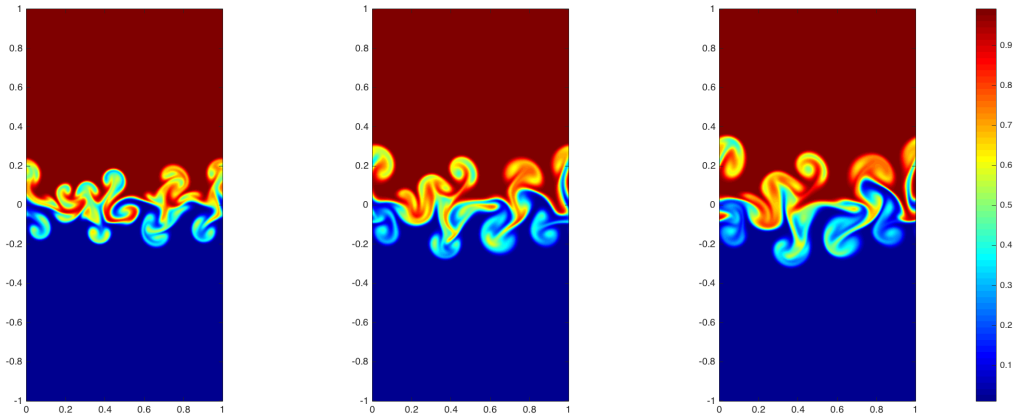

(d) t=6 (e) t=8 (f) t=10

Figure 6.4: The progression of the multi-mode Rayleigh-Taylor instability for M=0.3 and Re_p = 5000. This figure shows the mass fraction for the heavy fluid.

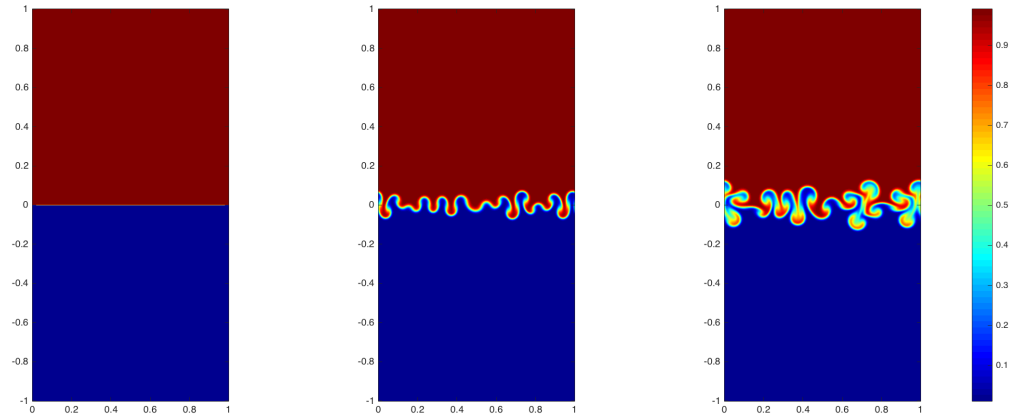

(a) t=0 (b) t=2 (c) t=4

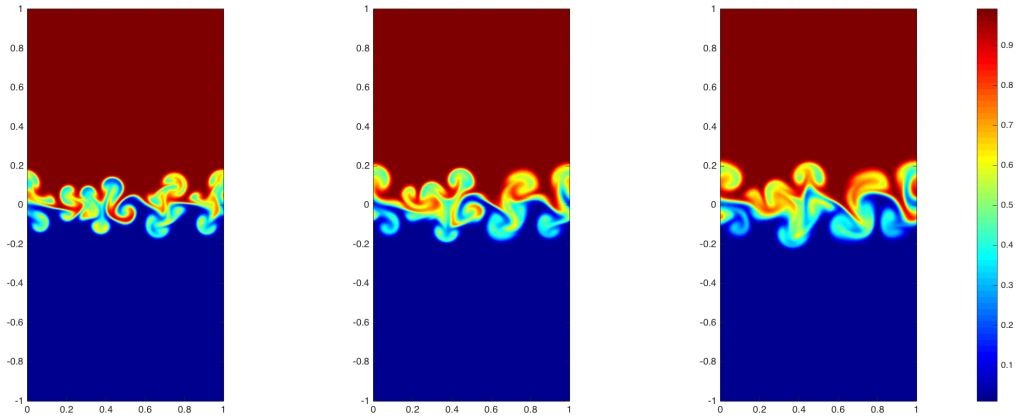

(d) t=6 (e) t=8 (f) t=10

Figure 6.5: The progression of the multi-mode Rayleigh-Taylor instability for M=0.9 and Re_p = 5000. This figure shows the mass fraction for the heavy fluid.

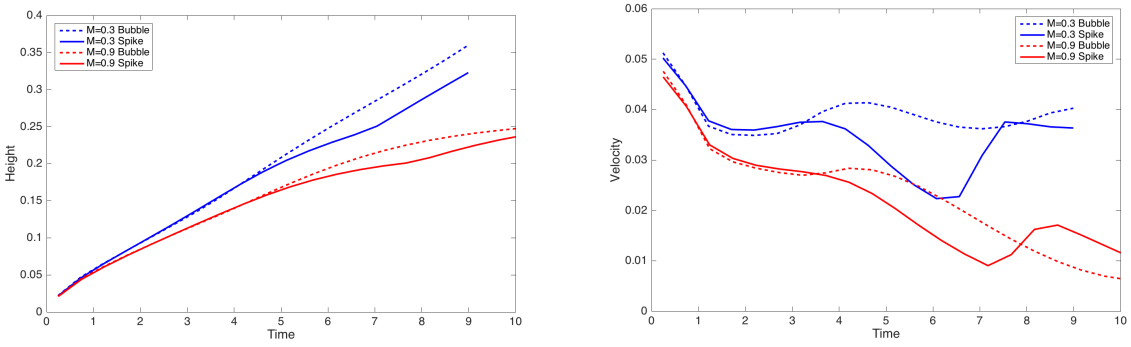

(a) Height (b) Velocity

Figure 6.6: That maximum distance traveled by the heavy and light fluid shown as the bubble and spike height, plotted in conjunction with the vertical velocities for both as well.

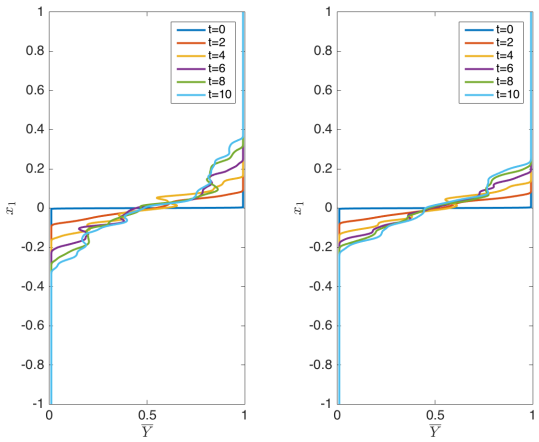

(a) M=0.3 (b) M=0.9

Figure 6.7: The average values of the mass fraction of the heavy fluid as a function of x_1 plotted at various times for both the M=0.3 (left) and M=0.9 (right) case.

velocity, but further investigation can enlighten the physics happening.

Since these simulations are multi-modal and thusly relatively chaotic in nature, it is difficult to understand everything that is happening by simply looking at the entire field. Because of this, and the fact that there are truly multiple different growth rates occurring, a more statistical approach is needed and can be achieved by either taking the average of the field in the x_2 direction or the RMS value in the same direction in relation to how that variable is best described[21]. This will leave us with averaged quantities that depends only on the x_1 direction and results in a better insight of the entire problem and its evolution. To begin with, Figure 6.7 shows the average of the Mass fraction plotted against x_1. Comparing these two plots, it is apparent that within their respective layers, both cases experience a similar amount of mixing, but the low stratification case is able to grow to a much further distance.

To better understand the mixing, though, a clearer picture can be obtained by looking at the average values of the density in the same fields. These results can be seen in Figure 6.8. This clearly shows that the two simulations are both mixing their densities in a way so that they are tending towards a stable stratification. In the case of the high Mach number stratification, by $t = 10$ the

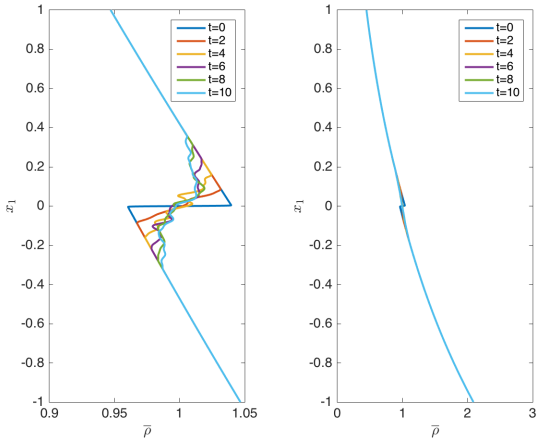

(a) M=0.3 (b) M=0.9

Figure 6.8: The average values of the density as a function of x_1 plotted at various times for both the M=0.3 (left) and M=0.9 (right) case.

mixed layer has washed out any sign of the initial density jump and the stratification has become uniform and stable leading to the nearly complete suppression of the instability. In the low Mach number case, the mixing region is working towards a stable and uniform mixture, but it still has more growth and mixing needed to accomplish this. This informs us that the growth should still continue at some rate.

The rate at which the growth of the instability occurs at can be measured by u or the velocity in the x_1 direction. At the same time, the rate of the mixing can be measured by the growth of the v velocity, i.e. the velocity in the x_2 direction. Essentially, for the instability to continue growing, u must also continue to grow to drive the vertical movement of the fluid, and in order for the two fluids to be exposed to each other for mixing, the v velocity must be present. The v velocity component increasing corresponds to an increase in mixing, but when it begins decaying it means that the instability has been fully suppressed and the decaying mixing regime has been reached [21]. A plot of the RMS values of the velocity components can be seen in 6.9 where it is observed that the high stratification case reaches a peak in u velocity very quickly, i.e. t=2, and begins decaying where the v velocity peaks much later, i.e. t=6, before it begins decaying. This

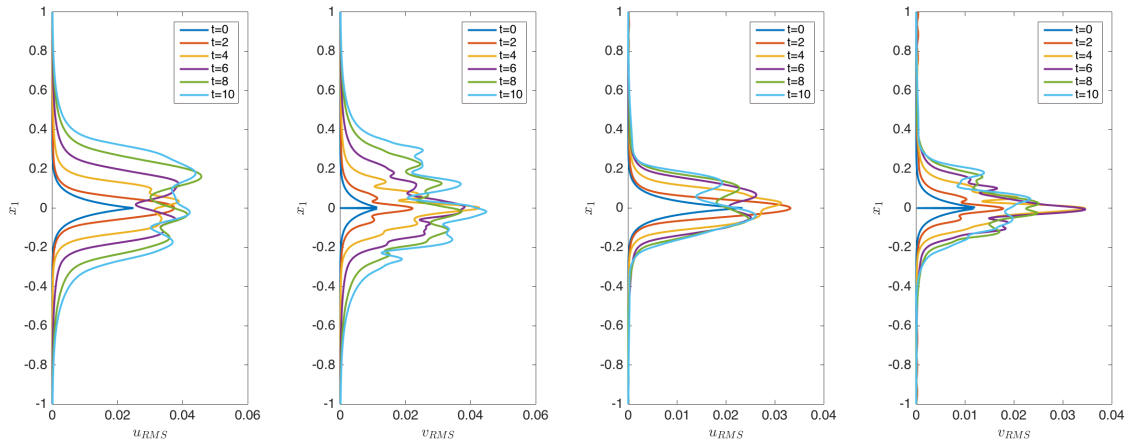

(a) M=0.3,u (b) M=0.3,v (c) M=0.9,u (d) M=0.9,v

Figure 6.9: The average values of the u and v components of velocity as a function of x_1 plotted at various times for both the M=0.3 (left) and M=0.9 (right) case.

shows the suppression of the growth of the instability, the transition to increased mixing, and then followed by the regime of decaying mixing. The low Mach number case, though, has not begun experiencing this full set of regimes yet. Both the u and v velocity have stagnated and stopped growing in overall magnitude, but continue to spread further in the domain. This implies that the suppression is starting to take place but has not completely stopped the growth of the instability yet.

It is also of interest to investigate the effects of the thermodynamic properties, i.e. the temperature and pressure. For these, the average pressure varies very little, so the fluctuating pressure, $p^{'}(x,y,t) = p(x,y,t) - p_0(x)$, is investigated. The variations in the temperature are significant enough that they can be detected in their base fields. The resulting averaged fields are presented in Figure 6.10. Essentially, as the Mach number is raised, the departures from the background states are larger in their magnitude, but the lower Mach number is able to achieve a larger area of influence caused by the larger mixing region.

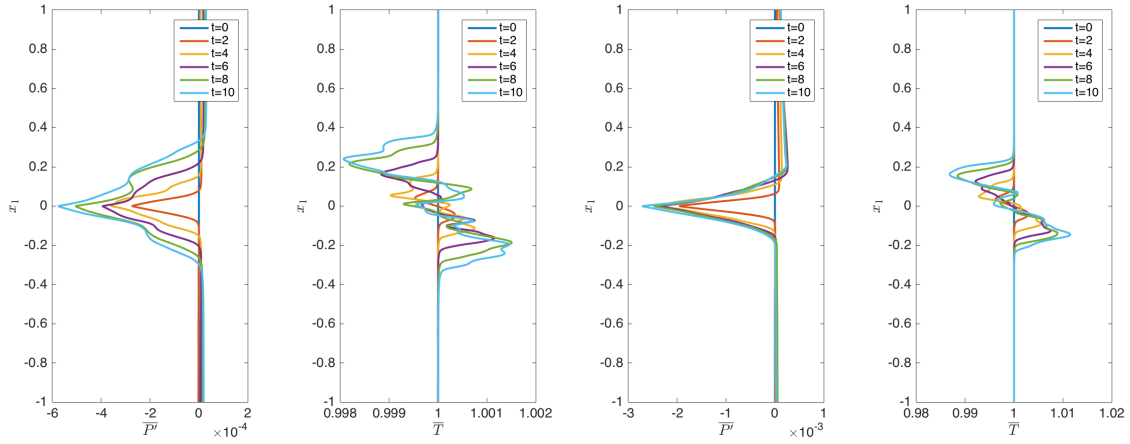

(a) M=0.3,$p^{'}$ (b) M=0.3,T (c) M=0.9,$p^{'}$ (d) M=0.9,T

Figure 6.10: The average values of the pressure fluctuations and the temperature as a function of x_1 plotted at various times for both the M=0.3 (left) and M=0.9 (right) case.

6.5.2 Vorticity Dynamics

Though we have explored many of the resulting effects arising from the multi-mode RTI in these configurations, a clear picture of the mechanism that causes the suppression and an indication as to when the suppression will occur is still lacking. In order to fully understand the underlying mechanisms that drive the instability growth, an analysis on the vortical fields must be completed. Firstly, the evolution of the vorticity for both the low and high stratifications can be viewed in Figures 6.11 and 6.12. As is expected, the vorticity fields for the low stratification are able to spread to a much larger area than that of the high stratification, but it is important to note that in both cases, the vorticity fields peak at the relatively early time around $t = 4$. After this peak, the vortical fields begin to decay, with the decay rate increasing with the Mach number. To fully see these effects, the average of the magnitude of vorticity in the entire field can be plotted as a function of time. The results for this are shown in 6.13. This confirms exactly what the time progression implied, i.e. the peak in vorticity occurs around $t = 4$ and the vorticity begins to decay. The high stratification case decays at a faster rate, but it is this decay in vorticity that causes the suppression observed in the growth.

In order to understand where this decay comes from, the various terms in the vorticity equation must be explored. For the single mode study, a new non-dimensional version of the 2D equation for ω_3 was presented [65]. The equation was

$$\frac{D\omega_3^*}{Dt^*} = \left[-\omega_3^* S_{kk}^* - (1 \mp A)\left(v_0^* \frac{\partial p'^*}{\partial x_2^*} + p_0^* \frac{\partial v'^*}{\partial x_2^*}\right)\right] - \frac{1}{M^2}\left[\epsilon_{3jk} \frac{\partial v'^*}{\partial x_j^*} \frac{\partial p'^*}{\partial x_k^*}\right] + \sqrt{\frac{A}{1+A}} \frac{1}{Re_p} D_3^*\,, \quad (6.18)$$

where v is the specific volume. This equation was derived by substituting the density for the specific volume and then splitting the specific volume and the pressure into their hydrostatic background states and their fluctuating parts, i.e.

$$v^*(x_1, x_2, t) = v_0^*(x_1^*) + v'^*(x_1, x_2, t)\,, \quad p^*(x_1, x_2, t) = p_0^*(x_1^*) + p'^*(x_1, x_2, t)\,. \quad (6.19)$$

In doing this derivation, the only change is in the non-dimensionalization of the problem replacing the wavelength of the perturbation, λ with the domain width, L_{x_2}. This adjustment has already

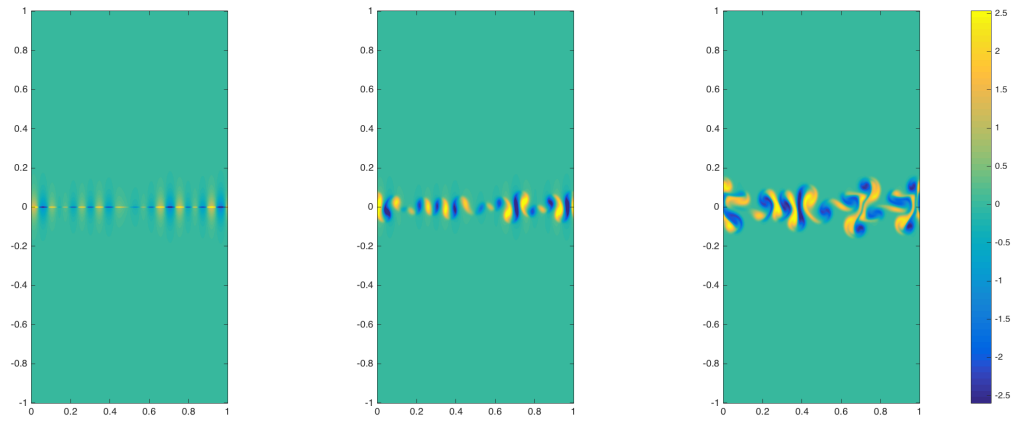

(a) t=0 (b) t=2 (c) t=4

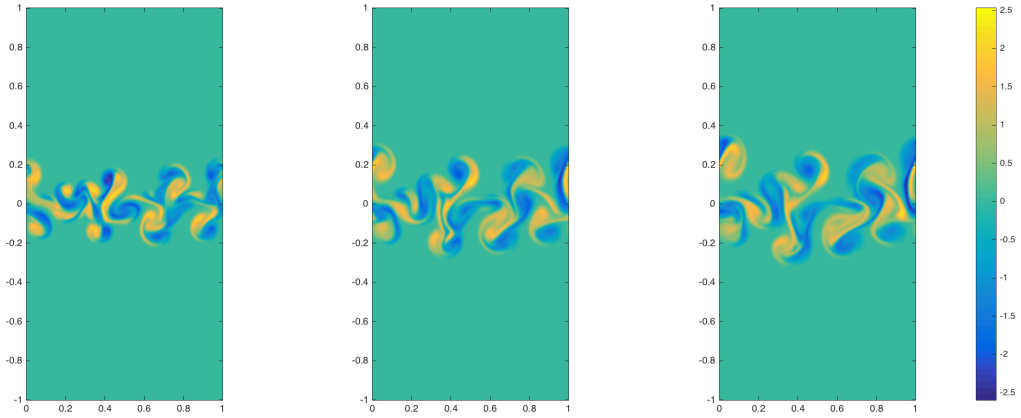

(d) t=6 (e) t=8 (f) t=10

Figure 6.11: The evolution of the vorticity field for the M=0.3 case over time.

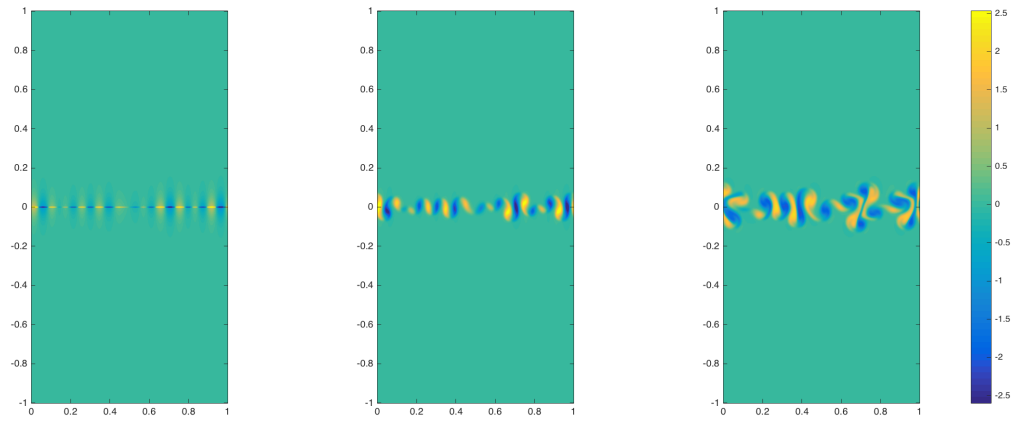

(a) t=0 (b) t=2 (c) t=4

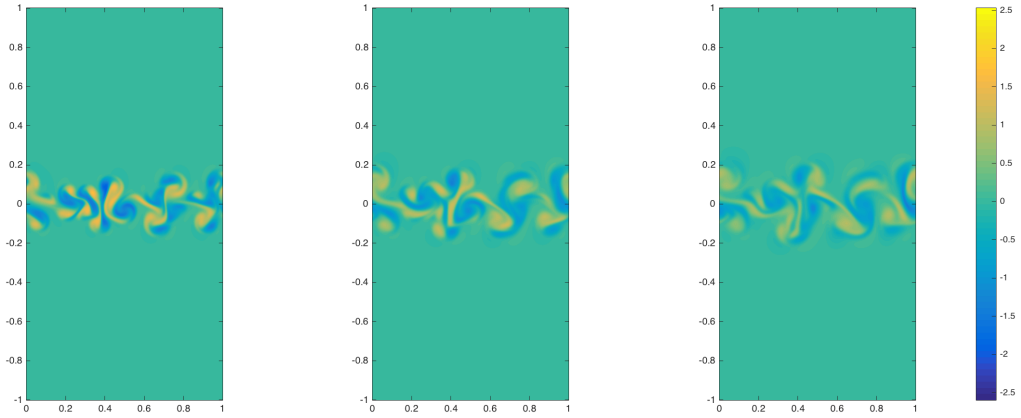

(d) t=6 (e) t=8 (f) t=10

Figure 6.12: The evolution of the vorticity field for the M=0.9 case over time.

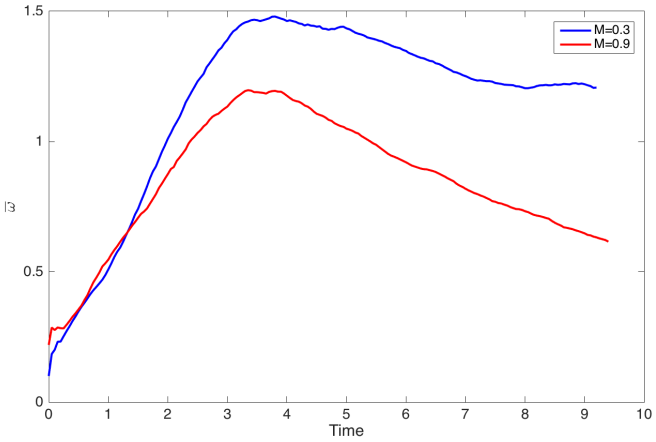

Figure 6.13: The average of the magnitude of vorticity in the entirety of the domain plotted as a function of time for both the $M = 0.3$ (blue) and $M = 0.9$ (red) cases.

been accounted for in the definition of M and Re_p and thusly the equation works out to be identical.

In investigating this equation previously, it was shown that the first and second terms were very small scale and had little impact on the growth of the instability, whereas the third term accounted for the majority of the growth, and the fourth term accounted for the asymmetry in the bubble and spike evolution. Doing a similar investigation into the orders of magnitude that these terms present results in the knowledge that the third term, namely the interaction between the hydrostatic pressure and the fluctuating specific volume, is at least 1.5 orders of magnitude larger than the other terms. In Figure 6.14 each of these terms is plotted for the $M = 0.3$ case at a $t = 4$, and through this basic view, it becomes quite clear that the fluctuating specific volume term dominates with the sum of the other terms accounting for at most 5% of the vorticity transport. The results for the high stratification case are nearly identical, and for this reason, the rest of the analysis will focus just on the third term.

Since the fluctuating specific volume term is the most important for the vorticity transport it is imperative that we understand it completely. First, a plot of the development of this term for $M = 0.3$ and $M = 0.9$ is presented in Figures 6.15 and 6.16, respectively. It can be seen that in both cases the peak in this term happens in the early stages of growth, around $t = 2$. From there both of the stratifications show a decay in the field, meaning that the vorticity is also decaying. To further explore this, the RMS value of this term over time as a function of x_1 has been plotted in Figure 6.17 along with similar plots for the vorticity field itself. By investigating this plot overtime, it becomes quite clear how the vorticity develops and changes over time, and how this term causes it. Essentially, in both cases, the peak in vorticity generation happens in the very early time, and as the instability is allowed to grow, less and less vorticity is generated, but it is generated over a wider field. In the case of the high stratification, the vortical field continuously decays towards zero as is expected since it quickly enters the state of the decaying mixing regime. For the low stratification case, though, the decay seems to slow and asymptote to a constant state that stretches slightly wider as time goes on. This seems to imply that this low stratification may not become fully suppressed immediately, but rather it will continue to grow at a constant, albeit slow, rate.

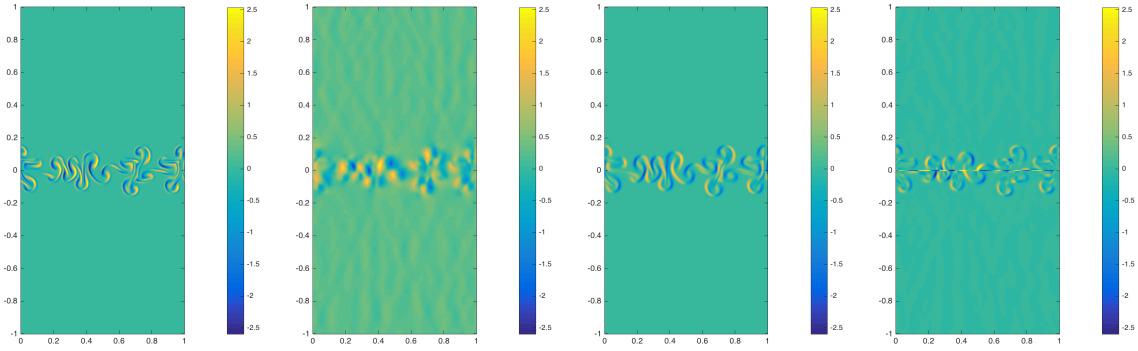

(a) Term 1 (b) Term 2 (c) Term 3 (d) Term 4

Figure 6.14: The individual terms of the vorticity equation, i.e. equation 6.18. The first term is the effects of dilatation, the second is the interaction of the hydrostatic specific volume with the fluctuating pressure, the third is the interaction of the hydrostatic pressure with the fluctuating specific volume, and the fourth term is the perturbation baroclinic term. The viscous dissipation is omitted for clarity.

To truly have a clear understanding of all the effects in play in these simulations, more run time is needed to see how the low stratification case continues to evolve and whether or not it becomes completely suppressed when given enough time.

6.6 Conclusions

A continuation of the study into the effects of compressibility on the Rayleigh-Taylor instability was presented. This study involved extending previous research on the single mode instability to the multi-mode regime. This study was done using the Parallel Adaptive Wavelet Collocation Method to perform wavelet based direct numerical simulations in order to fully resolve the entirety of the scales of the flow but to still keep the cost of the simulations at a reasonable level. These simulations were carried out with an initially isothermal background stratification with varying levels of strength based on the isothermal Mach number, i.e. $M = 0.3$ and $M = 0.9$. These simulations were performed at a moderately high Reynolds number of $Re_p = 5000$.

The resulting simulations showed surprising effects. For both stratification strengths, significant suppression was observed resulting in the mixing layer and the relevant speed at which it grew to be significantly reduced when compared to that of the single mode case. The velocity of the bubble and spike layers for the high stratification do nothing but decay from the initial conditions, while the velocity of low stratification case seems to asymptote to some constant value. This effect can partly be explained by investigating the average values in the mixing layer. For the high stratification case, the density is quickly smoothed to that of a stable stratification, and thusly the velocity fields peak and then begin to diminish. For the low stratification, though, the mixing layer is working towards a stable stratification, but because of the weakness of the background stratification, the layer must become significantly thicker before a completely stable state can be reached. This is expressed by the average velocities seemingly growing asymptoticly to a constant state in which the layer slowly continues to grow in size.

To truly fully understand these effects, an investigation into the vorticity and the terms of its relevant transport equation was done. It was found that the average vorticity in the field

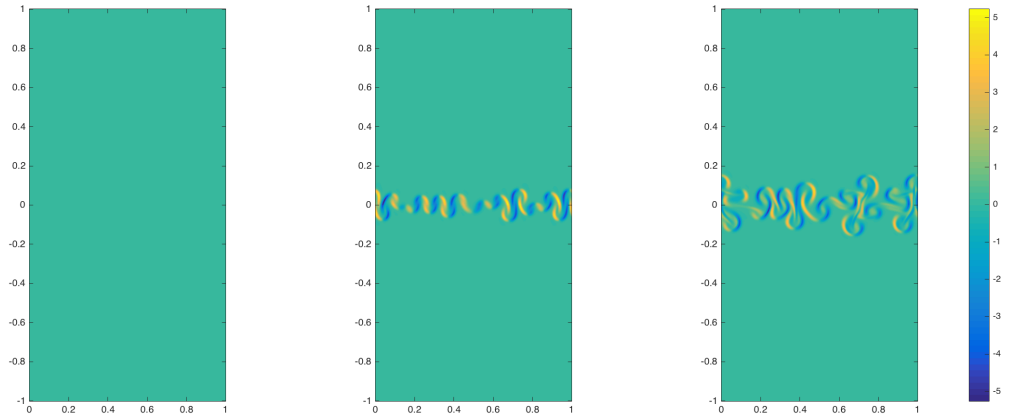

(a) t=0 (b) t=2 (c) t=4

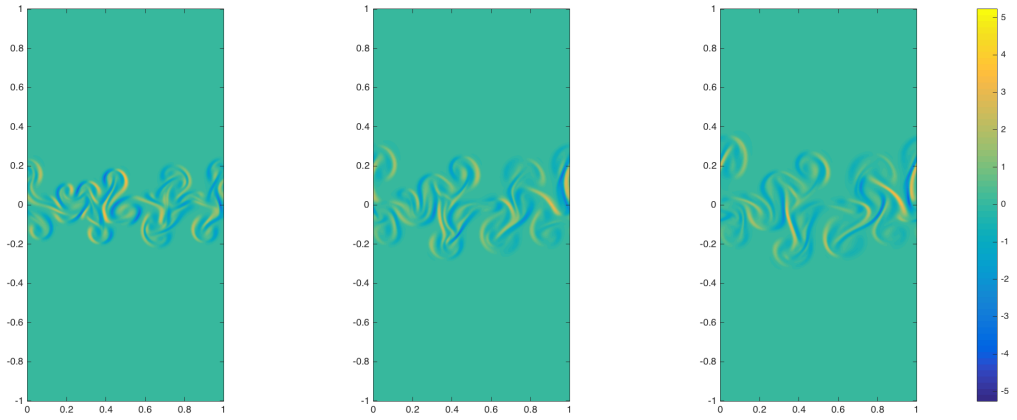

(d) t=6 (e) t=8 (f) t=10

Figure 6.15: The evolution of the third term, i.e. the effects of the fluctuating specific volume, of the presented vorticity equation for the $M = 0.3$ case.

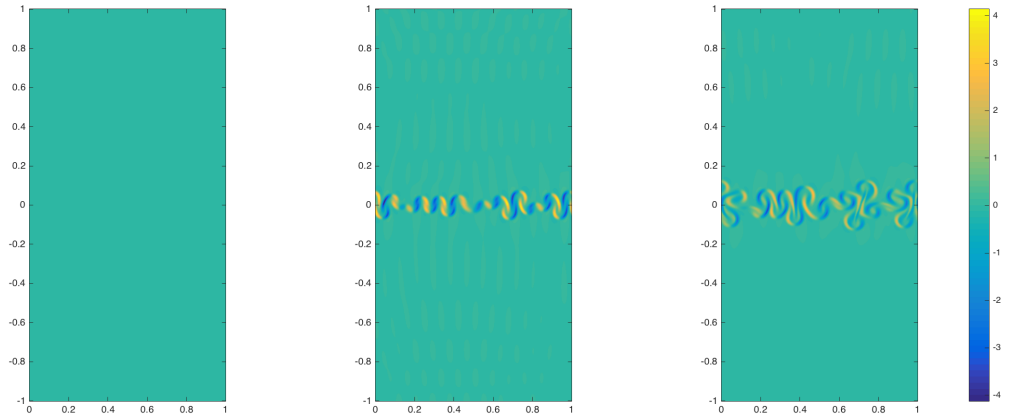

(a) t=0 (b) t=2 (c) t=4

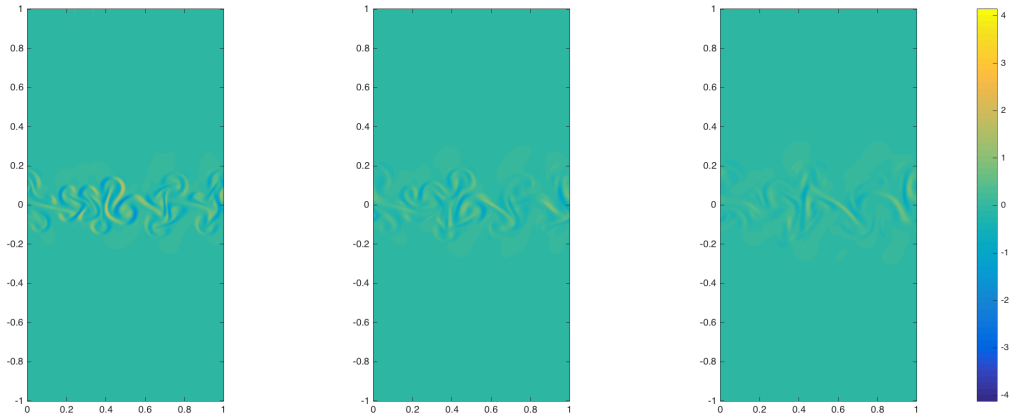

(d) t=6 (e) t=8 (f) t=10

Figure 6.16: The evolution of the third term, i.e. the effects of the fluctuating specific volume, of the presented vorticity equation for the $M = 0.3$ case.

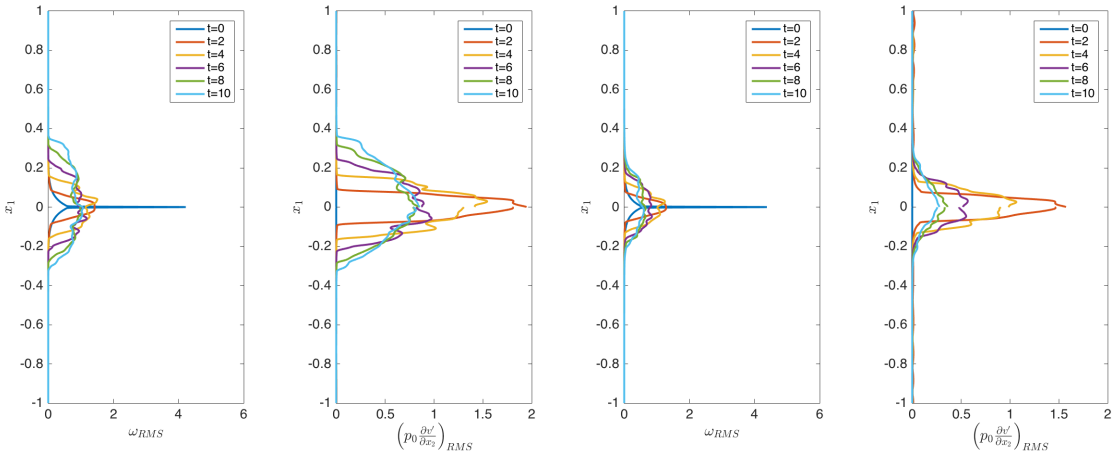

(a) M=0.3 (b) M=0.3 (c) M=0.9 (d) M=0.9

Figure 6.17: The RMS values of the vorticity in addition to the fluctuating specific volume term of the vorticity equation as a function of x_1 plotted at various times for both the M=0.3 (left) and M=0.9 (right) case.

decays over time. This decay is more intense for higher stratifications, and it can all be explained through one term in the vorticity equation. It was also found that the majority of the terms in the vorticity equation account for less than 5% of the transport. The term that accounts for the rest of the transport is derived from the interaction between the hydrostatic background pressure and the fluctuating specific volume. Essentially as the simulations are carried out, this term generates vorticity in the opposite direction as needed for growth and this causes a diminish in the magnitude of the vorticity generated. This leads the vorticity production to peak very early in the simulations, and then to quickly decay. In the case of high stratifications, this decay tends towards 0 as the instability transitions into a decaying mixing regime. For the low stratification, though, the vorticity generation appears to stall at a small but non-zero rate which accounts for the low velocity growth that the instability continues to experience. In the end, longer simulation times are needed to truly capture the full extent of the growth of the low stratification state, but the results from the high stratification state are very definitive.

Chapter 7

Conclusions and Future Work

7.1 Conclusions

Successful high-resolution wavelet-based direct numerical simulations were carried out for the compressible low Atwood Rayleigh-Taylor instability. It was found that to ensure fully resolved, physical, and symmetric simulations without the addition of unwanted modes, an investigation into the initial symmetry of the problem must be used. By exploring the symmetry in the initial conditions and minimizing the inevitable computational and numeric asymmetry that occurs, the simulations were able to be carried out until very late times while remaining highly symmetric.

The first portion of the investigation involved exploring the effects of Reynolds number and isothermal Mach number on the development of the single mode Rayleigh-Taylor instability. Through this, it was discovered that Reynolds number has a very minimal impact on the overall growth of the isothermal and compressible scenario. On the other hand, though, it was found that the isothermal Mach number, which acts as a measure of the static background stratification, has a significant impact and causes an increase in the asymmetry between the bubble and spike development in addition to causing the complete suppression of the instability growth at moderate to high Mach numbers. This effect was explored by analyzing the vorticity transport terms and also investigating the evolution of a vortex pair in the same stratification. Through this, it was shown that the fluctuating baroclinic term was responsible for the asymmetry at low Mach numbers, while the generation of vorticity in the opposing direction by the perturbation specific volume term was responsible for the suppression. The vortex pairs were able to be used to predict the height of the

final mixing region for Mach numbers of 0.6 and above, and they were also suppressed through the same mechanism.

The second full investigation was done by comparing the effects of the background stratification type on the instability growth. The isopycnic and isentropic background stratifications were thusly compared to the isothermal stratifications. Through this, it was found that in the early times, all of the stratifications caused an initial suppression to the growth in the linear and potential flow regimes, but after that, various effects dominated depending on the stratification. As stated before, it was again confirmed that moderate and high Mach number stratifications caused complete suppression in the isothermal case and this was caused by the perturbation specific volume term in the vorticity transport equation. For the isentropic case, though, increasing the Mach number of the stratification caused both an increase in the late time asymmetry between the bubble and spike by accelerating the growth of just the spike. This was due to the vorticity transport done by the interaction of the dilitation, the perturbation baroclinic term, and the fluctuating specific volume term. Finally, the isopycnic case was found to accelerate the growth of the instability with increasing Mach number. For this stratification, the flow remained highly symmetric until the fluctuating baroclinic term became significant, and then became highly asymmetric between the bubble and spike.

The third and final investigation was done on the effects of the isothermal stratification on the multi-modal RTI. To do this, the same stratifications were investigated as the first simulation with a focus on the $M = 0.3$ and $M = 0.9$ cases. It was found that for the multi-mode case, all instability growth was highly suppressed. The only significant term was the fluctuating specific volume term, and it continued to generate vorticity in the opposing direction to the growth. Essentially, this removal of vorticity leads to the instability reaching a maximum growth height and then entering into a decaying mixing regime in which the two fluids mix and the kinetic energy is slowly dissipated. This region was investigated by looking at the average values across the domain, and it was found that given enough time, the simulations worked towards a completely stable state.

When all of this is taken into consideration, the full set of simulations can be examined

through a different lens. Essentially, we must ask the question: in what scenario would each of these stratifications be useful? Well, this series of investigations showed that if the desired result is to suppress the growth of the instability, strong isothermal conditions are ideal, with multi-modal perturbations being the most suitable since they are suppressed even faster. If intense growth is wanted, especially at late times, the isopycnic stratification is the desired state, with the Mach number essentially controlling the speed at which the mixing occurs. The isentropic simulations show that if an asymmetric growth is desired, than the isentropic background stratification would be the best. Overall though, the key is more so that the understanding of the effects of these various stratifications has been greatly increased, and this knowledge can now be put to use in real world applications and further simulation efforts.

7.2 Future Work

As always, there is more work that can be accomplished on this project. The most important next step is to broaden the results of the multi-mode conditions. An exploration that will be needed by the community at large is a full sweep of the Reynolds number effects and dimensionality in addition to the exploration of all of the various background stratifications. In essence, the multi-mode investigation could potentially lead to multiple more papers in which all of the various effects found in the single mode case are explored.

Besides extending the multi-mode results, there are many other directions in which this study could go in the future. There are many effects that have yet to be studied and are not fully understood. Studying such things as random equilibrium initializations and initializations where the thermodynamics are very much out of equilibrium would yield interesting results. The inclusion of more physics, such as magnetism or reactions, into the problem would surely uncover new effects. This code base is actually already easily adapted to include reactions between two species, and some preliminary work on electromagnetic effects has been completed as well. Also, there has been some work extending and exploring RTI in the immiscible case with PAWCM by using a newly found and developed level-set method, but all three of these projects require significant more time before

they can come to fruition. At this point, the possibilities are seemingly endless, but realistically, this project has already pushed PAWCM to its limits in its current form. Any intense future work will most likely require the use of a different code base and the redevelopment of the environment for suitable use.

Bibliography

[1] 5. Newton's Method for Nonlinear Equations and Unconstrained Minimization, chapter 8, page 86110.

[2] Bhanesh Akula, Prasoon Suchandra, Mark Mikhaeil, and Devesh Ranjan. Dynamics of unstably stratified free shear flows: an experimental investigation of coupled KelvinHelmholtz and RayleighTaylor instability. Journal of Fluid Mechanics, 816:619–660, apr 2017.

[3] J.M. Alam, N. K. -R Kevlahan, and O. V. Vasilyev. Simultaneous space–time adaptive wavelet solution of nonlinear partial differential equations. J. Comp. Phys., 214(2):829–857, 2006.

[4] U Alon and D Shvarts. TwoPhase Flow Model for RayleighTaylor and RichtmyerMeshkov Mixing *. Boston. ISBN World Scientific, 9810229100, 1996.

[5] Uri Alon, Jacob Hecht, David Mukamel, and Dov Shvarts. Scale invariant mixing rates of hydrodynamically unstable interfaces. Physical Review Letters, 72(18):2867–2870, may 1994.

[6] M. J. ANDREWS and D. B. SPALDING. A simple experiment to investigate two-dimensional mixing by rayleigh-taylor instability. Physics of fluids. A, Fluid dynamics, 2(6):922–927, 1990.

[7] R. Betti, V. N. Goncharov, R. L. McCrory, and C. P. Verdon. Growth rates of the ablative RayleighTaylor instability in inertial confinement fusion. Physics of Plasmas, 5(5):1446, may 1998.

[8] William H. Cabot and Andrew W. Cook. Reynolds number effects on Rayleigh-Taylor instability with possible implications for type Ia supernovae. Nature Physics, 2(8):562–568, 2006.

[9] K. M. Case. Taylor Instability of an Inverted Atmosphere. Physics of Fluids, 3(3):366, 1960.

[10] S. (Subrahmanyan) Chandrasekhar. Hydrodynamic and hydromagnetic stability. Dover Publications, 1981.

[11] Yi-Ju Chou and Yun-Chuan Shao. Numerical study of particle-induced Rayleigh-Taylor instability: Effects of particle settling and entrainment. Physics of Fluids, 28(4):043302, apr 2016.

[12] ANDREW W. COOK and PAUL E. DIMOTAKIS. Transition stages of RayleighTaylor instability between miscible fluids. Journal of Fluid Mechanics, 443:69–99, sep 2001.

[13] Megan S Davies Wykes and Stuart B Dalziel. Efficient mixing in stratified flows: experimental study of a RayleighTaylor unstable interface within an otherwise stable stratification. J. Fluid Mech, 756:1027–1057, 2014.

[14] Giuliano De Stefano and Oleg V. Vasilyev. Wavelet-based adaptive large-eddy simulation with explicit filtering. Journal of Computational Physics, 238:240–254, apr 2013.

[15] Guy Dimonte. Spanwise homogeneous buoyancy-drag model for RayleighTaylor mixing and experimental evaluation. Physics of Plasmas, 2000.

[16] Guy Dimonte, D. L. Youngs, A. Dimits, S. Weber, M. Marinak, S. Wunsch, C. Garasi, A. Robinson, M. J. Andrews, P. Ramaprabhu, A. C. Calder, B. Fryxell, J. Biello, L. Dursi, P. MacNeice, K. Olson, P. Ricker, R. Rosner, F. Timmes, H. Tufo, Y.-N. Young, and M. Zingale. A comparative study of the turbulent RayleighTaylor instability using high-resolution three-dimensional numerical simulations: The Alpha-Group collaboration. Physics of Fluids, 16(5):1668, apr 2004.

[17] R. E. Duff, F. H. Harlow, and C. W. Hirt. Effects of Diffusion on Interface Instability between Gases. Physics of Fluids, 5(4):417, 1962.

[18] M Farge and N Kevlahan. Wavelets and turbulence. Proceedings of the ..., 1996.

[19] Markus Flaig, Tomasz Plewa, Paul A. Keiter, R. Paul Drake, Mike Grosskopf, Carolyn Kuranz, and Hye-Sook Park. Design of a supernova-relevant RayleighTaylor experiment on the National Ignition Facility. I. Planar target design and diagnostics. High Energy Density Physics, 12:35–45, sep 2014.

[20] S. Gauthier and B. Le Creurer. Compressibility effects in RayleighTaylor instability-induced flows. Philosophical Transactions of the Royal Society of London A: Mathematical, Physical and Engineering Sciences, 368(1916), 2010.

[21] Serge Gauthier. Compressible RayleighTaylor turbulent mixing layer between Newtonian miscible fluids. Journal of Fluid Mechanics, 830:211–256, nov 2017.

[22] E. Georg and J. Glimm. Self-similarity of RayleighTaylor mixing rates. Physics of Fluids, 17:054101, 2005.

[23] S. Gerashchenko and D. Livescu. Viscous effects on the Rayleigh-Taylor instability with background temperature gradient. Physics of Plasmas, 23(7):072121, jul 2016.

[24] Jean Charles Gilbert and Xavier Jonsson. LIBOPT - an environment for testing solvers on heterogeneous collections of problems - version 1.0. Technical Report RT-0331, INRIA, March 2007.

[25] V. N. Goncharov. Analytical Model of Nonlinear, Single-Mode, Classical Rayleigh-Taylor Instability at Arbitrary Atwood Numbers. Physical Review Letters, 88(13):134502, mar 2002.

[26] S. S. Gopalakrishnan, J. Carballido-Landeira, A. De Wit, and B. Knaepen. Relative role of convective and diffusive mixing in the miscible Rayleigh-Taylor instability in porous media. Physical Review Fluids, 2(1):012501, jan 2017.

[27] Andreas Griewank. Achieving Logarithmic Growth Of Temporal And Spatial Complexity In Reverse Automatic Differentiation. Optimization Methods and software, 1:3554, 1992.

[28] I. Hachisu, T. Matsuda, K. Nomoto, and T. Shigeyama. Rayleigh-Taylor instabilities and mixing in the helium star models for Type Ib/Ic supernovae. Astrophysical Journal, Part 2 - Letters, 368:L27–L30, 1991.

[29] Magnus Rudolph Hestenes. Conjugate direction methods in optimization. Applications of mathematics. Springer-Verlag, 1980.

[30] H. Jin, X. F. Liu, T. Lu, B. Cheng, J. Glimm, and D. H. Sharp. RayleighTaylor mixing rates for compressible flows. Journal of Fluid Mechanics, 17:024104, 2005.

[31] G. C. Jordan IV, R. T. Fisher, D. M. Townsley, A. C. Calder, C. Graziani, S. Asida, D. Q. Lamb, and J. W. Truran. ThreeDimensional Simulations of the Deflagration Phase of the Gravitationally Confined Detonation Model of Type Ia Supernovae. The Astrophysical Journal, 681(2):1448–1457, jul 2008.

[32] Nicholas K. R. Kevlahan and Oleg V. Vasilyev. An Adaptive Wavelet Collocation Method for Fluid-Structure Interaction at High Reynolds Numbers. SIAM Journal on Scientific Computing, 26(6):1894–1915, jan 2005.

[33] K. Kifonidis, T. Plewa, H. Th. Janka, and E. Mueller. Non-spherical Core Collapse Supernovae I. Neutrino-Driven Convection, Rayleigh-Taylor Instabilities, and the Formation and Propagation of Metal Clumps. feb 2003.

[34] J. D. Kilkenny, S. G. Glendinning, S. W. Haan, B. A. Hammel, J. D. Lindl, D. Munro, B. A. Remington, S. V. Weber, J. P. Knauer, and C. P. Verdon. A review of the ablative stabilization of the RayleighTaylor instability in regimes relevant to inertial confinement fusion. Physics of Plasmas, 1(5):1379, may 1994.

[35] P P Kronberg. Extragalactic magnetic fields. Reports on Progress in Physics, 57(4):325–382, apr 1994.

[36] M.-A. Lafay, B. Le Creurer, and S. Gauthier. Compressibility effects on the Rayleigh-Taylor instability between miscible fluids. Europhysics Letters (EPL), 79(6):64002, sep 2007.

[37] David Layzer and David. On the Instability of Superposed Fluids in a Gravitational Field. The Astrophysical Journal, 122:1, jul 1955.

[38] Hyun Geun Lee and Junseok Kim. A comparison study of the Boussinesq and the variable density models on buoyancy-driven flows. Journal of Engineering Mathematics, 75(1):15–27, oct 2011.

[39] Walter H. G. Lewin, J. van. Paradijs, and Edward Peter Jacobus van den Heuvel. X-ray binaries. Cambridge University Press, 1997.

[40] John. M. Lewis, S. Lakshmivarahan, and Sudarshan Kumar Dhall. Dynamic data assimilation: a least squares approach. Cambridge University Press, 2006.

[41] John Lindl. Development of the indirect-drive approach to inertial confinement fusion and the target physics basis for ignition and gain. Physics of Plasmas, 2(11):3933, nov 1995.

[42] D. Livescu. Compressibility effects on the RayleighTaylor instability growth between immiscible fluids. Physics of Fluids, 16(1):118, 2004.

[43] D Livescu. Numerical simulations of two-fluid turbulent mixing at large density ratios and applications to the Rayleigh-Taylor instability. Philosophical transactions. Series A, Mathematical, physical, and engineering sciences, 371(2003):20120185, nov 2013.

[44] X. Ma, P. A. Delamere, and A. Otto. Plasma transport driven by the Rayleigh-Taylor instability. Journal of Geophysical Research: Space Physics, 121(6):5260–5271, jun 2016.

[45] Eduard Stiefel Magnus Rudolph Hestenes. Methods of conjugate gradients for solving linear systems. Journal of Research of the National Bureau of Standards, 49(6), 1952.

[46] J.P. Mellado, S. Sarkar, and Y. Zhou. Large-eddy simulation of RayleighTaylor with compressible miscible fluids. Physics of Fluids, 17:076101, 2005.

[47] Alireza Nejadmalayeri, Alexei Vezolainen, Eric Brown-Dymkoski, and Oleg V. Vasilyev. Parallel adaptive wavelet collocation method for PDEs. Journal of Computational Physics, 298:237–253, 2015.

[48] D. Oron, L. Arazi, D. Kartoon, A. Rikanati, U. Alon, and D. Shvarts. Dimensionality dependence of the RayleighTaylor and RichtmyerMeshkov instability late-time scaling laws. Physics of Plasmas, 8(6):2883–2889, jun 2001.

[49] J.M. Ortega and W.C. Rheinboldt. Iterative Solution of Nonlinear Equations in Several Variables. Classics in Applied Mathematics. Society for Industrial and Applied Mathematics, 1987.

[50] L. Rayleigh. Investigation of the character of the equilibrium of an incompressible heavy fluid of variable density. Proceedings of the London mathematical society, 14:170–177, 1884.

[51] S J Reckinger, D Livescu, and O V Vasilyev. Adaptive wavelet collocation method simulations of RayleighTaylor instability. Physica Scripta, T142(T142):014064, dec 2010.

[52] Scott J. Reckinger, Daniel Livescu, and Oleg V. Vasilyev. Comprehensive numerical methodology for direct numerical simulations of compressible RayleighTaylor instability. Journal of Computational Physics, 313:181–208, 2016.

[53] M. S. Roberts and J. W. Jacobs. The effects of forced small-wavelength, finite-bandwidth initial perturbations and miscibility on the turbulent RayleighTaylor instability. Journal of Fluid Mechanics, 787:50–83, jan 2016.

[54] Wolfram Schmidt. Turbulence: From tea kettles to exploding stars. Nature Physics, 2(8):505–506, aug 2006.

[55] Kai Schneider and Oleg V. Vasilyev. Wavelet Methods in Computational Fluid Dynamics*. Annual Review of Fluid Mechanics, 42(1):473–503, jan 2010.

[56] David M. Schultz, Katharine M. Kanak, Jerry M. Straka, Robert J. Trapp, Brent A. Gordon, Dusan S. Zrnić, George H. Bryan, Adam J. Durant, Timothy J. Garrett, Petra M. Klein, Douglas K. Lilly, David M. Schultz, Katharine M. Kanak, Jerry M. Straka, Robert J. Trapp, Brent A. Gordon, Dusan S. Zrnić, George H. Bryan, Adam J. Durant, Timothy J. Garrett, Petra M. Klein, and Douglas K. Lilly. The Mysteries of Mammatus Clouds: Observations and Formation Mechanisms. Journal of the Atmospheric Sciences, 63(10):2409–2435, oct 2006.

[57] D.H. Sharp. An overview of Rayleigh-Taylor instability. Physica D: Nonlinear Phenomena, 12(1):3–18, 1984.

[58] Innocent Souopgui, Scott A. Wieland, M. Yousuff Hussaini, and Oleg V. Vasilyev. Spacetime adaptive approach to variational data assimilation using wavelets. Journal of Computational Physics, 306:253–268, 2016.

[59] G. Taylor. The Instability of Liquid Surfaces when Accelerated in a Direction Perpendicular to their Planes. I. Proceedings of the Royal Society A: Mathematical, Physical and Engineering Sciences, 201(1065):192–196, mar 1950.

[60] Oleg V. Vasilyev. Solving Multi-dimensional Evolution Problems with Localized Structures using Second Generation Wavelets. International Journal of Computational Fluid Dynamics, 17(2):151–168, mar 2003.

[61] Oleg V Vasilyev and Christopher Bowman. Second-Generation Wavelet Collocation Method for the Solution of Partial Differential Equations. Journal of Computational Physics, 165(2):660–693, 2000.

[62] Oleg V Vasilyev, Bushe, W Kendal, and W K Bushe. On the Use of a Dynamically Adaptive Wavelet Collocation Algorithm in Direct Numerical Simulations of Non-Premixed Turbulent Combustion. Center for Turbulence Research Annual Research Briefs, 1998.

[63] Y.M. Wang and J. Robertson. Late stages of the RayleighTaylor instability: a numerical study in the context of accreting neutron stars. Astrophysical Journal, 299:85–108, 1985.

[64] Tie Wei and Daniel Livescu. Late-time quadratic growth in single-mode Rayleigh-Taylor instability. Physical Review E, 86(4):046405, oct 2012.

[65] Scott A. Wieland, Scott J. Reckinger, Peter H. Hamlington, and Daniel Livescu. Effects of Isothermal Stratification Strength on the Single Mode Compressible Rayleigh-Taylor Instability. Manuscript in Preperation, 2017.

[66] Scott A. Wieland, Scott J. Reckinger, Peter H. Hamlington, and Daniel Livescu. Effects of Stratification Type on the Compessible Single Mode Rayleigh-Taylor Instability. Manuscript in Preperation, 2017.

[67] Scott A. Wieland, Scott J. Reckinger, Peter H. Hamlington, and Daniel Livescu. Multimodal Perturbation Evolution in the Compressible Rayleigh-Taylor Instability. In 70th Annual Meeting of The APS Division of Fluid Dynamics, 2017.

[68] F. A. (Forman Arthur) Williams. Combustion Theory. Addison/Wesley Pub. Co.

[69] Qingzhen Yang, Ben Q. Li, and Feng Xu. Electrohydrodynamic Rayleigh-Taylor instability in leaky dielectric fluids. International Journal of Heat and Mass Transfer, 109:690–704, jun 2017.

[70] David L. Youngs. Modelling turbulent mixing by Rayleigh-Taylor instability. Physica D: Nonlinear Phenomena, 37(1):270–287, 1989.

[71] M. Zingale, S. E. Woosley, C. A. Rendleman, M. S. Day, and J. B. Bell. Three- dimensional numerical simulations of RayleighTaylor unstable flames in Type Ia supernovae. Astrophysical Journal, 632:1021–1034, 2005.

[72] Ellen G. Zweibel and Carl Heiles. Magnetic fields in galaxies and beyond. Nature, 385:131–136, 1997.